Distance Measurement Error Modeling for Time-of-Arrival Based Indoor Geolocation

A Dissertation Submitted to the Faculty

of

WORCESTER POLYTECHNIC INSTITUTE

in partial fulfillment of the requirements for the

Degree of Doctor of Philosophy

in

Electrical and Computer Engineering

by

_____

Bardia Alavi

April 2006

APPROVED

_____

Prof. Kaveh Pahlavan, Advisor

_____

Prof. Fred J. Looft, Head, ECE Department

to

My Parents

Abstract

In spite of major research initiatives by DARPA and other research organizations, precise indoor geolocation still remains as a challenge facing the research community. The core of this challenge is to understand the cause of large ranging errors in estimating the time of arrival (TOA) of the direct path between the transmitter and the receiver. Results of wideband measurement in variety of indoor areas reveal that large ranging errors are caused by severe multipath conditions and frequent occurrence of undetected direct path (UDP) situations. Empirical models for the behavior of the ranging error, which we refer to as the distance measurement error (DME), its relation to the distance between the transmitter and the receiver and the bandwidth of the system is needed for development of localization algorithms for precise indoor geolocation.

The main objective of this dissertation is to design a direct empirical model for the behavior of the DME. In order to achieve this objective we provide a framework for modeling of DME, which relates the error to the distance between the transmitter and the receiver and bandwidth of the system. Using this framework we first designed a set of preliminary models for the behavior of the DME based on the CWINS proprietary measurement calibrated ray-tracing simulation tool. Then, we collected a database of 2934 UWB channel impulse response measurements at 3-8GHz in four different buildings to incorporate a variety of building materials and architectures. This database

was used for the design of more in depth and realistic models for the behavior of the DME. The DME is divided into two components, Multipath-DME (MDME) and UDP-DME (UDME). Based on the empirical data, models for the behavior of each of these components are developed. These models reflect the sensitivity to bandwidth and show that by increasing the bandwidth MDME decreases. However in UDME the behavior is complicated. At first it reduces as we increase the bandwidth but after a certain bandwidth it starts to increase. In addition to these models through an analysis on direct path power versus the total power the average probability of having a UDP was calculated.

Acknowlegment

First of all I want to thank my advisor, Professor Kaveh Pahlavan for all his guidance and helps through all the years of my PhD. I want to express my gratitude and at the same time what I think about him. What I have learnt from him is beyond the technical knowledge. He is one of the most responsible and caring persons that I have seen in my life, as if it was not his responsible sense I don't know how my PhD would turn.

I would like to thank National Science Foundation, Innovative Wireless Technologies, and Army Research Lab for their quality funding that helped to my research work and improvement of this project.

I am deeply thankful to my close friends in CWINS lab, Nayef Alsindi and Mohammad Heidari for all their helps and more importantly the valuable and memorable times that we spent with each other. There have been numerous associates who have helped me over the last few years, especially, Emad Zand, Dr. Jacques Beneat, Hamid Hatami, Muzaffer Kanaan, Ferit Ozan Akgul, and Leon T. Metreaud.

I want to thank all of my friends in Worcester and their indirect affect on quality of my work.

Thanks are due to Professor Allen H. Levesque for his kind help over the last few years and also his valuable comments on my thesis, to Professor Fred J. Looft and

Professor Xinrong Li for their valuable comments as my thesis committee members, and to many professors at WPI from whom I have learned greatly.

Words can not express my gratefulness to my dear parents and my brother for their care and support and their important responsibility for enabling me in reaching this point of my life. Finally my gratefulness to God, for giving me the strength of mind and perseverance for facing challenges and overcoming obstacles.

Table of Content

List of Figures

List of Tables

Table of Acronyms

AK	Atwater Kent
BER	Bit Error Rate
CCDF	Complementary Cumulative Distribution Function
CDF	Cumulative Distribution Function
CWINS	Center for Wireless Information Network Studies
DDP	Detected Direct Path
DME	Distance Measurement Error
DP	Direct Path
FDP	First Detected Peak
GPS	Global Positioning System
ITI	Indoor to Indoor
LNA	Low Noise Amplifier
LOS	Line of Sight
MDME	Multipath Distance Measurement Error
NC	No Coverage
OLOS	Obstructed Line of Sight
OTI	Outdoor to Indoor
PDF	Probability Density Function
PLM	Path-Loss Model
RMSE	Root Mean Square Error
RT	Ray Tracing
RTI	Roof to Indoor
Rx	Receiver
S-V	Saleh-Valenzuela
STD	Standard Deviation
TOA	Time of Arrival
Tx	Transmitter
UDME	UDP Distance Measurement Error
UDP	Undetected Direct Path
UWB	Ultra-Wideband
WPI	Worcester Polytechnic Institute

Chapter 1

Introduction

1.1 Evolution of Indoor Geolocation Technology
1.2 Distance Measurement Error
1.3 Objective of the Thesis
1.4 Contributions of the Thesis
1.5 Outline of the Thesis

1.1 Evolution of Indoor Geolocation Technology

Localization using radio signals has been considered as an application of wireless communications since World War II, where locating soldiers in emergency situation was critical. This problem was addressed by the US Department of Defense many years after, during the war in Vietnam, when they launched a series of satellites under a project called Global Positioning System (GPS) [Kap96]. In the early times of GPS, these satellites were designated for military applications only. However, around 1990 they became partially available for commercial use. Today, GPS is widely used in commercial and personal applications. Although GPS has attracted numerous popular outdoor applications in open areas it does not perform properly in highly dense urban and indoor areas [Pah98].

In late 1990s, at about the same time that E-911 technologies were introduced [Mey96], another initiative for accurate indoor geolocation began independently, motivated by a variety of applications envisioned for indoor location-sensing in

commercial, public safety, and military settings [Pah02a] [Kos00] [Pot00]. In commercial applications there is an increasing need for indoor location-sensing systems to track people with special needs, the elderly, and children who are away from visual supervision. Other applications include systems to assist the sight-impaired, to locate instrumentation and other equipment in hospitals, to locate surgical equipment in an operating room, and to locate specific items in warehouses. In public safety and military applications, indoor location sensing systems are needed to track inmates in prisons and to guide policemen, fire-fighters, and soldiers in accomplishing their missions inside buildings [Pah98].

Accurate indoor localization is also an important part of various personal robotics applications [Jen01] as well as in the more general context of context-aware computing [War97]. More recently, location sensing has found applications in location-based handoffs in wireless networks [Pah00], location-based *ad-hoc* network routing [Ko98] [Jai01] and location-based authentication, security, privacy [Sma02], and RFID assisted localization [Hah04]. These and other applications have stimulated interest in modeling the propagation environment to assess the accuracy of different sensing techniques [Pah98] [Kri99a], as well as in developing novel technologies to implement the systems [Fon01] [Bah00a] [Bah00b]. We have already seen implementation of the first generation of indoor positioning products using a variety of technologies [Wer98] [Roo02a] [Roo02b], the more accurate second generation of products demands extensive research in understanding and modeling of the channel behavior caused by intensive multipath in the indoor areas. These models are necessary for the design of

meaningful algorithms to remedy the effects of extensive multipath [Che99], [Kan04a, b], which causes large ranging error that we refer to as the distance measurement error (DME).

1.2 Distance Measurement Error

Multipath channel impulse response is modeled as [Sal87], [Rap02], [Pah05],

$$h(\tau) = \sum_{k=1}^{L_p} \alpha_k \delta(\tau - \tau_k), \tag{1-1}$$

where L_p is the number of multipath components, and $\alpha_k = |\alpha_k| e^{j\phi_k}$ and τ_k are amplitude and propagation delay of the kth path, respectively. To make discussions simpler, we define the direct line-of-sight (LOS) path between transmitter and receiver antennas as the direct-path (DP) and the detected first arrival path in the measured channel impulse response as the first-detected-peak (FDP). In time-of-arrival (TOA) based positioning systems, the TOA of the FDP, $\hat{\tau}_W$ is detected as an estimate of the TOA of the DP, τ_{DP}, The estimated distance between the transmitter and the receiver antennas are obtained from,

$$\hat{d}_W = c \times \hat{\tau}_W \tag{1-2}$$

where subscript W indicates the system bandwidth and c is the speed of light. The DME is then defined as

$$DME_W = \hat{d}_W - d\ , \tag{1-3}$$

where d is the spatial distance between transmitter and receiver antennas. In practice, the empirical analysis of the DME is a function of the accuracy of measurement of the DP which is a function of the bandwidth of the measurement system. Ultra-wideband (UWB) measurements provide the widest bandwidth and consequently the most accurate measurements of the behavior of the DP [Gha04] [Opp04] [Por03].

Figure 1.1 shows the basic concepts involved in the wideband TOA measurement using arrival time of the DP in a typical indoor multipath environment [Ala03a]. In this figure the solid vertical lines represent the ideal channel impulse response generated by a ray-tracing algorithm for two arbitrary locations in an office area. The DP is also the strongest path and location of this path is the expected value of the TOA. Other paths arriving after a number of reflections and transmissions occur after the DP with lower amplitudes. These paths generated by ray tracing algorithms would have been observed at the receiver if the bandwidth of the system was infinite. In practice bandwidth is limited and the received signal will be a number of pulses whose amplitude and arrival time are the same as impulses but they have a pulse shape and addition of all these pulse shapes forms the received signal, which in Fig. 1.1 we refer to as the channel profile [Pah05]. In indoor geolocation systems we use the first detected peak of the channel profile above the detection threshold as the estimated TOA of the DP. In a single path environment the actual expected and the estimated DP are the same. In multipath conditions, however, as shown in Fig. 1.1, the peak of the channel profile gets shifted from the expected TOA resulting in a TOA estimation error caused by the multipath condition. We refer to the ranging error caused by erroneous

estimate of the TOA as DME. For a given multipath condition we expect that as we increase the bandwidth DME reduces.

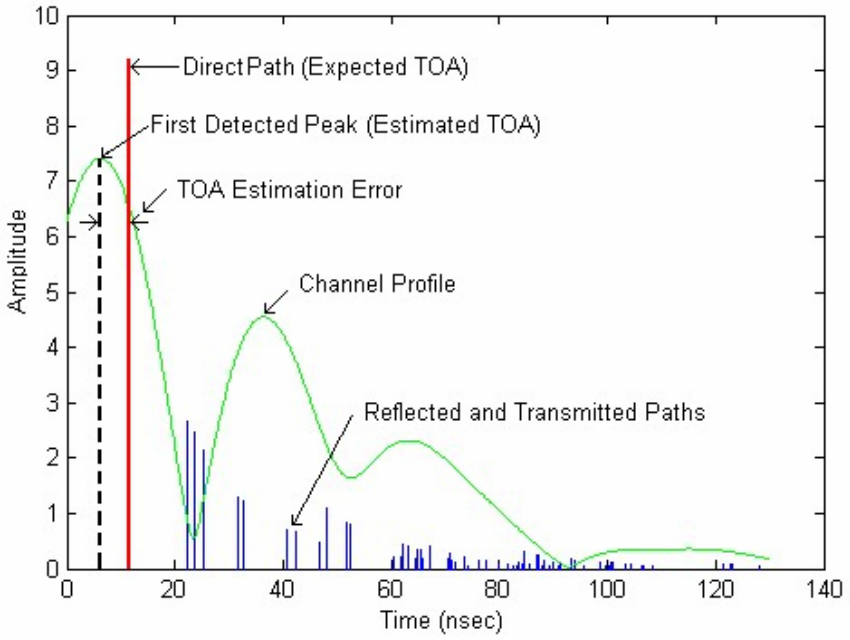

Figure 1.1: Channel profile and Channel Impulse Response

1.3 Objectives of the Research

In spite of major research initiatives by DARPA and other organizations [Fon01], [Gez05], and research and developments in a number of companies, precise indoor geolocation still remains as a challenge facing the research community. The major challenge is not the design of hardware or implementation of existing complex GPS algorithms for indoor application. The challenge is to understand the cause of large DMEs observed in severe multipath conditions and frequent occurrence of undetected direct path conditions in indoor areas [Pah98]. For development of such precise indoor geolocation systems, empirical models for the behavior of the DME and its relation to the bandwidth of the system are needed. However, the literature provides

no direct model for the DME and its relation to the bandwidth, and thus providing such a model is the central objective of this research.

The existing indoor propagation models were developed with emphasis on telecommunication applications [Has93], [And94], [Gre97], [Gha03a, b]. When we use these models for indoor geolocation the DME obtained from these models does not fit the empirical measurements and the models do not reflect thoroughly the effects of bandwidth. For example, the popular Saleh-Valenzuela (S-V) model developed at the Bell Laboratories in late 1980's, as the first comprehensive model for indoor radio propagation, does not provide a satisfactory close approximation for the error produced in geolocation measurements [Pah05]. Figure 1.2 shows complementary cumulative distribution function (CCDF) for the DME generated by S-V model and empirical data results for 500 MHz system bandwidth.

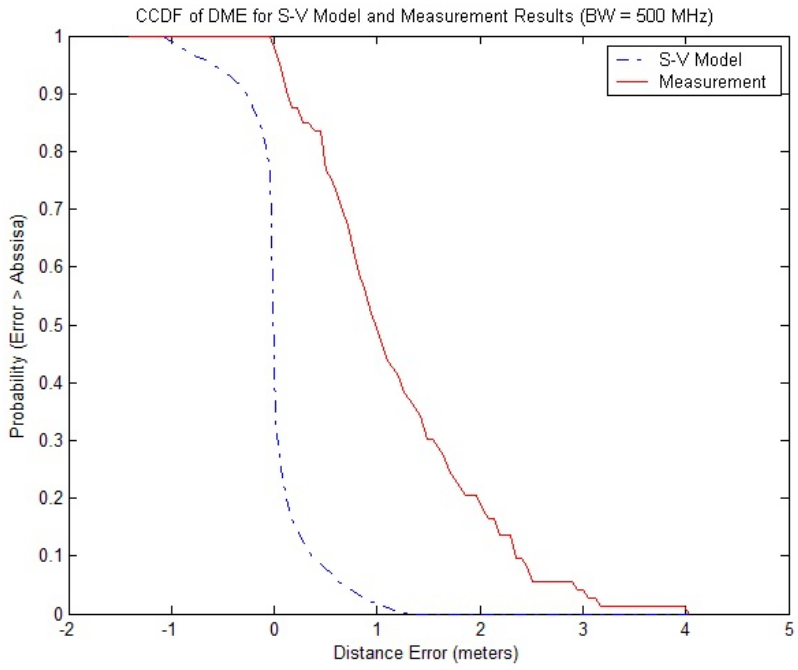

Figure 1.2: CCDF of DME for Saleh-Valenzuela Model vs. Measurement Results

Recently, it is claimed that the UWB indoor radio propagation channel model introduced by the IEEE 802.15.3a standard has paid indirect attention to the indoor geolocation problem [Foe02] [IEE03] [Mol03]. This attention is rather limited because this model is basically optimized to reflect the clusters of multipath arrivals and their impact on performance in telecommunication applications, the parameters of the model is adjusted by empirical data from measurements with a fixed bandwidth without considering the effects of distance, and it has neglected the impacts of undetected direct path conditions which is the major cause of large errors in ranging estimates.

Another model of this type that is intended to fit both telecommunication and geolocation applications is a two path model with variable delay between the two paths, which was introduced in [Kri99a, b]. This model reflects the occurrence of the UDP conditions caused by the limitation of the range of the receiver for geolocation applications and it represents the statistical behavior of the rms delay spread of the channel for telecommunication applications. The problem with this model is that the effects of all paths are represented by only two paths, making the model useless for certain telecommunications applications such as performance evaluation of RAKE receivers. Furthermore, the model is based on results of ray-tracing rather than empirical measurements. In addition, this model is developed for infinite bandwidth and neglects the effect of bandwidth and distance which are of vital practical importance for design of indoor geolocation systems.

These experiments have shown that design of a model to address both telecommunication and geolocation application becomes very complex and extremely

challenging, in particular when we want to pay attention to the behavior of the DME and its relation to distance and bandwidth. Therefore, there is a need for developing empirical models specifically for geolocation applications. The main objective of this research is to design a direct empirical model for the behavior of the DME and relate that to the system bandwidth and to the distance between the transmitter and the receiver.

1.4 Contributions of the Research

In order to achieve the main objective of the research we need to provide a framework for modeling of DME and relating that to distance and the system bandwidth. This framework and modeling were first created by using ray-tracing as a simulation tool. But a simulation based model always suffers from the disadvantage of not being based on real data. Therefore, in an extensive measurement campaign a database was collected in four different buildings to incorporate most varieties of building materials and architectures. This measurement database was used to provide different models for both path-loss and DME. The innovative path-loss models are created for geolocation applications, which consider both the power of the first path and total power. The power of the first path is essential for geolocation applications and the total power is essential for communication coverage.

The main contribution of this research is to provide a framework for direct modeling of the distance measurement error for TOA based indoor geolocation systems based on empirical measurements and to relate these errors to the bandwidth of the system. As such, the specific contributions of the research are:

a) Introducing a framework for direct modeling of the DME

b) Design of a preliminary model relating the DME to the distance and bandwidth by using results of measurement calibrated ray-tracing algorithms

c) Compiling a large database of UWB measurements in a residential house, two office buildings and a manufacturing floor with a bandwidth of up to 5GHz to enhance the preliminary models

d) Providing an analytical method to calculate average probability of having an undetected direct path condition with information about building size and materials or path-loss models of first path and total power

1.5 Outline of the Thesis

The remainder of the thesis is organized as follows. Chapters 2 and 3 complete part I of the thesis, which introduces a model for distance measurement error using a simulation tool called ray-tracing. In chapter 2 a model for a fixed bandwidth of 200 MHz is introduced and in chapter 3 the same model is studied when the bandwidth changes from 30 MHz to 3 GHz. The model consists of a zero mean Gaussian random number and an exponential part. Each of these two distributions has different weights representing the condition of the environment.

Part II of the thesis, chapters 4, 5, and 6, deals with the same problem: modeling of the distance measurement error, but in part II we use the results of the UWB measurements. Therefore in chapter 4 we describe the measurement campaign targeted for indoor geolocation channel characterization and modeling. In chapter 5 we develop

innovative path-loss models for first path, which is essential for geolocation and total power, which is essential for communication coverage. We also provide DME models based on power of the first path, these models have application in algorithm development for geolocation [Kan04a, b]. The detailed data of the path-loss models and DME models are provided in Appendices A and B. Finally in chapter 6 we introduce a complete model for distance measurement error addressing all the problems of the part I model, followed by a section for studying the effect of bandwidth on distance measurement errors.

Part III includes chapters 7 and 8 of the dissertation. Chapter 7 provides an analysis for calculating the probability of undetected direct path in indoor environment. This analysis uses the information regarding the site to calculate received power of the direct path and total power, and then uses them to calculate probability of undetected direct path. Finally chapter 8 provides a summary of the research, and proposes future researches on this topic.

Part I

Distance Measurement Error Modeling Using Ray-Tracing

In chapter 1 it is shown that telecommunication models are not a good candidate for positioning applications. Therefore there is a need for new models for geolocation in severe multipath conditions in indoor and urban areas. One approach is to design a multipath arrival model that fits both communication and positioning applications. A model of this type has been introduced in [Kri99a, b]. The problem with this model is that it is complex and not up to the point to be used in telecommunication applications. In addition this model does not include the effect of bandwidth, which is a very important factor for geolocation applications. Another approach is to model distance measurement error directly, as in chapter 2.

Chapter 2: Preliminary modeling using RT with fixed bandwidth

In this chapter we introduce a model for distance measurement error using the results of Ray-Tracing tool as a simulation tool with a fixed bandwidth.

Chapter 3: Modeling the Effect of Bandwidth

In this chapter we use the results of modeling in chapter 2 and study the effect of bandwidth on the distance measurement error.

Chapter 2

Preliminary Modeling Using RT with Fixed Bandwidth

2.1 Introduction to Ray-Tracing

Ray-Tracing (RT) software is basically a simulation environment to simulate the channel behavior in different areas [And93]. The predictions from ray tracing software are particularly accurate for propagation of radio signals at frequencies higher than 900 MHz where electromagnetic waves can be described as traveling along localized ray paths. Three basic mechanisms considered in ray tracing are: (a) transmission and reflection (b) diffraction and (c) scattering. In indoor areas, reflection and transmission usually dominate diffraction or scattering. We used RT specifically for indoor areas. Using the RT software it is possible to simulate the behavior of the signal, traveling

from the transmitter (Tx) to receiver (Rx) based on optical rules. By locating a Tx and the Rx pair, RT simulates all the paths reaching to Rx, including necessary information such as received path amplitude, time delay, arrival angle, departure angle, phase, number of reflections, and number of transmissions. RT can be used to produce large databases of channel impulse responses for statistical analysis of the channel. Therefore it saves a lot of time and energy compared to physical measurement.

These are some advantages of using RT rather than making channel measurements:

- RT tools are less costly than measurement equipments
- Ease of performing simulations
- Feasibility of measuring the channels in some hard to access places, such as factories and etc.
- Having infinite bandwidth

Although in general measurement results are more reliable than RT simulations, but for early stages of modeling using RT is highly recommended.

Figure 2.1 shows a snapshot of our RT software that was developed in our lab, CWINS.

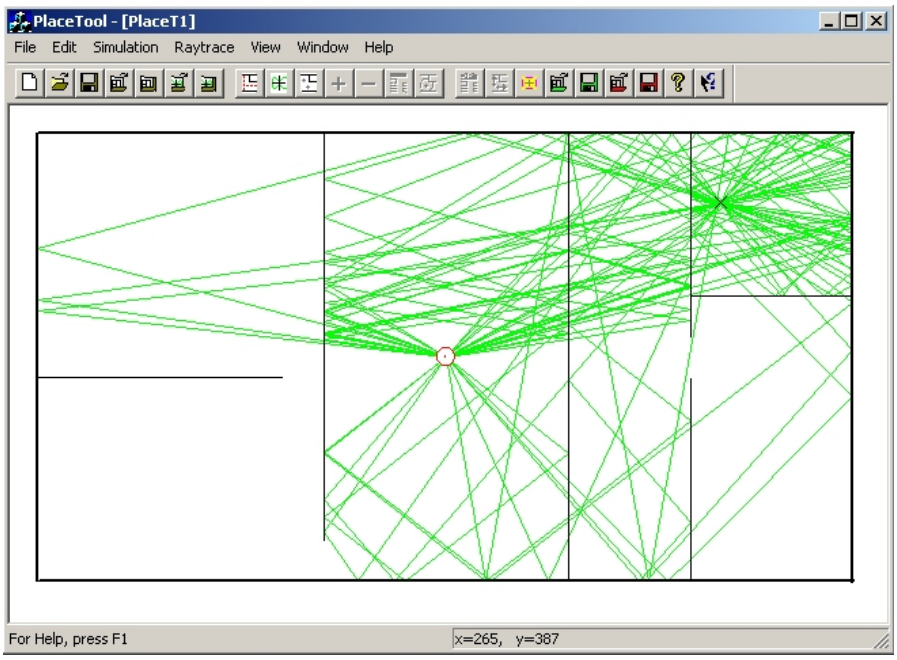

Figure 2.1: A sample snapshot of Ray-Tracing software

The rays are different paths traveling from the Tx toward the Rx. We used ray-shooting technique for out RT tool. A pincushion of rays is sent out from the transmitter, and the progress of each ray is traced through the environment until the ray has either intersected the receiver or has lost enough power that its contribution to the received signal is negligible. The time of arrival, intensity, phase, and direction of arrival are recorded for each ray that intersects the receiver. Once every ray has been traced to completion, the channel impulse response is formed. Figure 2.2 shows a sample of a channel impulse response taken from the same pair of Tx-RX shown above. Detailed explanation about RT can be found in [Pah05].

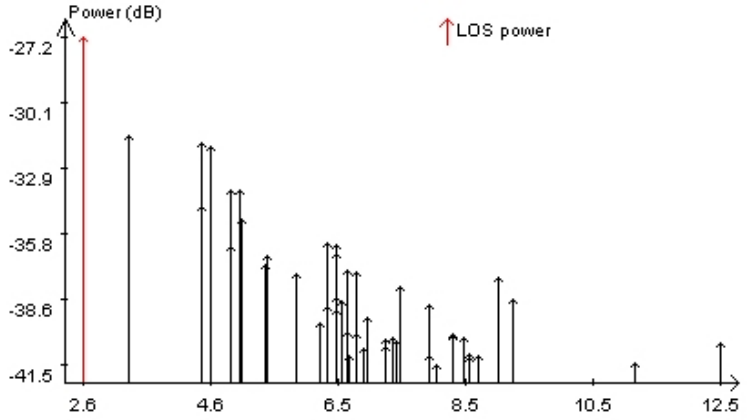

Figure 2.2: Ray-Tracing sample channel impulse response

2.2 RT Simulation

In this section we explain our scenario performed for generating the database, and then we describe the simulation procedure and the results.

2.2.1 Simulation Scenario

To generate a large database of the channel impulse responses of a typical indoor area we used a calibrated floor plan [Fal96] for RT. The floor plan is taken from the inner rooms of the second floor of Atwater Kent Laboratory, Worcester Polytechnic Institute (WPI). The calibration process aimed to fit the results of measurements with the results of RT simulation by adjusting the reflection and transmission coefficients of the walls in the floor plan. Figure 2.3 shows this floor plan.

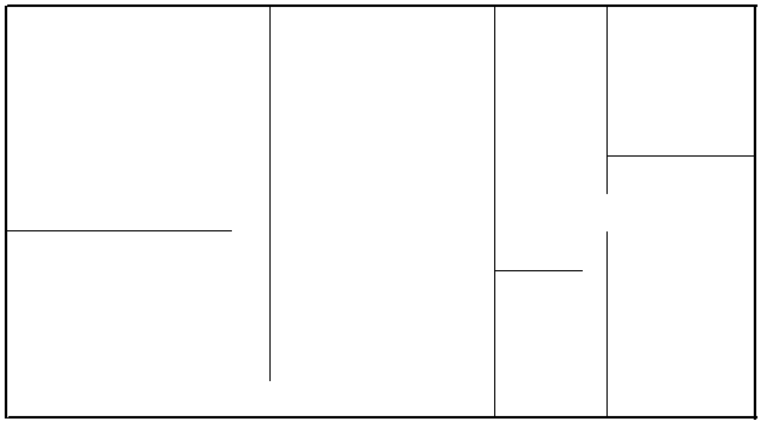

Figure 2.3: Floor plan used for RT simulation (Inner rooms of Atwater Kent building)

An adequate number of receiver locations, totally 946 points, with uniform distribution over the whole floor plan were considered for making the database of channel impulse responses. These 946 points were arranged in 22 rows and 43 columns as shown in Fig. 2.4. The minimum distance between receivers and outer walls is 67 cm, and distance between each two consecutive receivers of the same row or column is 43 cm and size of the whole floor plan is 20×11 m^2. The location of the transmitter, which is in the middle of the floor plan, does not change during the whole simulation procedure. This location is shown with a circled "X" in the figure.

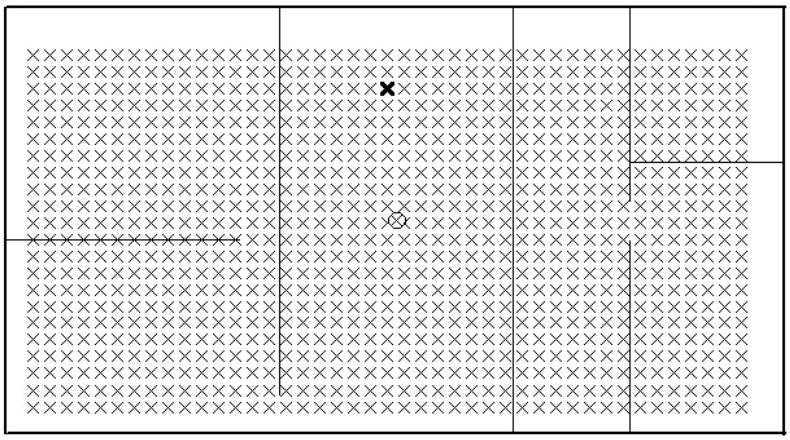

Figure 2.4: RT floor plan including all the points for simulation

2.2.2 Simulation Procedure for Calculating DME

As mentioned above, RT produces channel impulse responses which can be interpreted as channel profiles with infinite bandwidth. In order to have a realistic channel profile we need to reduce the bandwidth, and therefore we filter the ideal channel profile, which is the outcome of the RT using a low-pass filter with a given bandwidth. Then the estimated distance between the transmitter and the specified receiver is obtained from filtered channel profile, which is estimation of TOA of the FDP.

To filter the ideal channel profile we used a raised-cosine filter. Also, bandwidth of the filter used for the simulation, is a very important factor in changing the DME. The system bandwidth, which is one of the measurement equipment parameters, is related to the raised cosine pulse width, as shown in Fig. 2.5. Channel profile shown in figure 1.1 is created by convolving the raised cosine filter with channel impulse response generated from RT.

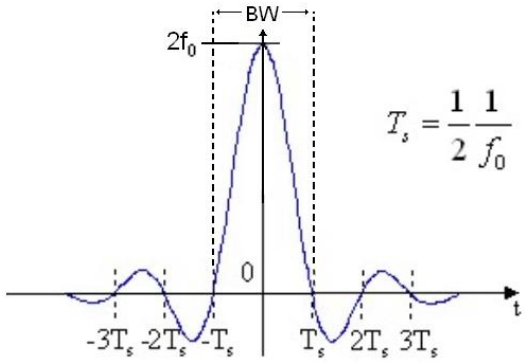

Figure 2.5: Raised cosine pulse

Figure 2.6 shows the procedure for finding channel profile and DME using RT. First RT generates the channel impulse response, and then it passes through a low-pass-filter (raised cosine in here) and creates the channel profile. From a-priori knowledge about the actual distance we can calculate the DME. In our modeling in this chapter the used bandwidth for the simulation is 100 MHZ.

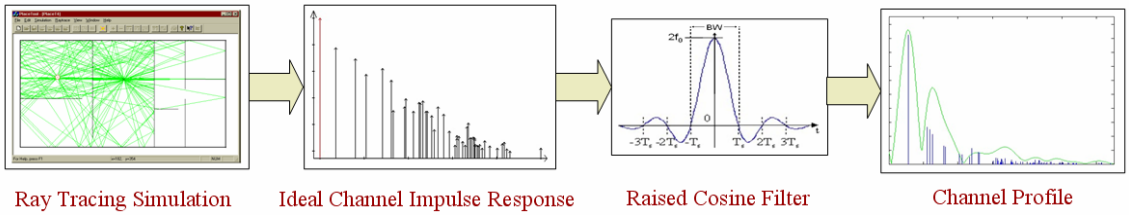

Figure 2.6: Procedure for generating the database of RT channel profiles

2.2.3 Simulation Results

After running simulation for 946 receivers, described in the previous section, the outcomes, which were the raw files of RT, were processed by Matlab® to estimate the distance for each receiver. The estimated distance $\hat{d}$ that is based on TOA measurement, the actual distance between the transmitter and the receiver d, and the distance error ε_d are related to each other based on (1-3). The scatter plot of distance error vs. distance

for all 946 points with bandwidth equal to 100 MHz is shown in Fig. 2.7. In this plot the vertical axis represents the DME and the horizontal axis represents the actual distance.

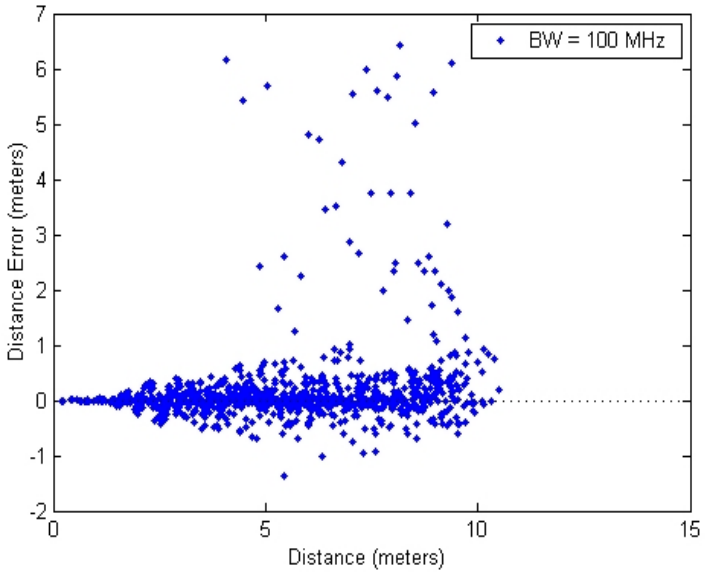

Figure 2.7: Scatter plot of DME derived from simulation results (RT) at 100 MHz bandwidth

2.3 DME Modeling

2.3.1 Modeling Strategy

Characteristics of the distance error in LOS and obstructed LOS (OLOS) environments are substantially different. To make the modeling closer to reality, the receiver locations were partitioned into LOS and OLOS classes. The total number of LOS receivers is 308, and total number of OLOS receivers is 638, where adding them together results in 946 as the total number of points.

2.3.2 Modeling the LOS Case

Figure 2.8 shows the scatter plot for the LOS case. By looking at the scatter plot of Fig. 2.8, two major features are visible in behavior of the distance error for the LOS case. The first one is the increase of the distance error with increasing the actual distance. Because as transmitter and receiver become further separated from each other, the number of reflected paths and their relative power with respect to the first path power both increase, making detection of the TOA of the first path more difficult.

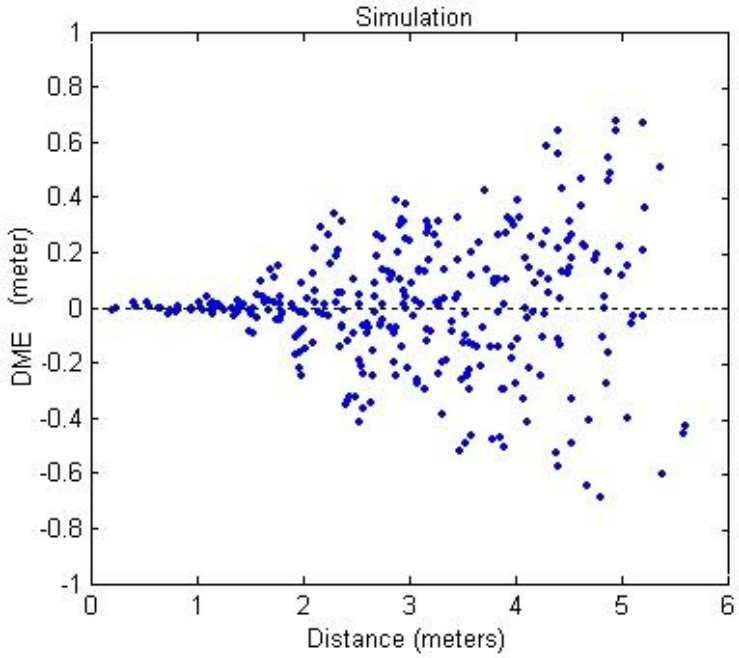

Figure 2.8: Scatter plot of DME for LOS case from RT at 100 MHz bandwidth

The second issue is the symmetry of the scatter plot across the zero line. This feature can be acceptable when we consider that the values of the distance errors are small with respect to actual distance. Since the estimated distance is always positive, from (1-3) it can be shown that the distance error is always greater than or equal to the negative of actual distance ($DME \geq -d$).

Using the first mentioned feature, we define a parameter named normalized DME γ, which is defined in (2-1).

$$\gamma = \frac{DME}{d} \tag{2-1}$$

Fig. 2.9 shows the scatter plot of the normalized DME for LOS. It can be seen that the behavior of γ is not related to the distance. Using (1-3) and (2-1) one can rearrange (1-3) to obtain $\hat{d}$ from

$$\hat{d} = d(1+\gamma) \tag{2-2}$$

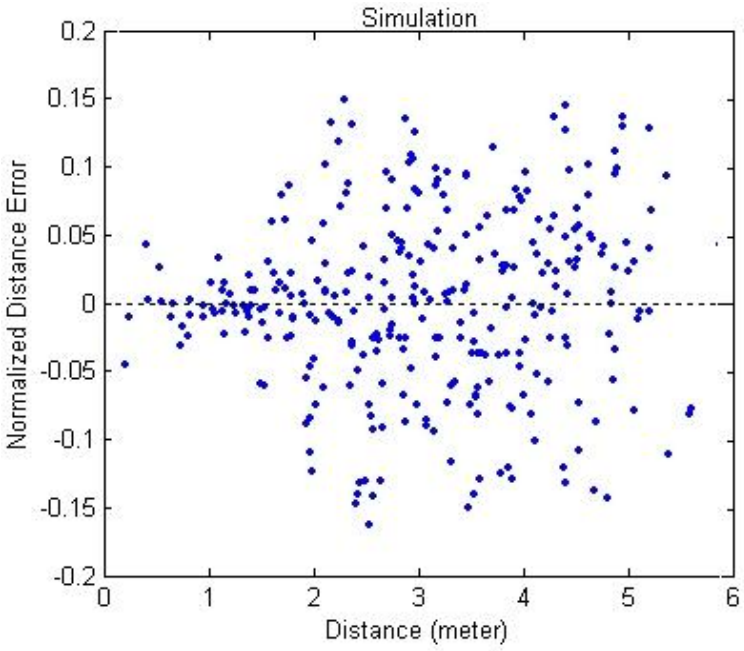

Figure 2.9: Scatter plot of normalized DME for LOS case from RT at 100 MHz bandwidth

We assume that γ has Gaussian distribution with zero mean and variance σ_L^2 derived from simulation results in Fig. 2.9, which in this case σ_γ is equal to 6cm. Fig.

2.10 shows the generated sample points with Gaussian distribution using "randn" function in Matlab®. From now on we refer to such a distribution as $G(0, \sigma_L)$.

Then for generating distance error comparable with the one in Fig. 2.8, using (2-1) and generated normalized distance error, Fig. 2.10, we generate the distance error as shown in Fig. 2.11. To compare the model with the simulation, CCDF of both simulation and model has been calculated and is shown in Fig. 2.12.

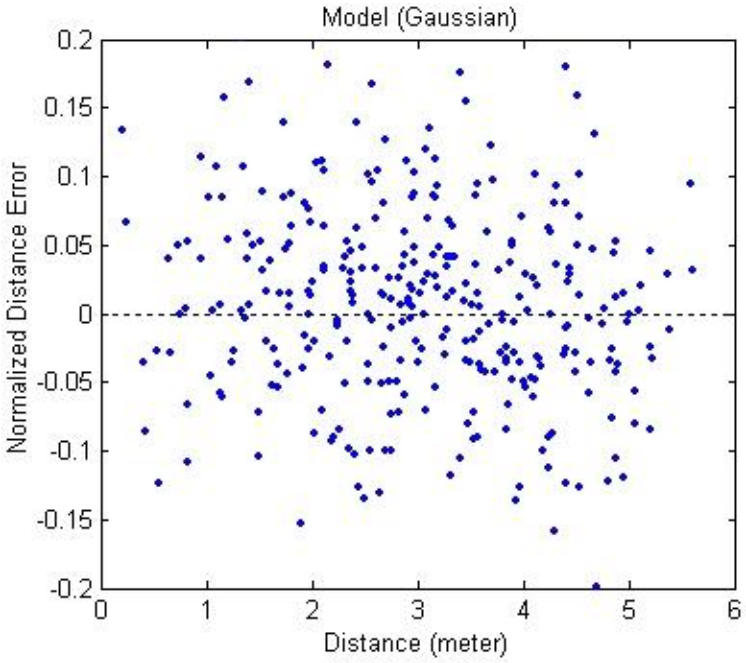

Figure 2.10: Scatter plot of normalized DME for LOS case generated from the Gaussian model

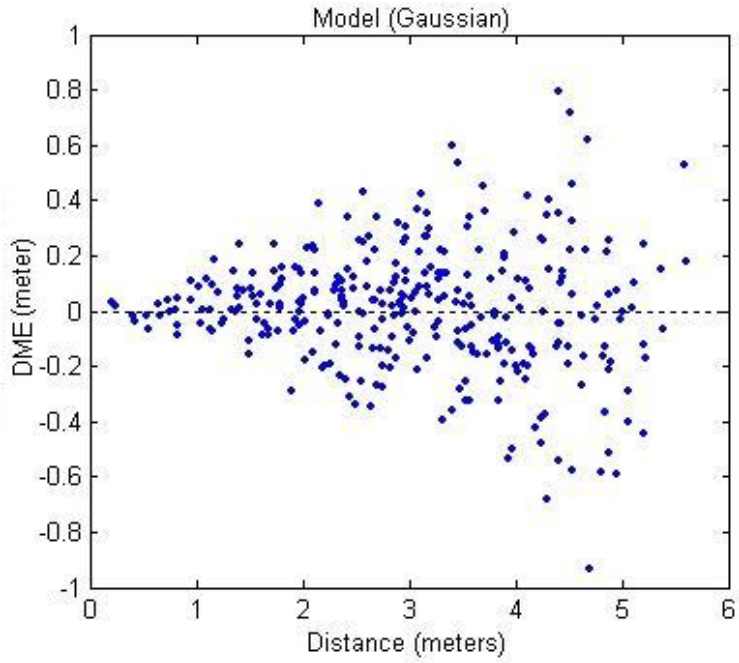

Figure 2.11: Scatter plot of DME for LOS case generated from the model

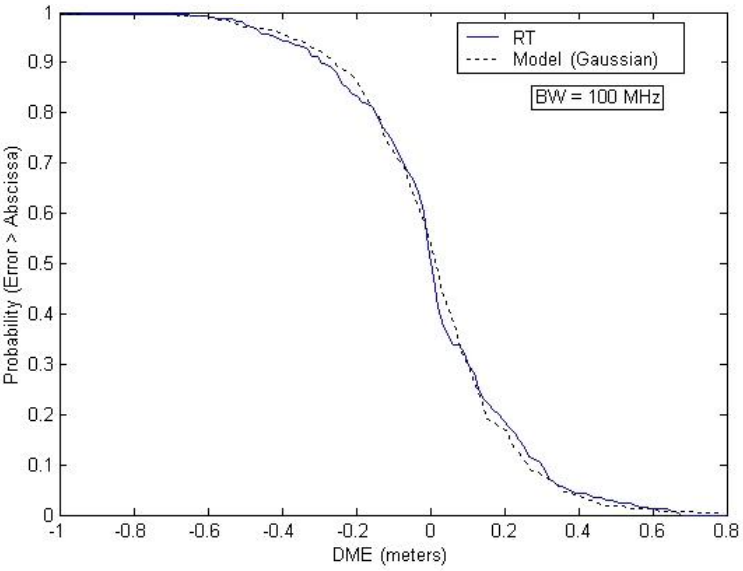

Figure 2.12: Comparison between CCDFs of DME from RT and model for LOS

Fitting the simulation results with the Gaussian model for normalized error illustrates that distance error has a linear relationship to actual distance, and Gaussian distribution of normalized error was a good assumption. But it must be emphasized that

with lower bandwidth, since the magnitude of distance error increases, assuming Gaussian distribution is not as real as in this case, and it needs further work.

We can summarize the model as follows,

$$\hat{d} = d\left(1 + G\left(0, \sigma_L\right)\right) \qquad \text{(2-x)}$$

To use this model for generating a set of distance estimations $\hat{d}$ one must first generate a set of samples of γ with the distribution G(0, σ_L), where σ_L = 6cm, then using the distance set and (2-2) the set of $\hat{d}$ can be obtained.

2.3.3 Modeling the OLOS Case

Using the same bandwidth, we produced "DME" and "Normalized DME" from RT for the OLOS case. Fig. 2.13 shows the scatter plot of DME vs. distance. As it can be seen from the figure, this time, neither DME nor normalized DME points (not presented) are symmetric around the zero line. The reason is that because LOS is not present, detecting the first path is more difficult and the error magnitudes are greater those observed in the LOS case. Also there are some outlying points with very complicated behavior caused by the multipath effect. These points have quite greater amount of distance error, and their distribution does not seem to be Gaussian. In the following chapters we investigate these points in greater detail.

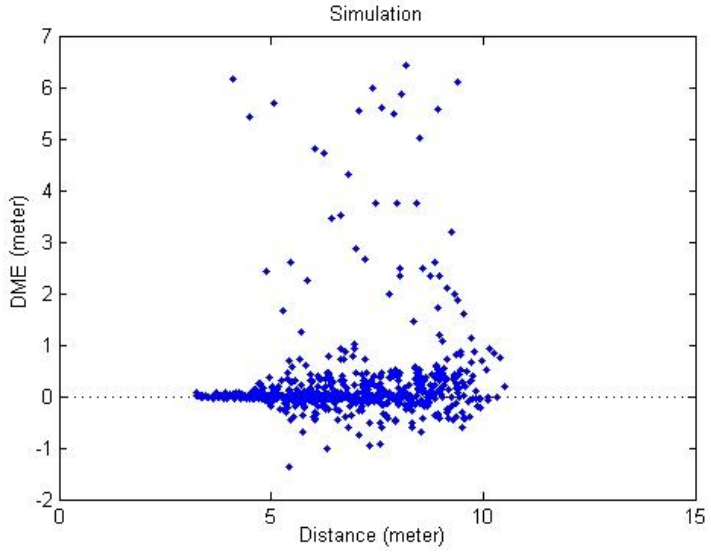

Figure 2.13: Scatter plot of DME for OLOS case from RT at 100 MHz bandwidth

For modeling the OLOS case, a mixture of two functions is considered as the distribution of normalized distance error. The first one, which contains the normal points, follows a Gaussian distribution. The second one, which contains those outlying points mentioned before, modeled with exponential distribution. Fig. 2.14 shows the mixture probability distribution function, consisting Gaussian and Exponential PDFs.

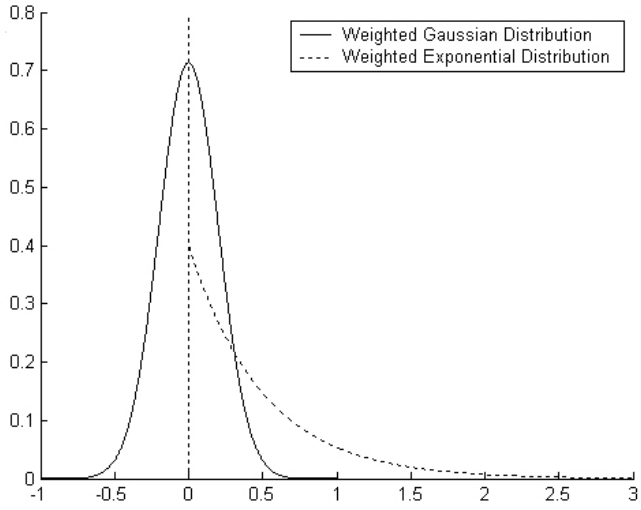

Figure 2.14: Visualization of mixture of Gaussian and Exponential PDF's

To make the integral of the sum of both PDF's equal to one; we have to assign a weight to each PDF. The weights are directly related to the number of points in each type of distribution, if we consider the number of Gaussian points N_G and the number of Exponential points N_{Exp} then we have

$$\text{Total number of points} = N_{Total} = N_G + N_{Exp} \tag{2-3}$$

$$\text{Weight of Gaussian PDF} = W_G = \frac{N_G}{N_{Total}} \tag{2-4}$$

$$\text{Weight of Exponential PDF} = W_{Exp} = \frac{N_{Exp}}{N_{Total}} \tag{2-5}$$

If we assume that the name of the stated PDF is *P(x)* then *P(x)* is equal to

$$P(x) = P_{-}(x) + P_{+}(x) \tag{2-6}$$

$P_{-}(x)$ refers to the negative side of the PDF and $P_{+}(x)$ to the positive side. To find the number of points with Gaussian distribution, we count the number of negative points (N_{-}), and since the Gaussian distribution is symmetric, then number of points with Gaussian PDF is equal to twice as the number of negative points. So, we have:

$$N_G = 2 \times N_{-} \tag{2-7}$$

$$N_{Exp} = N_{Total} - N_G \tag{2-8}$$

The next step is finding the mean and variance of the Gaussian distribution. According to assumption, mean is equal to zero. To find the variance, if we only

consider the negative part of the mix distribution, it is like to define a new PDF as depicted in (2-9). The same definition can be considered for the positive part as $g_{+}(x)$.

$$g_{-}(x)=\begin{cases}\dfrac{2}{\sqrt{2\pi}\sigma_G}e^{\frac{-x^2}{2\sigma_G^2}} & x<0\\ 0 & x\geq 0\end{cases} \tag{2-9}$$

To find the mean of $g_{-}(x)$, using partial integration results to the following equation.

$$\overline{g_{-}(x)}=-\sqrt{\frac{2}{\pi}}\,\sigma_G \tag{2-10}$$

Then using (2-6) and "`mean`" function of Matlab®, variance of the Gaussian part of the mixed distribution can be found. Exponential distribution function has the form of (2-11) [Ros76].

$$e(x)=\begin{cases}\lambda e^{-\lambda x} & x\geq 0\\ 0 & x<0\end{cases},\qquad \overline{e(x)}=\frac{1}{\lambda} \tag{2-11}$$

Using (2-6), (2-9), and (2-11), we can rewrite (2-6) to the form of

$$P(x)=W_G\times G(0,\sigma_G^2)+W_{Exp}\times e(x) \tag{2-12}$$

To find the amount of "λ" for the exponential distribution, taking mean from $P_{+}(x)$ will result to (2-13), which is suitable to obtain "λ".

$$\overline{P_{+}(x)}\times N_{+}=\overline{g_{+}(x)}\times\frac{N_G}{2}+\overline{e(x)}\times N_{Exp} \tag{2-13}$$

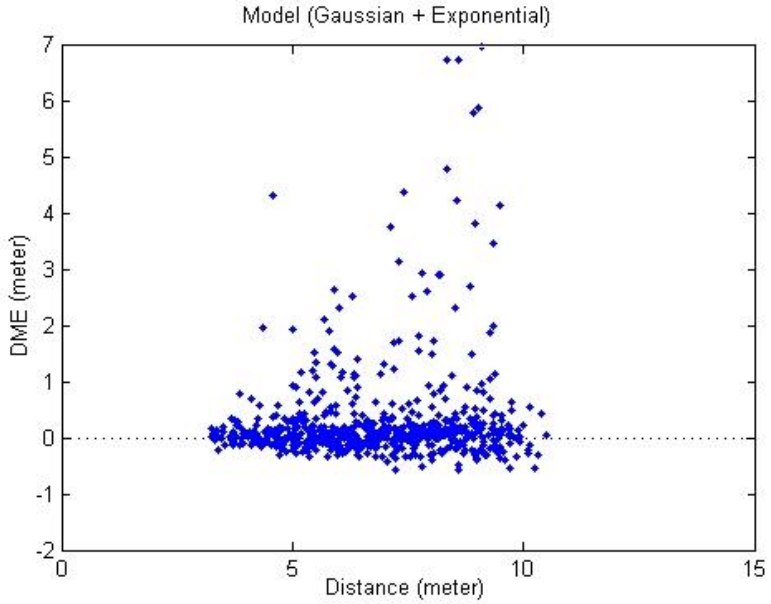

Figure 2.15: Scatter plot of DME for OLOS case from Gaussian+Exponential model at 100 MHz bandwidth

After obtaining required parameters from the simulation results, we used them to generate appropriate number of points for each part and mixing them together. Then using (2-2), DME's were generated, which are shown in Fig. 2.15. If we use the simple Gaussian method used for LOS, the result will be equivalent to 2.16. Fig. 2.17 shows the CCDF of both models compared to the simulation results, and thus the new PDF fits better than the simple Gaussian one. Finally the estimated distance model for the OLOS case can be written as,

$$\hat{d} = d + W_G \cdot G\left(0, \sigma_G\right) + W_{Exp} \cdot Exp\left(\lambda\right). \tag{2-14}$$

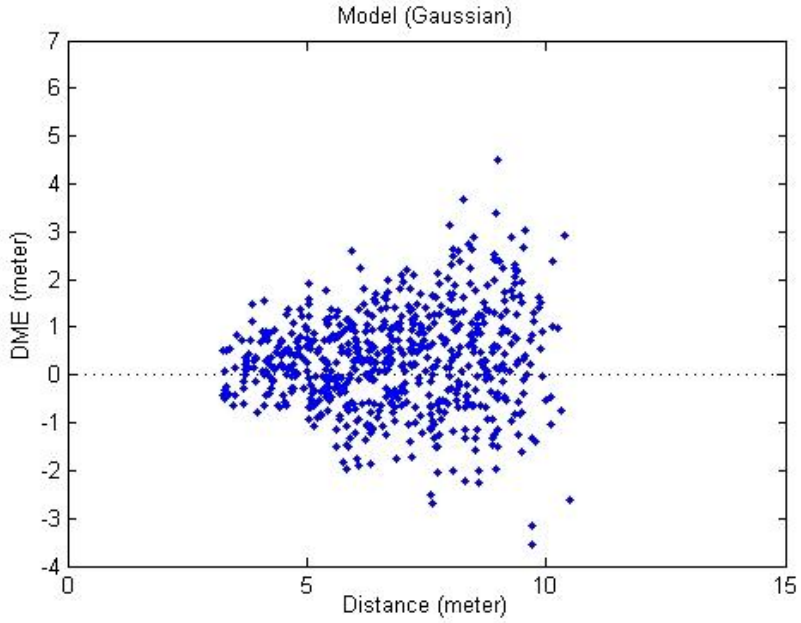

Figure 2.16: Scatter plot of DME for OLOS case from Gaussian model at 100 MHz bandwidth

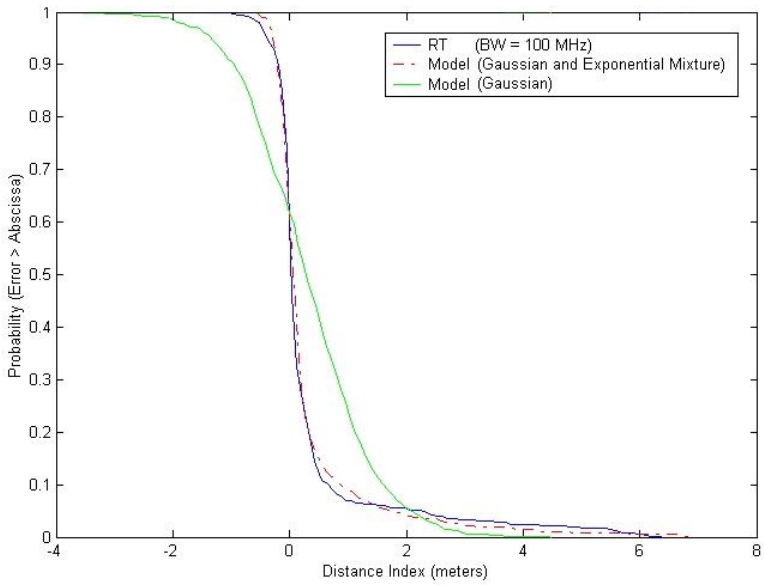

Figure 2.17: Comparison between CCDFs of DME from RT and two models for OLOS

2.4 Summary

We have modeled the estimated distance from TOA of the DP. Ray Tracing software has been used as a simulation tool for generating the database. We have shown that the behaviors of the channel for LOS and OLOS cases are different, and two models have been introduced for LOS and OLOS case, for bandwidth of 100 MHz. The models are summarized in the following equation.

$$\hat{d} = d + \begin{cases} d \cdot G\left(0, \sigma_L\right) & LOS \\ W_G \cdot G\left(0, \sigma_G\right) + W_{Exp} \cdot Exp\left(\lambda\right) & OLOS \end{cases} \tag{2-15}$$

Table 2.1: Typical values of model parameters for 100 MHz bandwidth

	Number of Points	Gaussian PDF Parameters	Exponential PDF Parameters
LOS	$N = 308$	$N = 308\ \sigma_L = 0.06$	N/A
OLOS	$N = 638$	$N_G = 504\ \sigma_G = 0.028\ W_G = 0.79$	$N_{Exp} = 134\ \lambda = 5.3\ W_{Exp} = 0.21$

We have shown that for the LOS case; where the amount of error is relatively small, a zero mean Gaussian distribution for normalized DME could closely model the distance error. For the OLOS case, we have shown that the Gaussian model is not suitable, and instead we have introduced a mixture distribution, containing zero mean Gaussian and Exponential distribution that fits the distance error very well. Table 2.1 shows typical values of model parameters obtained from the results of the simulation for 100 MHz bandwidth.

Chapter 3

Modeling the Effect of Bandwidth

3.1 Introduction

In chapter 2 we introduced a framework for indoor geolocation including the concept of DME. We showed that the DME depends on the distance and the scenario of the radio propagation channel. In this chapter we want to study the effect of system bandwidth in the accuracy of indoor geolocation systems, DME is a good representative for this measure. We use RT similar to chapter 2 and we change the bandwidth of the system by changing the raised cosine filter bandwidth. First we show the effect of bandwidth on channel profile and DME and then we extend our introduced model in chapter 2 to include the bandwidth effect.

3.2 Effect of Bandwidth on DME

In practice the accuracy of measurement of the DP is a function of system bandwidth. In another word DME is a function of bandwidth. To show the effects of

bandwidth, four channel profiles, with four different bandwidths, have been produced and shown in Fig. 3.1. All of these channel profiles are related to one pair of Tx/Rx that is shown in Fig. 2.4, the Tx is shown with a circle and Rx is shown with a bold "X". The same procedure demonstrated in Fig. 2.6 has been used to generate these channel profiles.

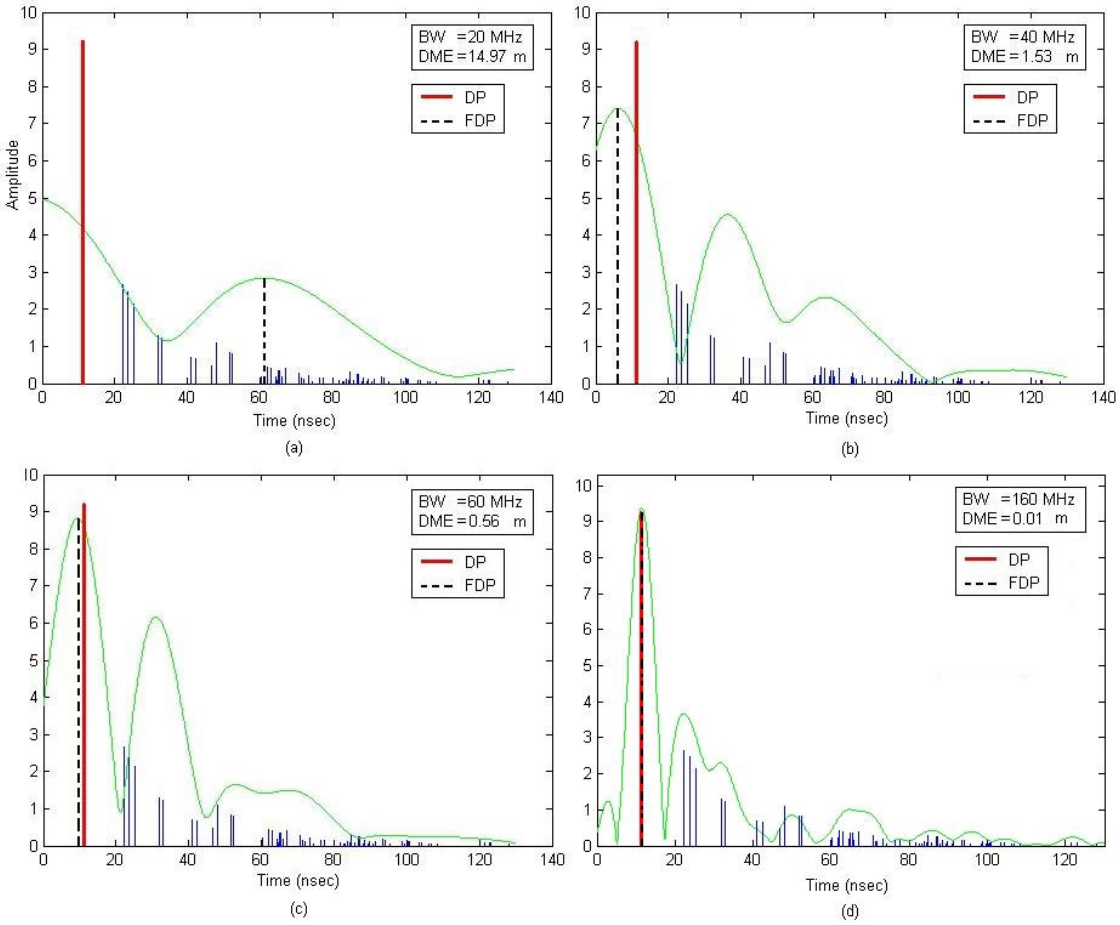

Figure 3.1: Channel profiles generated from RT, using one pair of Tx/Rx, with different bandwidths: (a) 20MHz, (b) 40MHz, (c) 60MHz, and (d) 160MHz

It can be seen that as the bandwidth increases the channel profile shapes become more and more similar to ideal channel profile, i.e. channel impulse response. At the same time by increasing the bandwidth the DME decreases.

3.3 DME Modeling as a Function of Bandwidth

3.3.1 Modeling Strategy

This section is very similar to section 2.3 with the difference that here we have a new parameter called "*W*" that represents the system bandwidth and usually occurs in as a subscript.

Also, similarly we have partitioned the area into LOS and OLOS areas. In LOS region the minimum distance is close to zero and the maximum distance is around 5.5 meters. In OLOS region the distance varies between 3 to 11 meters.

To incorporate the effect of bandwidth, here we redefine DME from (1-3) as,

$$DME_W = \hat{d}_W - d \ . \tag{3-1}$$

3.3.2 LOS Modeling

Figure 3.2 shows the scatter plots of DME_W derived from the simulation results for two different bandwidths 50 and 500 MHz. As we discussed in chapter 2, to model the increase of DME_W with increasing the distance, we use the same normalization technique. The normalized distance error is defined in (3-2), and for the LOS case it is shown as γ_{Lw}. Here the subscript "*L*" stands for LOS.

$$\gamma_{L,W} = \frac{DME_{L,W}}{d} \tag{3-2}$$

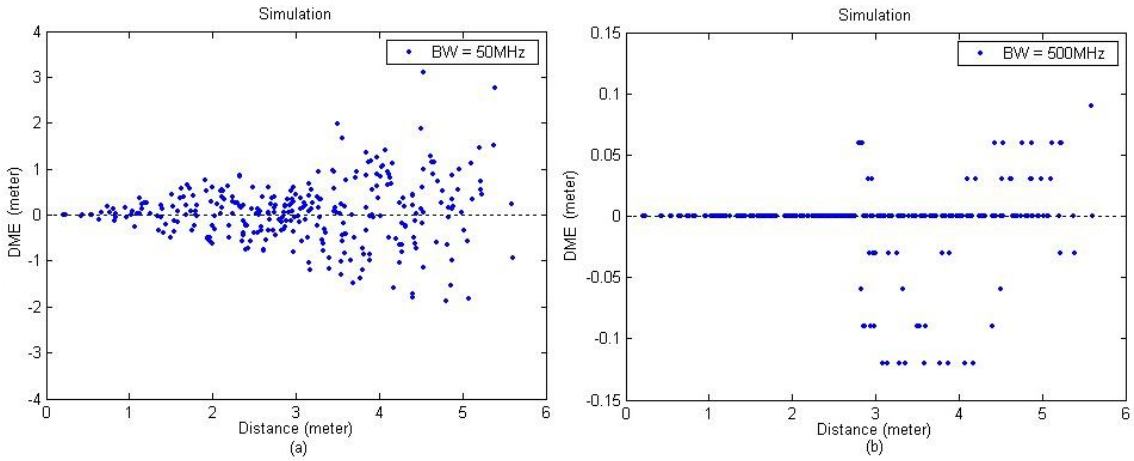

Figure 3.2: Scatter plots of DME for LOS derived from RT for (a) *W* = 50 MHz (b) *W* = 500 MHz

This definition results in a general form of representing the estimated distance in terms of normalized distance error,

$$\hat{d}_{L,W} = d\left(1+\gamma_{L,W}\right). \tag{3-3}$$

Similar to chapter 2, we assume that $\gamma_{L,W}$ has zero mean Gaussian distribution with variance derived from the simulation results, which has the form of

$$f\left(\gamma_{L,W}\right) = \frac{1}{\sqrt{2\pi}\sigma_{L,W}} e^{-\frac{\gamma_{L,W}^2}{2\sigma_{L,W}^2}} \tag{3-4}$$

where $\sigma_{L,w}$ is the standard deviation (STD) of $\gamma_{L,W}$.

Figure 3.3 shows the corresponding normalized DME for the points that are shown in Fig. 3.2. We used (3-3) to derive the normalized DME.

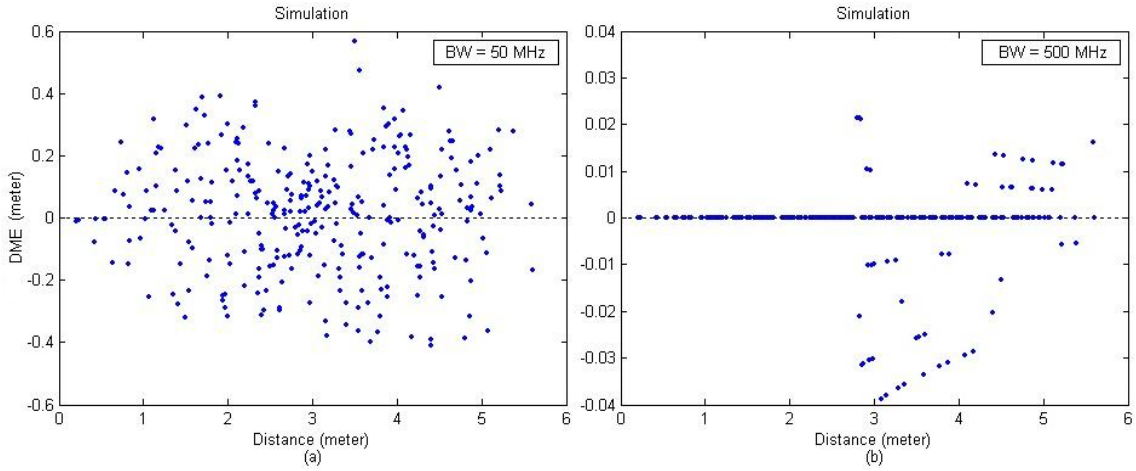

Figure 3.3: Scatter plots of normalized DME for LOS derived from RT for (a) W = 50 MHz (b) W = 500 MHz

Figure 3.4 shows the generated normalized distance errors from the introduced model in (3-4) for the normalized DME. The plots correspond to Figs. 3.3 and have the same number of points and variances as their simulation version.

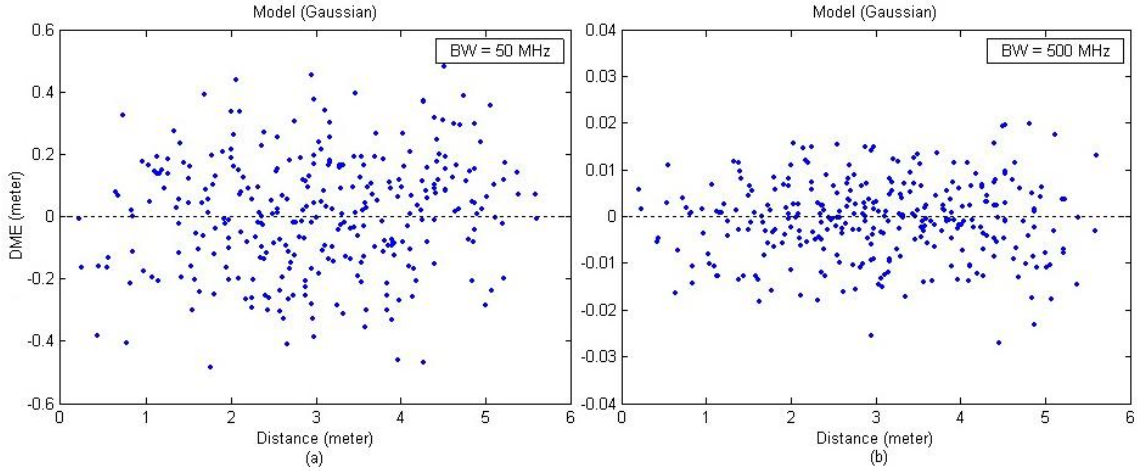

Figure 3.4: Scatter plots of normalized DME generated from model for (a) W = 50 MHz (b) W = 500 MHz

To generate the distance error sets we can rewrite (3-2) as

$$DME_{L,W} = \gamma_{L,W} \times d \ , \tag{3-5}$$

and using the distance set that we used for the simulation phase, we can derive the distance errors. The results are shown in Fig. 3.5.

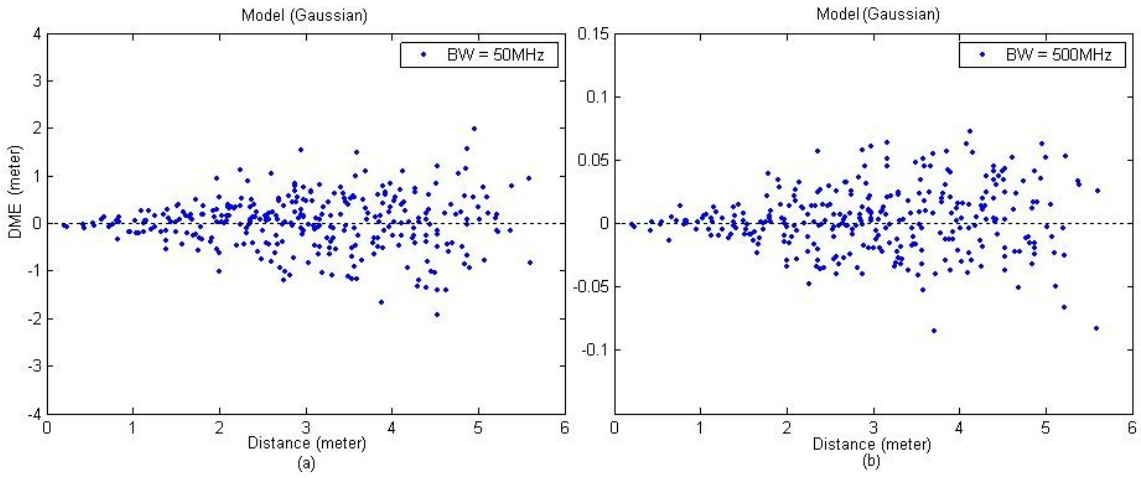

Figure 3.5: Scatter plots of DME for LOS generated from model for (a) *W* = 50 MHz (b) *W* = 500 MHz

To measure the similarity of the introduced model with the results of simulation, complementary CDF has been used. The complementary CDF curves for two bandwidths 50 and 500 MHz are shown in Fig. 3.6-(a), (b). It can be seen that for higher bandwidths the CCDF curve doesn't resemble the Gaussian shape. This is due to quantization error in the time axis of channel profiles. In addition, decreasing the time step can solve this problem but the amount of DME and the fitting error (discussed in the next paragraph) is so small that it makes this approximation quite accurate. This quantization effect can be clearly seen on figures 3.2-(b) and 3.3-(b).

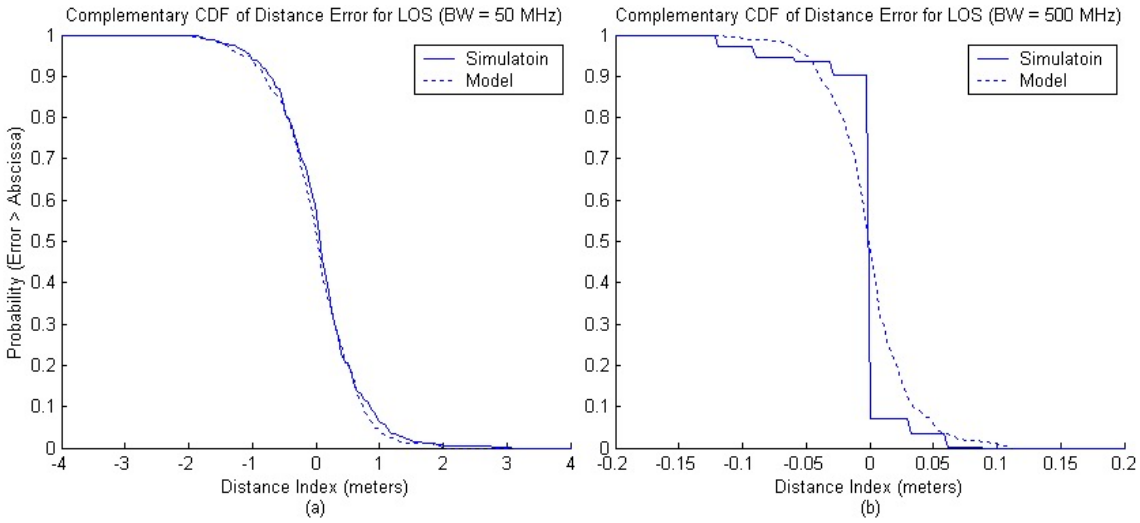

Figure 3.6: Comparison between complementary CDFs of DME for LOS, (a) *W* = 50 MHz, (b) *W* = 500 MHz

To show how closely the CDF curve of the model follows the CDF curve of the simulation, we defined a new parameter, which is called average fitting error or ε_{fit}. The average fitting error is defined as the average of the horizontal difference between the curves of the simulation and the model and it is derived from the area created between these two curves. Table 3.1 shows the standard deviation of the normalized distance error and the average fitting error for 9 different bandwidths from 30 to 3000 MHz. Figure 3.7 shows the two parameters $\sigma_{L,W}$ and ε_{fit} versus *1/W*, as it can be seen the model fits well until the lower limit of 40 MHz. Based on these results and from polynomial fittings (3-6) introduces an equation to find σ_{Lw} in cm, where A_L=52691, B_L=0.43, m_L=10^{-4}, and *W* is the bandwidth in MHz $(W \geq 40MHz)$.

$$\sigma_{L,W} = A_L(\frac{1}{W} - m_L)^2 + B_L \qquad (3\text{-}6)$$

Table 3.1: Typical values of model parameters and the fitting error for different bandwidths for LOS

w (MHz)	σ_{Lw} (cm)	ε_{fit} (cm)
30	34.33	29.40
40	34.33	15.34
50	19.06	5.57
100	6.48	2.59
200	2.6	2.54
500	0.83	1.60
1000	0.27	0.58
2000	2.1e-14	3.4e-14
3000	2.1e-14	3.3e-14

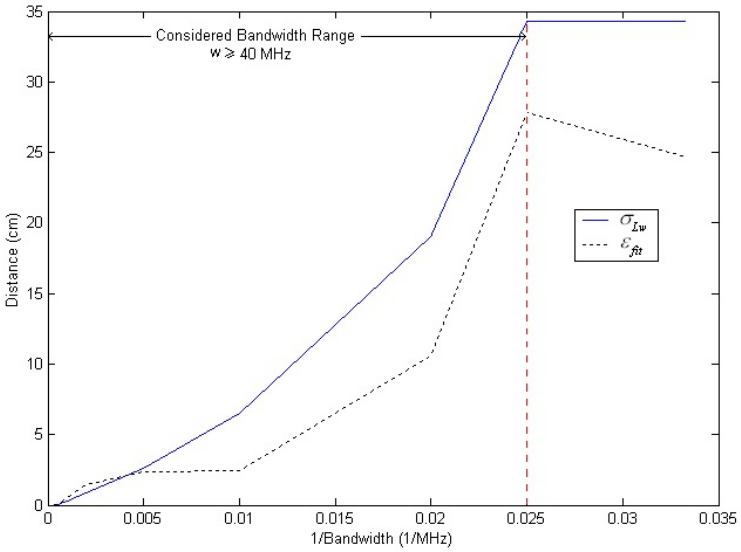

Figure 3.7: Standard deviation of normalized DME (σ) and the average fitting error (ε) vs. $1/W$ for LOS

3.3.3 OLOS Modeling

Figure 3.8 shows the scatter plots of $DME_{O,W}$ derived from the simulation results of OLOS environment for two different bandwidths 50 and 500 MHz. Here, again we used the concept of normalized DME, because of the increase in DME with

increasing the distance. So, the equations (3-2) and (3-3) can be applied for OLOS case as well

$$\gamma_{O,W} = \frac{DME_{O,W}}{d} \tag{3-7}$$

$$\hat{d}_{O,W} = d\left(1+\gamma_{O,W}\right). \tag{3-8}$$

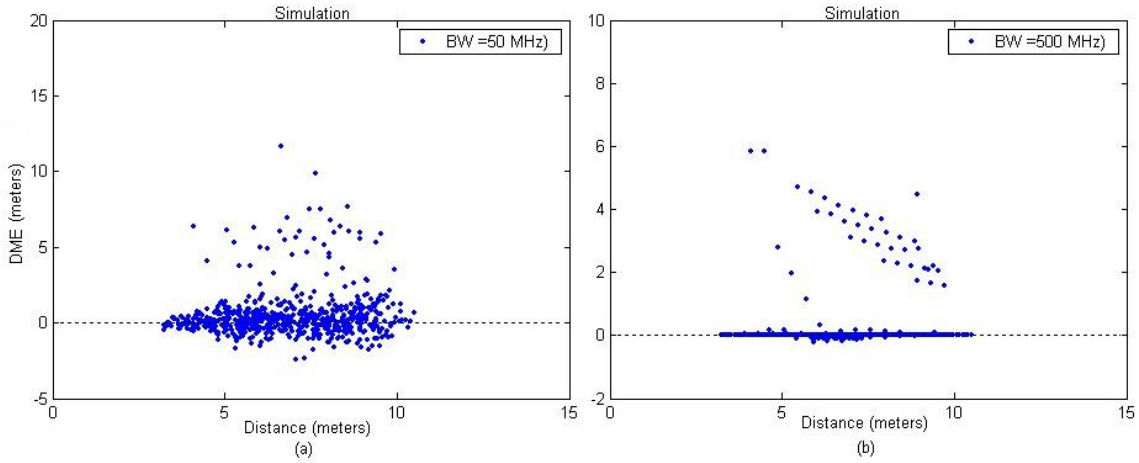

Figure 3.8: Scatter plots of DME for OLOS derived from RT for (a) *W* = 50 MHz (b) *W* = 500 MHz

To estimate the distribution of γ_{Ow} we made the same assumption as in chapter 2, which was a mixture of zero mean Gaussian and Exponential. The distribution of γ_{Ow} can be written in a compact form as

$$f\left(\gamma_{O,W}\right) = W_{G,W}\frac{1}{\sqrt{2\pi}\sigma_{O,W}}e^{\frac{\gamma_{O,W}^2}{2\sigma_{O,W}^2}} + W_{Exp,W}u\left(\gamma_{O,W}\right)\lambda_W e^{-\lambda_W\gamma_{O,W}} \tag{3-9}$$

where $W_{G,W}$ and $W_{Exp,W}$ are the weights of the Gaussian and Exponential parts, u is a step function, σ_{Ow} is the STD of Gaussian distribution, and λ_w is the Exponential distribution parameter.

To extract the parameters for OLOS we used the same technique that has been used in chapter 2 with a small modification. As it can be seen from table 3.1, for high bandwidths DME dramatically decreases, in such a way that it goes beyond the simulation resolution. In those cases the data does not seem to be correct anymore and most of the points have equal distance error, which makes the distribution have a delta function close to zero causing error in parameter calculations. To overcome this problem we divided the distance error region into three sections, middle, negative, and positive. The middle section is a very narrow (with a constant width of Δ=0.002) region between the positive and negative regions. Then, we counted half of the middle points as negative and half as positive. Figure 3.9 shows the distribution and the partitioning technique. To derive the parameters, first from the number of negative and positive points we find the values of W_{Gw} and W_{Expw}, Then we calculate the mean of the negative section assuming that mean of the middle points is -Δ/2, and after calculating σ_{Ow} we calculate the mean of the positive part assuming that mean of the middle points is Δ/2 to derive λ_w.

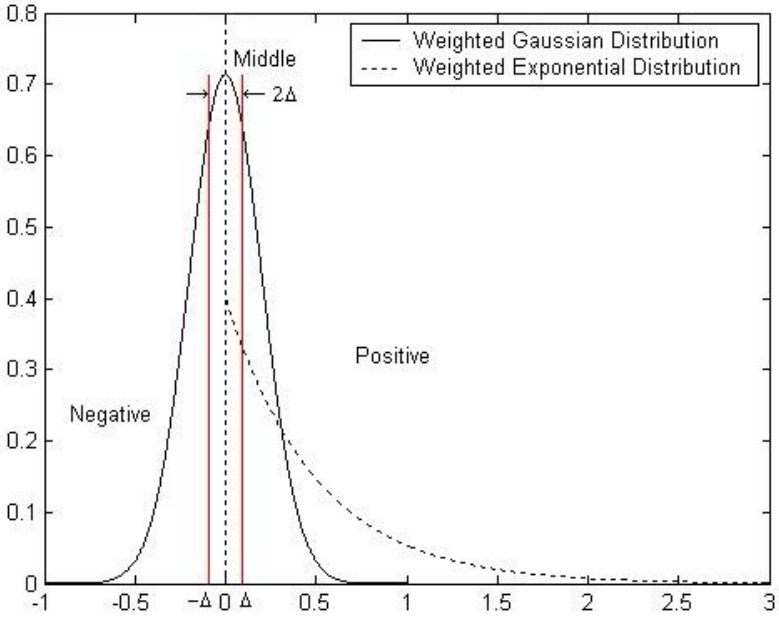

Figure 3.9: Assumed distribution for the OLOS with the partitioning

Figure 3.10 shows the generated DME using the normalized DMEs in (3-8) from the introduced model in (3-9); these scatter plots correspond to Fig. 3.8 and have the same number of points as their simulation version.

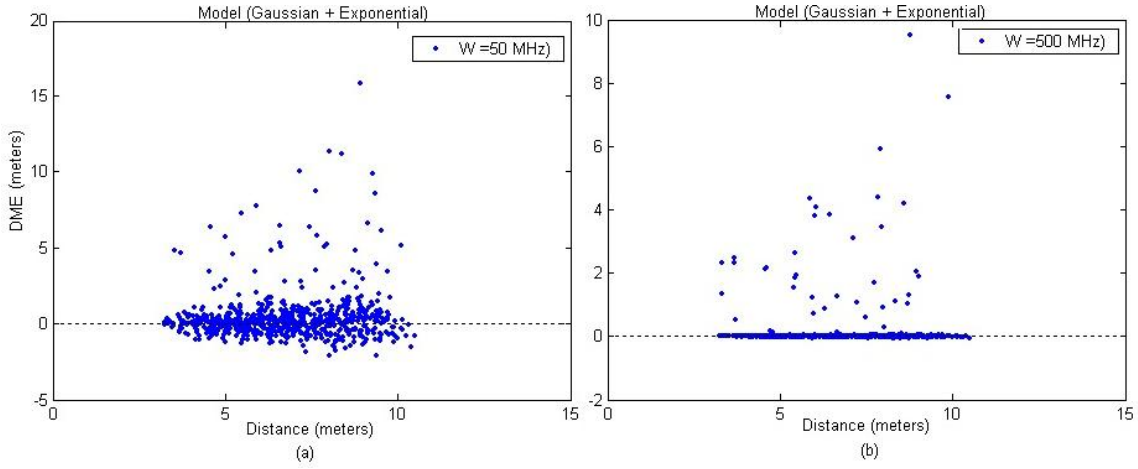

Figure 3:10: Scatter plots of DME for OLOS generated from model for (a) *W* = 50 MHz (b) *W* = 500 MHz

It can be seen that the Exponential part in distance errors has not decreased like the Gaussian part. To compare these scatter plots, Fig. 3.11 shows the CCDFs of DME for 50 and 500 MHz bandwidths for the OLOS case. To illustrate that the Gaussian model used for LOS does not fit for the OLOS case we include its CDF curve in the figures as well. For 50 MHz bandwidth ε_{fit} is 11 cm for Gaussian Exponential mixture and 65 cm for Gaussian, while for 500 MHz they are 6 and 63 cm.

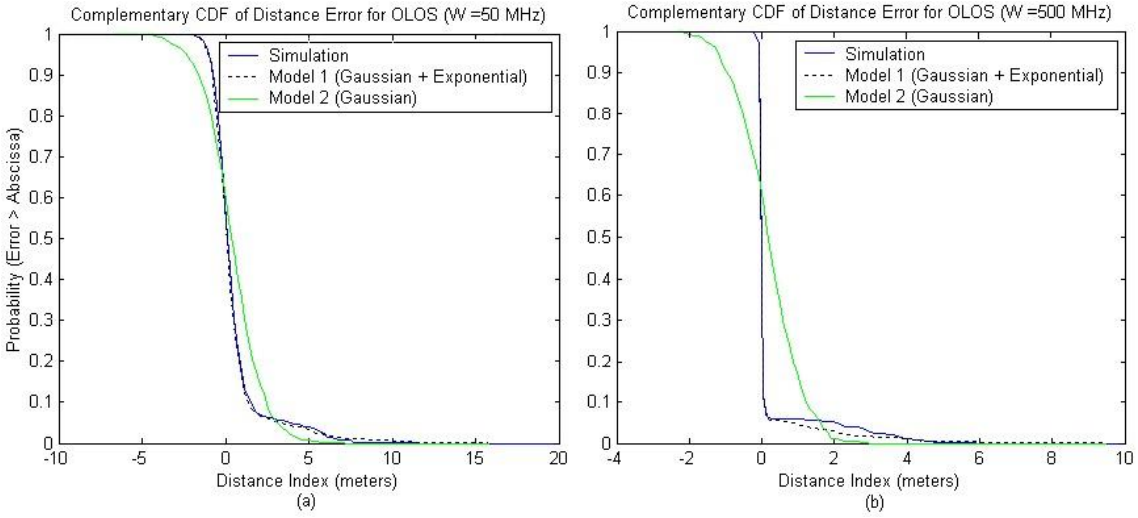

Figure 3.11: Comparison between complementary CDFs of DME for OLOS, (a) *W* = 50 MHz, (b) *W* = 500 MHz

Table 3.2 shows the typical values of model parameters for different bandwidths, and the corresponding average fitting error values. To use the polynomial fitting we need to sketch them versus 1/*W*, as it is shown in Fig. 3.12. For the OLOS case the considered bandwidth range, which is used for polynomial fit, is from 30 to 3000 MHz. Similar to (7), from the results of second order polynomial fit (3.10) introduces an equation to find $\sigma_{O,W}$ in cm, where A_O=9052, B_O=2.6, m_O=0.16, and W is in MHz.

$$\sigma_{O,W} = A_O(\frac{1}{W} - m_O)^2 + B_O \tag{3.10}$$

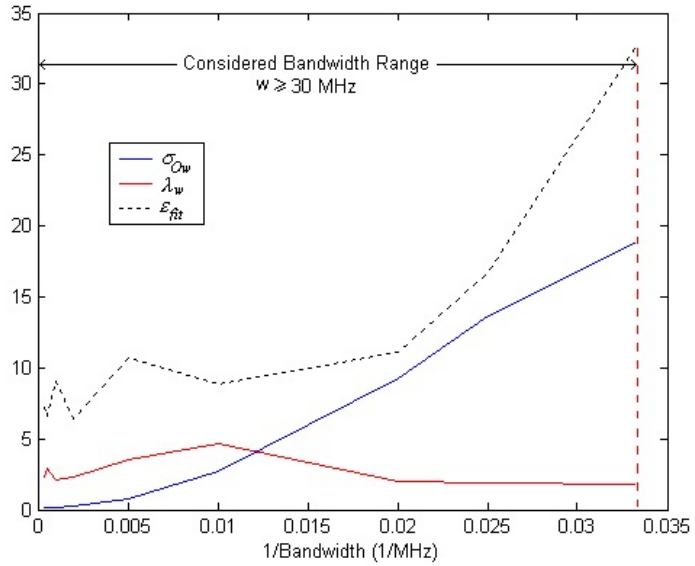

Figure 3.12: Model parameters for OLOS (σ and λ) and the average fitting error (ε) vs. $1/W$

Table 3.2: Typical values of model parameters and the fitting error for different bandwidths for OLOS

w (MHz)	σ_{Ow} (cm)	(m^{-1}) λ_w	ε_{fit} (cm)
30	18.86	1.75	32.85
40	13.71	1.92	16.70
50	9.27	1.98	11.13
100	2.67	4.67	8.84
200	0.78	3.50	10.70
500	0.29	2.31	6.37
1000	0.15	2.07	9.02
2000	0.13	2.93	6.64
3000	0.13	2.27	7.25

Since the variation of λ versus bandwidth is very small, in order to have a simpler model we assumed that its value is constant and equal to its mean, 2.6 m^{-1}.

3.4 Summary

In this chapter we modeled the estimated distance from TOA of the DP with considering the effect of bandwidth. As a continuation of chapter 2 we used RT software as a simulation tool to perform this modeling. Two different models for LOS and OLOS have been introduced and summarized in the following equation.

$$\hat{d} = d + \begin{cases} d \cdot G\left(0, \sigma_{L,W}\right) & LOS \\ d.\left(W_G \cdot G\left(0, \sigma_{O,W}\right) + W_{Exp} \cdot Exp\left(\lambda\right)\right) & OLOS \end{cases} \tag{3-11}$$

It was shown that the Gaussian part of the DME decreases with increasing the bandwidth but the exponential part remains the same.

Part II

Distance Measurement Error Modeling Using Ultra-Wideband Measurements

The modeling in Part I included a distance measurement error model considering the effect of bandwidth. Part I modeling has the following deficiencies:

1- It is not based on real data. Rather it uses RT software as a simulation tool.
2- There is no physical association involved on the model.

In Part II we address these issues.

Chapter 4: Measurement database

In this chapter we provide a database of UWB channel measurements that are taken for the purpose of indoor positioning. The measurement consists of two phases including covering variety of building types.

Chapter 5: Preliminary Analysis of UWB Measurements

In chapter 5, we conduct the preliminary analysis on the measurements, including the classification of the scenarios and path-loss modeling, and power based distance measurement error models.

Chapter 6: Modeling of distance measurement error using UWB data

In this chapter we introduce a complete model for distance measurement error addressing all the problems of the part I model, followed by a section for studying the effect of bandwidth on distance measurement errors.

Chapter 4

Measurement Database

4.1 Introduction

The main objective of the indoor channel measurements is to establish a realistic foundation for the evaluation of indoor channel models. Measurements targeted for indoor geolocation application have been collected in Center for Wireless Information Networks (CWINS) since 1998 [Ben99], [Zan03], [Als04], [IWT04], and [IWT05]. In this chapter we provide a comprehensive database of UWB channel measurements directed for positioning application. As through this dissertation the positioning system is time-of-arrival based. Hence the measurements are also TOA-based.

The organization of the chapter is as follows. Section 2 describes the measurement system used in both phases of the project, followed by sections 3 and 4 that are descriptions of phase I and II respectively. And finally section 5 is the summary of the chapter.

4.2 Measurement System

The system used is a frequency-domain measurement system, originally introduced in [How90] and [How91]. It employs a 40GHz Agilent E8363B vector network analyzer that is used to sweep the frequency spectrum of 3-6 GHz for the first phase of measurements and 3-8 GHz for the second phase. We used frequency sampling interval of 1 MHz.

Figure 4.1 shows the measurement system that has been used in phase I of the measurements. The transmitter and the receiver are a pair of disc-cone UWB antennas which are connected to the network analyzer by low-loss cables. On the receiver side a low-noise amplifier (LNA) is connected between the antenna and the network analyzer. The overall measurement system has a noise level of -120 dBm. The undesirable effects of the cables, LNA and antennas are removed through system calibration.

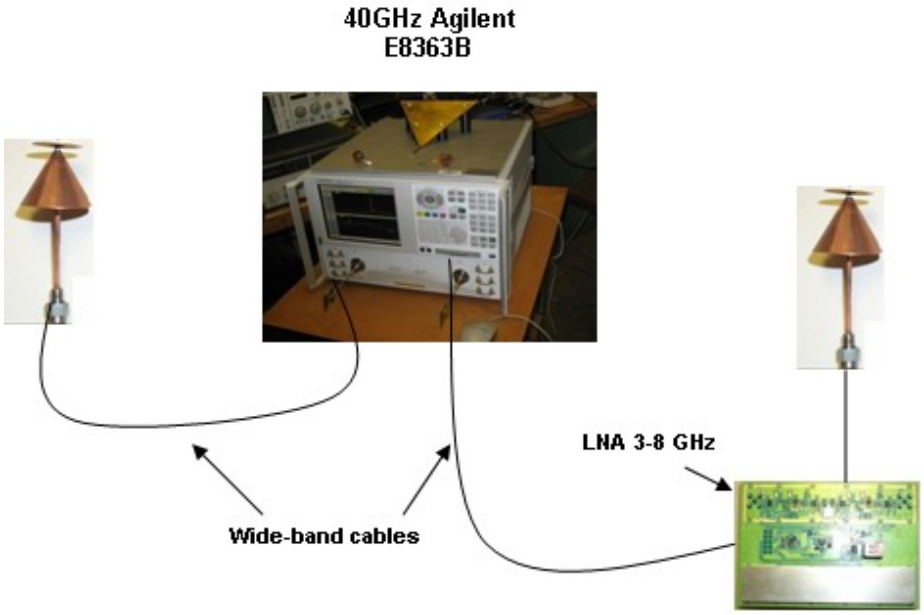

Figure 4.1: Measurement system used for Phase I of UWB Ranging Measurements

In the second phase of the measurements we used a power amplifier in the transmitter side in order to have a larger range of coverage. The power amplifier has 30dB amplification with the frequency range of 2-8GHz, which overall the system was able to measure from 3 to 8 GHz. Figure 4.2 shows the block diagram of this system.

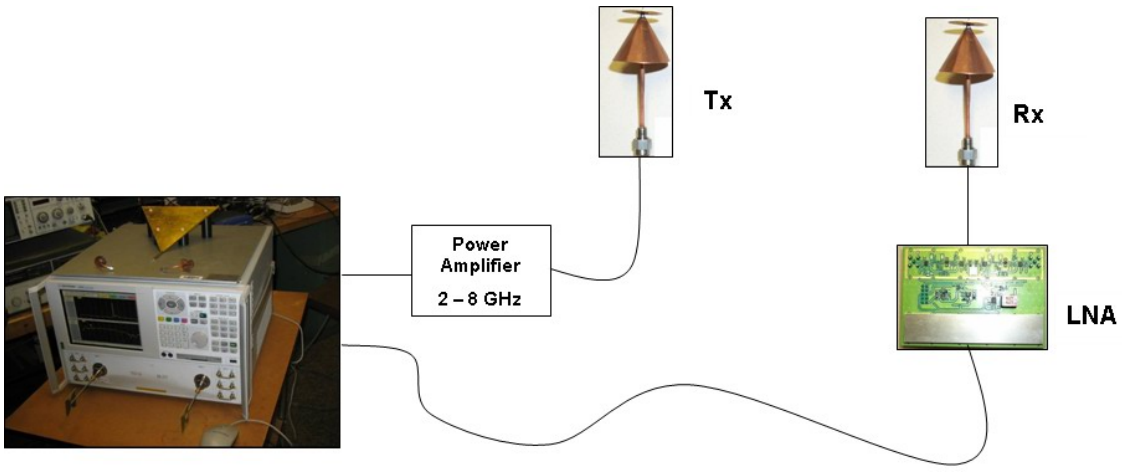

Figure 4.2: Measurement system used for Phase II of UWB Ranging Measurements

System calibration involves connecting the cables back-to-back without the antennas. This will remove the delay and attenuation of the cables. The second step to system calibration is connecting the antennas and performing a 1-meter LOS free space calibration. This removes the delay and gain caused by the antennas. As a result the CIR after calibration in this case would be a single path occurring at 0 ns.

4.3 Phase I of UWB Measurements

The main purpose of the first set of measurements is to prepare a simple database of a typical indoor environment. We used Atwater Kent (AK) Laboratories building in Worcester Polytechnic Institute (WPI) as the measurement site. This building has the style of a typical office environment, which is a good example of a typical indoor multipath site. The building has three floors and we have done measurements in all of the floors.

In order to provide a variety of choices we performed both indoor-to-indoor (ITI) and outdoor-to-indoor (OTI) channel measurements. First floor has been measured for only OTI cases, while second and third floors have been measured for only ITI cases.

Figure 4.3 shows the floor plan and the measured points that have been done in the first floor. In this figure there are two positions for transmitter, namely, A1 and A2. A1 is chosen to be in front of the entrance and A2 is chosen to be at the back of the building with no access to the entrance.

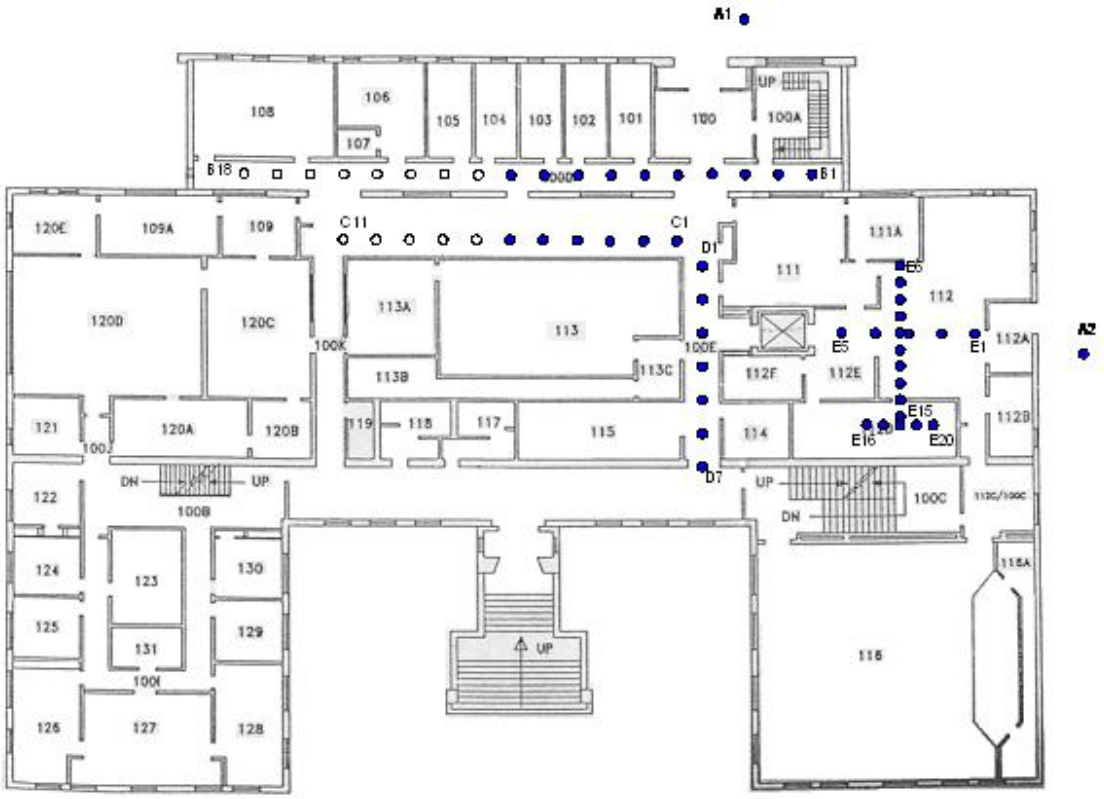

Figure 4.3: Measurement plan at 1st Floor with Tx located at A1 and A2, AK Laboratories

For the Tx location at A1, three sets of measurements have been done, namely: B set, C set, and D set. B set is in the closest corridor to the entrance and includes 10 points. C set is a corridor in parallel with the B set a few meters farther from the entrance and includes 8 points. D set is perpendicular to these sets and is in another corridor and includes 7 points. Each point in these three sets is 2 meters apart from its consecutive point. Table 4.1 shows the distances between Rx and Tx for these sets of measurements.

Table 4.1: Measured distances from Tx located at A1

B1	10.03	C1	13.71	D1	15.24
B2	9.41	C2	14.42	D2	17.21
B3	9.2	C3	15.36	D3	19.19
B4	9.41	C4	16.49	D4	21.18
B5	10.03	C5	17.78	D5	23.17
B6	10.98	C6	19.18	D6	25.15
B7	12.19	C7	20.69	D7	27.14
B8	13.59	C8	22.27		
B9	15.12				
B10	16.75				

For the Tx location at A2, only one set, E, has been done. But E set measurements are 20 points and have been performed in three different rooms. E1 to E5 are in one room, E6 to E15 are in the second room, and E16 to E20 are in the third room. Each point in these three sets is 1 or 2 meters apart from its consecutive point. Table 4.2 shows the distances between Rx and Tx for these sets of measurements.

Table 4.2: Measured distances from Tx located at A2

E1	6.56	E6	12.14	E16	13.62
E2	8.53	E7	11.74	E17	12.67
E3	10.52	E8	11.42	E18	11.73
E4	12.50	E9	11.17	E19	10.81
E5	14.49	E10	11.01	E20	9.89
		E11	10.94		
		E12	10.96		
		E13	11.08		
		E14	11.28		
		E15	11.56		

It must be added that in each Receiver point three sets of measurement has been done. So, the total number of measurements in the first floor is

$$3\times\left(10+8+7+20\right)=135 \tag{4-1}$$

The second floor measurements focused on the effect of inter-office walls where four transmitter locations produced four different measurement scenarios. Figure 4.4 shows the floor plan and the measured points that have been done in the second floor of the AK building. In this figure there are four positions for transmitter, namely, A0, B0, C0, and D0. A0, B0, and C0 are chosen to consider the effect of inner rooms and walls in an office area. Some of these points are LOS and some are OLOS. D0 is chosen to observe the behavior of the channel in a corridor environment; all of these points are ITI and LOS.

Figure 4.4: Measurement plan at 2nd Floor with Tx located at A0, B0, C0, and D0, AK Laboratories

For each of the Tx locations at A0, B0, and C0, the receiver was located at all three rows of A, B, and C, i.e. A1-A8, B1-B8, and C1-C6. So for each of these transmitter positions there is 24 receiver positions assigned. The rows are in parallel with one another with a distance of 90cm, and the distance between each two neighbor points in a same row is 50cm. Table 4.3 shows the distances between Rx and Tx for these sets of measurements.

Table 4.3: Measured distances from Tx located at A0, B0, and C0

Location Name	Tx/Rx	X	Y	Distance to A0	Distance to B0	Distance to C0
A0	Tx	0	0	0	0.9	1.8
A1	Rx	1	0	1	1.34	2.06
A2	Rx	1.5	0	1.5	1.75	2.34
A3	Rx	2	0	2	2.19	2.69
A4	Rx	3	0	3	3.13	3.50
A5	Rx	3.5	0	3.5	3.61	3.94
A6	Rx	4	0	4	4.1	4.39
A7	Rx	4.5	0	4.5	4.59	4.85
A8	Rx	5	0	5	5.08	5.31
B0	Tx	0	0.9	0.9	0	0.9
B1	Rx	1	0.9	1.34	1	1.34
B2	Rx	1.5	0.9	1.75	1.5	1.75
B3	Rx	2	0.9	2.19	2	2.19
B4	Rx	3	0.9	3.13	3	3.13
B5	Rx	3.5	0.9	3.61	3.5	3.61
B6	Rx	4	0.9	4.1	4	4.1
B7	Rx	4.5	0.9	4.59	4.5	4.59
B8	Rx	5	0.9	5.08	5	5.08
C0	Tx	0	1.8	1.8	0.9	0
C1	Rx	1	1.8	2.06	1.34	1
C2	Rx	1.5	1.8	2.34	1.75	1.5
C3	Rx	2	1.8	2.69	2.19	2
C4	Rx	3	1.8	3.50	3.13	3
C5	Rx	3.5	1.8	3.94	3.61	3.5
C6	Rx	4	1.8	4.39	4.1	4

For the Tx location at D0, on total 24 receiver points was located with 1 meter distance between two neighbors. The distances between Tx and Rx in this set is very straight forward because all of the points are in a row. Similar to the first floor, for each pair of Tx-Rx, we have done three sets of measurements. So, the total number of measurements in the second floor is

$$3\times\left(24+24+24+24\right)=288 \tag{4-2}$$

The third floor measurements took advantage of the existence of a metallic chamber. Figure 4.5 shows the floor plan and the measured points that have been done in the third floor of AK building. In this floor, the transmitter location is consistent during the measurements at A0, and four measurement sets have been done, namely A set, B set, C set and D set.

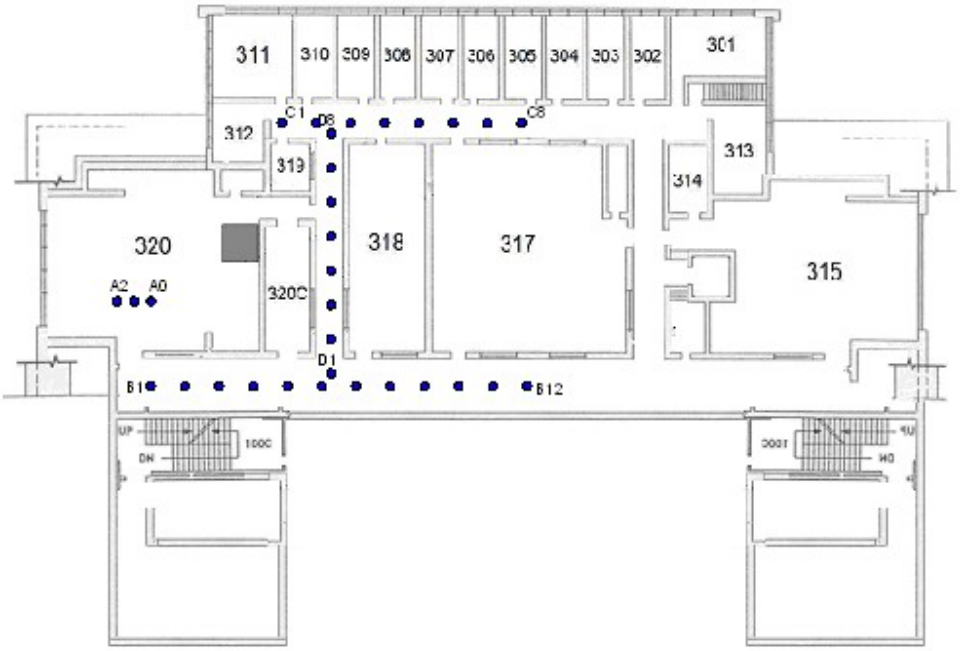

Figure 4.5: Measurement plan at 3rd Floor with Tx located at A0, B0, C0, and D0, AK Laboratories

The A set consists of only two measurement points and is meant for calibration of the measurement system. The B, C, and sets have 12, 8, and 8 measurement points respectively. These sets have been chosen in such a way to create a database in the case that the DP is not present. Table 4.4 shows the distances between Rx and Tx for these sets of measurements. The total number of measurements in the third floor is:

$$3\times\left(2+12+8+8\right)=90 \tag{4-3}$$

Table 4.4: Measured distances from Tx located at A0

A1	1	B1	4.29	C1	14.8	D1	11.99
A2	2	B2	4.73	C2	16.02	D2	11.59
		B3	5.87	C3	17.39	D3	11.52
		B4	7.38	C4	18.87	D4	11.80
		B5	9.08	C5	20.44	D5	12.40
		B6	10.88	C6	22.08	D6	13.27
		B7	12.74	C7	23.77	D7	14.37
		B8	14.64	C8	25.51	D8	15.65
		B9	16.57				
		B10	18.50				
		B11	20.45				
		B12	22.41				

The variety of measurements on the three floors of AK provides a rich and diversified database of scenarios that is significant for the modeling of both the path-loss and ranging errors. In total there were 513 points of measurements in phase I.

4.4 Phase II of UWB Measurements

The second phase of the measurements was made in three different types of buildings, a modern office building (Fuller Laboratories at WPI), a residential building (17 Schussler Rd.) and a manufacturing floor (Norton Company) all located in Worcester, Massachusetts. These measurements were divided into ITI, OTI, and RTI classes.

The measurement campaign involved improvements to the frequency range of measurement system (from 3-6GHz to 3-8GHz) which was done in parallel to obtaining necessary permissions and coordinating with the building's superintendents to perform the actual measurements. Each site was visited several times for negotiations and planning.

4.4.1 Description of the Buildings

This section provides an overview of the structure of the buildings used in the measurement campaign in the second phase of the measurements.

4.4.1.1 Fuller laboratories, WPI – A Typical Modern Office Building

Fuller Laboratories is a modern building that houses the Computer Science department at WPI and has been selected as the site for measurements related to office areas. Figure 4.6 shows photographs of the inside and outside of Fuller laboratories.

Figure 4.6: Office building environment at Fuller Laborataries, WPI

The dimensions of this building are on the order of a few tens of meters. It is surrounded on two sides by older WPI buildings (the Atwater Kent Laboratories and the Gordon Library) and by roads on the other two sides. One of the roads is an internal WPI campus road on the other side of which is the Salisbury Laboratories. The other road is a main road with an open park on the other side. The external walls of Fuller Laboratories are made of brick with some aluminum siding on two sides, metallic window frames and doors. Within the building are several computer labs, department offices, offices of faculty and graduate students, lecture halls, and classrooms. The walls are made of sheetrock and in some offices soft partitions divide the room into cubicles. Most of the rooms have furniture such as tables, chairs and desks as well as computers. Some conference rooms have glass walls mounted in metallic frames. Figure 4.7 shows the generic floor plans of Fuller Laboratories.

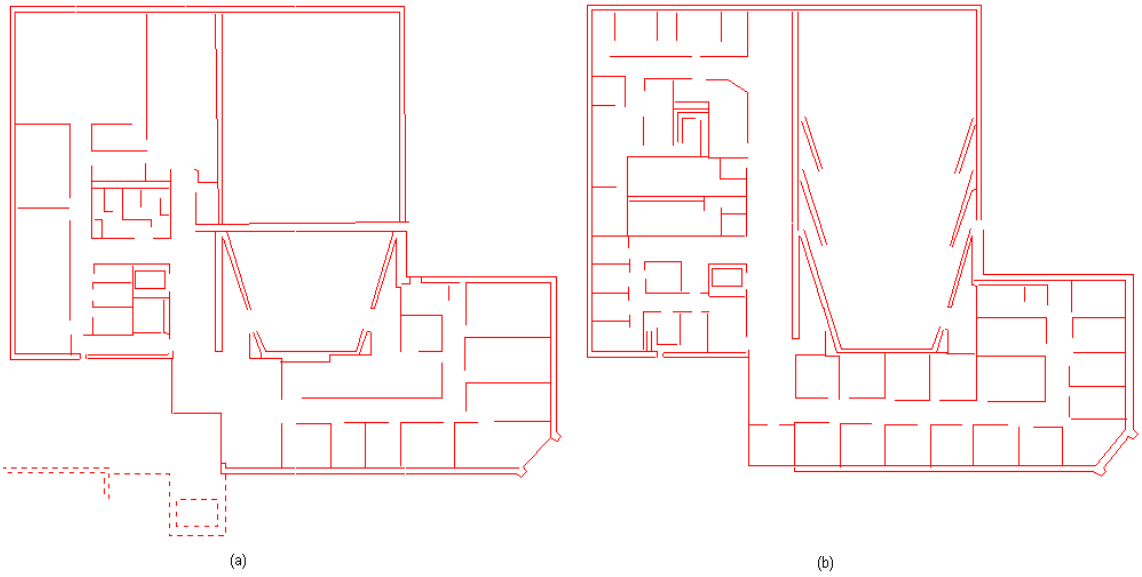

Figure 4.7: Floorplan of Fuller Laboratories, WPI, Worcester, MA.(a) First floor (b) Second Floor

4.4.1.2 Schussler Road, WPI – A Typical Residential House

This is a residential house available at WPI for graduate students. It is a fairly big house with wooden exterior walls and sheetrock interior walls. The house is however very old and is located in a fairly open area with a few buildings of similar features located nearby. Some trees and a parking lot surround other sides of the house. Inside the house there are several rooms that are furnished with couches, tables, chairs, etc. Some rooms have brick fireplaces. Rooms have dimensions on the order of a few meters. Figure 4.8 shows photographs of the inside and outside of Schussler house.

Figure 4.8: Residential house environment at 17 Schussler Rd., WPI

Figure 4.9 shows the floor plan of Schussler house.

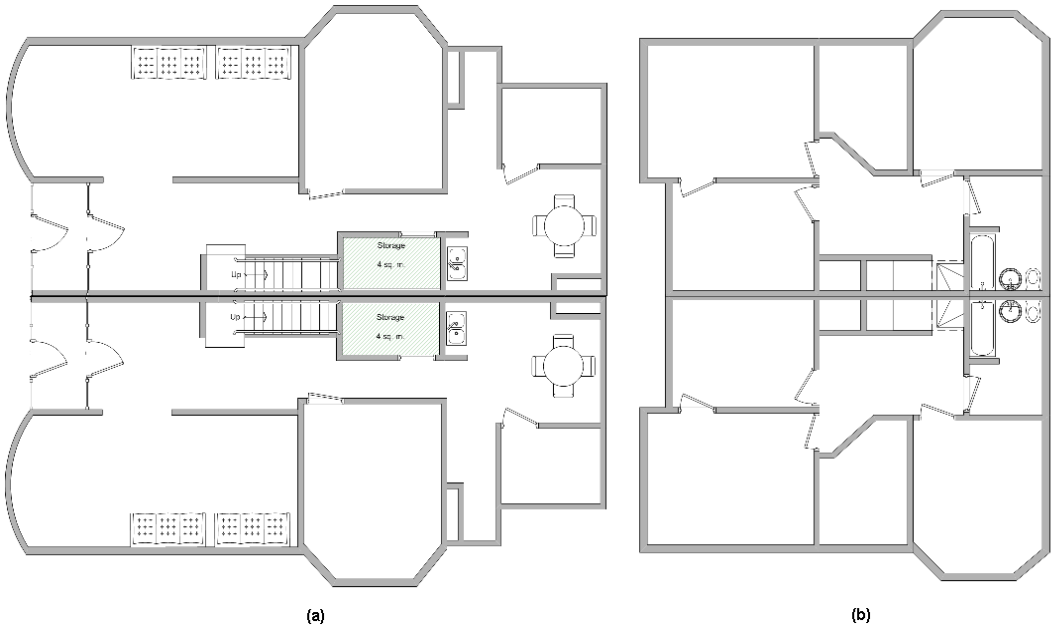

Figure 4.9: Floorplan of 15 and 17 Schussler Rd., Worcester, MA.(a) First floor (b) Second Floor

4.4.1.3 Norton Co., Worcester, MA – A Typical Manufacturing Floor

Norton Company is a manufacturer of welding equipment and abrasives for grinding machines. The building selected for measurement is Plant 7 that is a large building with dimensions on the order of a few hundred meters. This building is

connected to a five floor brick building and to another manufacturing floor through a long corridor. The rest of Plant 7 is mainly surrounded by open areas and small buildings. The building is used for manufacturing abrasives and houses huge ovens, grinding machines, transformers, cranes and other heavy machinery. Figure 4.10 shows snap shots of the interior and exterior of this building.

Figure 4.10: Manufacturing building environment at Norton Compnay, Worcester, MA

The building includes a set of partitioned offices with brick external walls, metallic windows and doors attached to the main huge open manufacturing area with steel sheet walls of a height of around seven meters and small metallic windows close to the ceiling. In addition to the fluorescent lights, many utility pipes and metallic support beams hang from the ceiling.

4.4.2 Details of measurement campaign

This section provides the details of the measurement campaign to collect a database of measurements in four different buildings. The Atwater Kent Laboratory was examined in the first phase of this project and in this campaign it was used for roof-to-indoor measurements.

4.4.2.1 Fuller Laboratories – Modern Office

Table 4.5 summarizes the Fuller measurement campaign. For each location there were three measurements and for each of those there were two different polarizations of the receiver antenna. One is horizontal or parallel and the other is vertical or perpendicular.

Table 4.5: Fuller Laboratories Measurement database

Environment	Scenario	Transmitter Location	# of Locations	Meas./ Location	# of Positions	Number of Measurements
Office (Fuller Laboratories)	Outdoor/Indoor	entrance I	31	3	2	186
		entrance II	25	3	2	150
		arbitrary	25	3	2	150
	Indoor/indoor	LOS	20	3	2	120
		OLOS	21	3	2	126
Total number of Measurements						732

The main objective of this part of the measurement campaign is to examine the behavior of the DP when the transmitter is in different locations around and inside an office environment. The receiver points were placed on three different floors: basement, first and second floor. More details about the description of the measurement can be found in [IWT05].

4.4.2.2 17 Schussler Road – Residential House

Table 4.6 summarizes the 17 Schussler Road measurement campaign. For each location there were three measurements and for each of those there were two different polarizations of the receiver antenna. One is horizontal and the other is vertical.

Table 4.6: 17 Schussler measurement database

Environment	Scenario	Transmitter Location	# of Locations	Meas./ Location	# of Positions	Number of Measurements
Residential (17 Schussler Rd.)	Outdoor/Indoor	area I Tx1 (0, -4)	31	3	2	186
		area II Tx2 (4, 11)	31	3	2	186
	Indoor/Indoor	OLOS Tx3 (3, 6)	29	3	2	174
Total number of Measurements						546

This measurement campaign focused on the channel behavior and the first path in a residential environment. The campaign included a mix of indoor-to-indoor, outdoor-to-indoor, and inter-floor measurements. Figures 4.11 and 4.12 show the floor plans of the first and second floors of 17 Schussler with the transmitter and receiver points clearly labeled. The measurements for all the receiver points on the first and the second floors were repeated for the three different transmitter locations, namely outdoor-to-indoor (Tx1 & Tx2) indoor-to-indoor (Tx3). A total of 6 snapshots per location were obtained (3 per location and 2 polarizations per location).

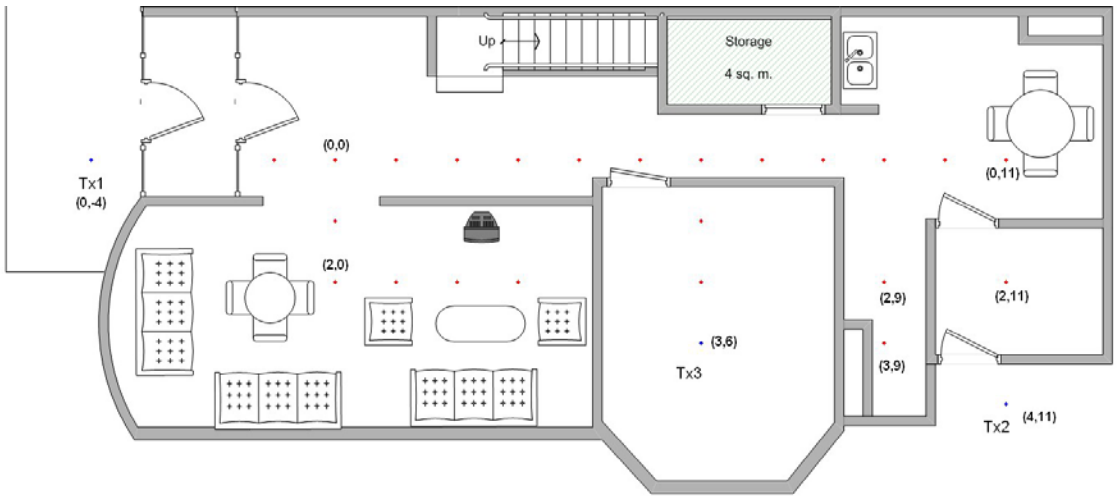

Figure 4.11: Measurement layout on first floor of 17 Schussler Road

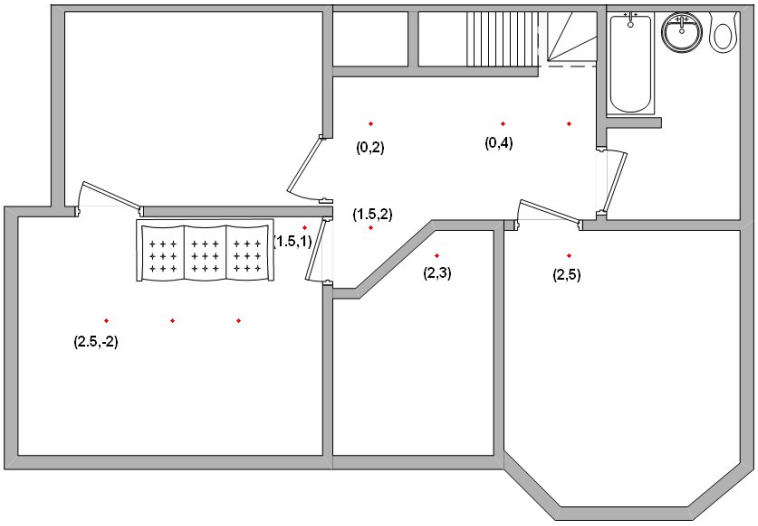

Figure 4.12: Measurement layout on second floor of 17 Schussler Road

4.4.2.3 Norton Company– Manufacturing Floor

Table 4.7 summarizes the measurement campaign at the Norton Company. For each location there were three measurements and for each of those there were two different polarizations of the receiver antenna. One is horizontal and the other is vertical. The measurements are divided into two indoor-to-indoor, two outdoor-to-indoor, and one roof-to-indoor measurement sets. More details about the description of the measurement can be found in [IWT-05].

Table 4.7: Norton Company Measurement databse

Environment	Scenario	Transmitter Location	# of Locations	Meas./ Location	# of Positions	Number of Measurements
Manufacturing Floor (Norton Company)	Outdoor/Indoor	entrance	20	3	2	120
		arbitrary	21	3	2	126
		Roof	21	3	2	126
	Indoor/Indoor	LOS I	20	3	2	120
		LOS II	21	3	2	126
Total number of Measurements						618

4.4.2.4 Atwater Kent – Old Office

The objective of the measurement campaign in Atwater Kent Laboratory was to examine the behavior of the DP for roof-to-indoor propagation conditions to complement the measurements collected in Phase I of the project. To perform these measurements the transmitter was located on the roof and the receiver points were placed on the third floor of AK in a variety of locations forming different propagation scenarios. The height of the roof above the third floor and consequently the vertical distance between the transmitter and the receiver is 3 meters. Figure 4.13 shows the floor plan of AK with the locations of the receiver on the third floor and the image of the location of the transmitter on the roof over the third floor.

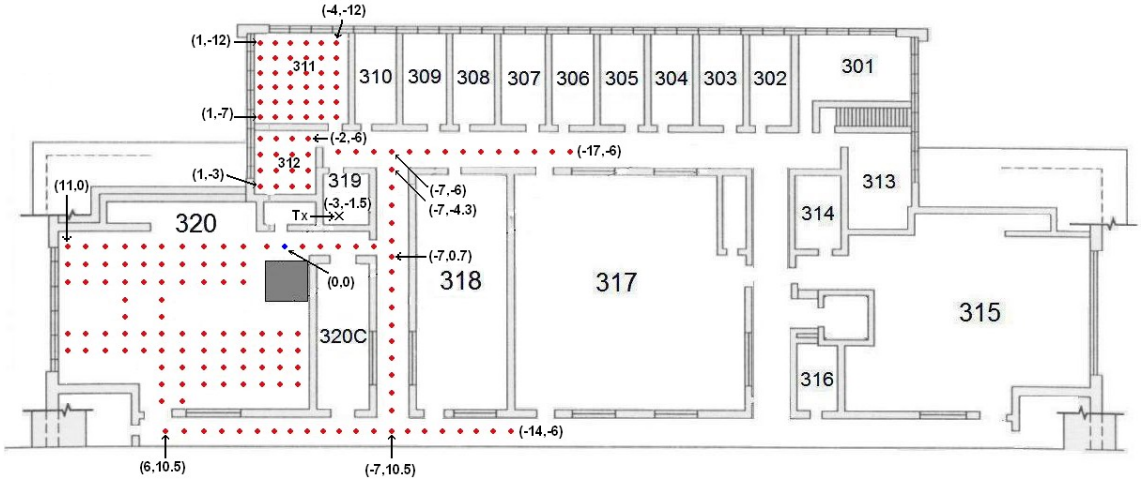

Figure 4.13: Measurement layout on 3rd floor of Atwater Kent building

The measurements were partitioned in several different rooms and corridors to reflect the diversity of the propagation scenarios. The layout was devised to facilitate identification of the receiver locations and calculation of the exact distance between the transmitter and the receiver. This was carried out using Cartesian coordinates. The (0, 0)

point was selected in accordance to the floor plan. Then the receiver points were placed one meter apart where it was accessible to conduct a measurement. Table 4.8 shows the breakdown of the measurements for the roof-to-indoor setup. In each location 6 measurements were collected corresponding to two positions, namely, horizontal and vertical polarization and 3 measurements per location. A total of 1038 snapshots were collected for this scenario.

Table 4.8: AK Roof –indoor measurement database

Environment	Scenario	Transmitter Location	Receiver Locations	# of Locations	Meas./ Location	# of Positions	Number of Measurements
Office (Atwater Kent)	Outdoor/Indoor (Roof)	Roof (-3, -1.5, 3)	AK3C1	21	3	2	126
			AK3C2	15	3	2	90
			AK3C3	15	3	2	90
			AK311	20	3	2	120
			AK312	14	3	2	84
			AK320 (CWINS)	88	3	2	528
Total # of Measurements							1038

4.4.3 An innovative method for massive geolocation measurements

One of the hidden challenges of the measurements that until you carry it out it does not reveal itself is how to measure the distance between the transmitter and the receiver in certain conditions. In the phase II of the measurements we had to perform outdoor-to-indoor, roof-to-indoor, and inter-floor indoor-to-indoor measurements. In all of these cases there was no direct path between the transmitter and the receiver without any obstacle to measure the distance between them.

In order to solve this problem we devised a new technique to locate the receiver points in the building and transmitter points inside and outside of the building. We created a 3 dimensional Cartesian coordinate system with 1 meter as its unit. Then we places grid points on the floor in the positions that we were interested to measure, and assigned their coordinate location to each point. For example if the coordinate of the transmitter is (0,0,0) and it is located in the first floor, then a receiver in the first floor can have coordinate of (2,3,0) or (x,y,0), when we want to measure in the second floor the receiver coordinate will be (x,y,3) provided that the height of the second floor is three meters.

Then the distance between the transmitter and the receiver can be easily found using the Euclidian relation.

$$d_{AB} = \sqrt{(x_A - x_B)^2 + (y_A - y_B)^2 + (z_A - z_B)^2} \tag{4-4}$$

4.5 Summary

In this chapter briefly we described our measurement system and database. The measurement system is a frequency domain measurement system with a vector network analyzer as the major part of that. We have done two phases of the measurement with 3 GHz bandwidth in phase I and 5 GHz bandwidth in phase II.

Phase I of the measurements were done in Atwater Kent Laboratories in Worcester Polytechnic Institute, for OTI and ITI cases. Overall 513 points were measured in the phase I, 135 points in the first floor, 188 points in the second floor, and 90 points in the third floor.

Phase II of the measurements has been done in four different buildings, representing four different types of environments, Schussler house, Fuller Laboratories, Norton Company, and Atwater Kent Laboratories, representing residential, modern office, manufacturing, and old office environments respectively.

The processed data is divided into:

a) Indoor-to-indoor (***ITI***)

b) Outdoor-to-indoor (***OTI***)

c) Roof-to-indoor (***RTI***)

In the indoor-to-indoor measurements we divide the measurement into LOS and OLOS areas. Table 4.9 shows the overall picture of the measurement database in the four buildings. In the outdoor-to-indoor scenarios for the office and manufacturing floor, we differentiate the location of outside reference point as being close to the entrance of the building or being located in an arbitrary position not correlated to the location of entrance.

Table 4.9: Summary of the Measurement Database

Environment	Measurement type	TX or (RX) Location	# of Locations	Meas./ Location	# of Positions	Number of Measurements
Office (Fuller Laboratories)	OTI	Entrance I	31	3	2	186
		Entrance II	25	3	2	150
		Arbitrary point	25	3	2	150
	ITI	LOS	20	3	2	120
		OLOS	21	3	2	126
Residential (17 Schussler Rd.)	OTI	Area I	31	3	2	186
		Area II	31	3	2	186
	ITI	OLOS	29	3	2	174
Manufacturing Floor (Norton Company)	OTI	Entrance	20	3	2	120
		Arbitrary	21	3	2	126
	ITI	LOS I	20	3	2	120
		LOS II	21	3	2	126
	RTI	(same as arbitrary)	21	3	2	126
Atwater Kent Laboratory	RTI	(AK3C)	51	3	2	306
		(AK311)	20	3	2	120
		(AK312)	14	3	2	84
		(AK320/CWINS)	88	3	2	528
Total number of Measurements						2934

Chapter 5

Preliminary Analysis of UWB Measurements

5.1 Introduction

In this chapter, based on our UWB measurements in chapter 4, we have developed path-loss models for DP and total power. The innovative path-loss models are created for geolocation applications, which consider both the power of the first path and total power. The power of the first path is essential for geolocation applications and the total power is essential for communication coverage. Also we have introduced DME models based on the received power. In section 2, we introduce our path-loss models for each environment and in the next section we introduce our DME models for each situation.

5.2 Path-Loss Models

In this section we first introduce the general path-loss model (PLM), and then we give the PLM for each building separately.

5.2.1 The General Path-Loss Model

A typical path-loss model usually has the following format [Pah05]:

$$L_x = L_0 + 10\alpha_x \log_{10}(d) + \eta_x \tag{5-1}$$

where L_x represents the path-loss in dB format, L_0 is the path-loss in first meter, d is the distance, α is called the distance power gradient. Random variable η_x is a zero mean Gaussian random variable representing the traditional shadow fading component of the path-loss model. In the channel measurements that we have done in phase II of the measurement campaign, we have introduced a new term by changing the polarization of the receiver antenna. Also the measurements showed that the roof should also be considered separately. Therefore the path-loss model is given by,

$$L_x = L_0 + L_R + f(d) + \eta_x + \mu_x \tag{5-2}$$

The parameter L_R is the additional path-loss component due to the roof effects. The random variable μ_x is a new non-zero mean Gaussian random variable representing the effects of polarization caused by laying the antenna on the floor. In practice this random variable is added when we consider the user lying on the ground causing a 90 degree difference in the polarization of the antennas. The function *f(d)* is a more

general form of the log function in (5-1). It is the best fit one-piece or two-piece distance-power relationship line, either in the form of:

$$f(d) = 10\alpha \log_{10} d \tag{5-3}$$

with no break, or in the form of

$$f(d) = \begin{cases} 10\alpha_1 \log_{10} d; & d \le D \\ 10\alpha_1 \log_{10} D + 10\alpha_2 \log_{10} (d / D); & d > D \end{cases} \tag{5-4}$$

with one break at *D*. In all models the subscript *x* is either, representing total power, or *F*, representing the first path power. In all our models in the first and the second phase of this project, the path-loss in the first meter is $L_0 = 42dB$ that associates with the center frequency of our measurements in *3-6GHz*.

Providing a path-loss model for the first path is not done in the literature before and is something unique about this measurement campaign. The unique models presented in this section provide for calculation of the coverage of the RF signal as well as coverage of the first path, which shows the boundaries for precision location estimation, in variety of buildings for a person standing up or laying on the floor.

5.2.2 Path-Loss models in each building

For path-loss modeling we have defined 21 different radio propagation scenarios for each building and we have developed path loss models for the total power and the first path power for 3GHz and 500MHz bandwidths for each of these propagation scenarios to produce a table of 72 models for different areas. Table 5.1 shows the

summary of the 21 scenarios for path-loss modeling of the total and the first path powers.

Table 5.1: Summary of the Path-loss Models Scenarios

Environment	Type of Measurement	Location of TX	Description of the Scenarios for RX Locations
Office (Fuller Laboratory)	OTI	Entrance I	Multi-floor
		Entrance II	Multi-floor
		Arbitrary point	Multi-floor
	ITI	LOS	Open area around entrance at the first floor
		OLOS	Same floor with elevator
			Inter-floor – open area
			Inter-floor – not open
Residential (17 Schussler Rd.)	OTI	Area I	Multi-floor (wooden construction)
		Area II	Multi-floor (brick construction)
	ITI	OLOS	Same-floor
			Inter-floor
Manufacturing Floor (Norton Company)	OTI	Entrance	Single-floor (behind entrance door)
		Arbitrary	Single-floor (a large walkway inside the building)
	ITI	LOS I	Open area with machinery
		LOS II	Straight walkway
	RTI	Roof	Large walkway inside (window on the roof)
			Large walkway inside (no window)
Atwater Kent Laboratory	RTI	Roof	Corridors of the third floor of AKL
		Roof	Inside room AK311
		Roof	Inside room AK312
		Roof	Inside room AK320 – the CWINS laboratory

In this section only one scenario is shown on the next page as a sample of the PLM's. A complete list of the PLM's can be found in Appendix A.

5.2.2.1 Fuller PLM for OTI: Inter-Floor - Arbitrary Point

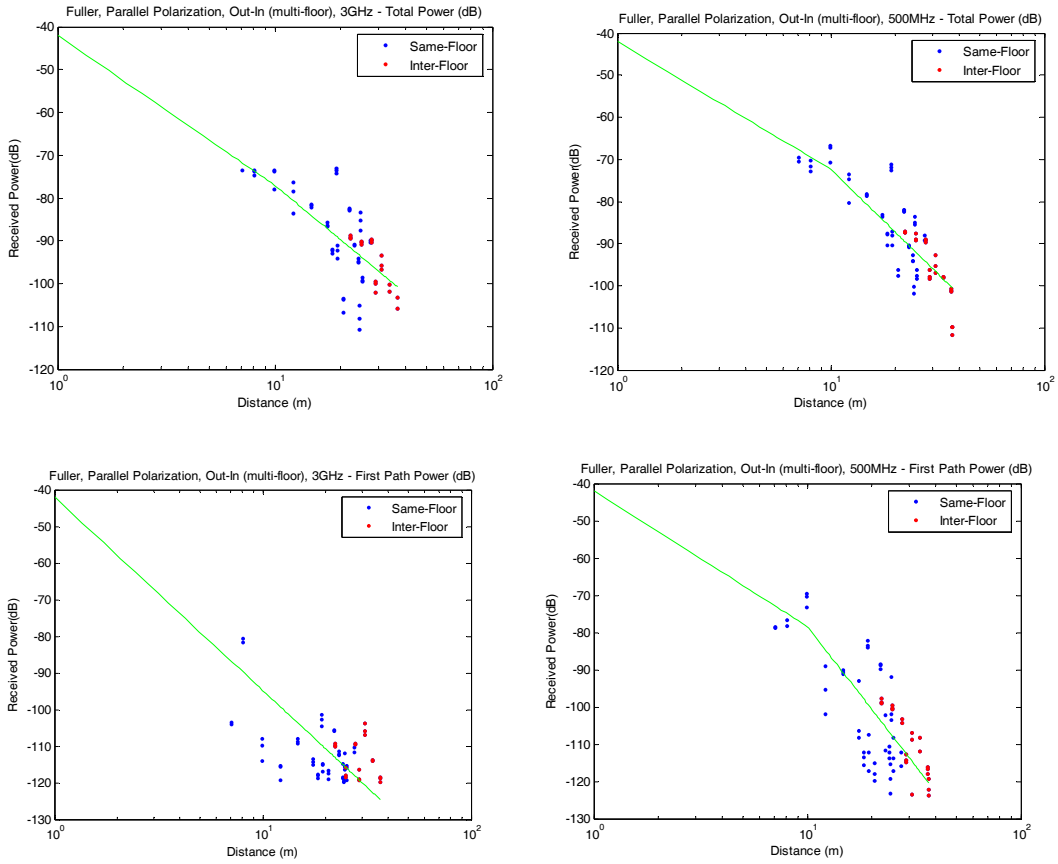

Figure 5.1: PLM for Fuller, OTI –Inter-floor, Arbitrary Point

@ 3GHz

$$L_T = \begin{cases} 42 + 35\log_{10} d + \eta_T + \mu_T & d \le 10 \\ 77 + 42\log_{10}\left(d/10\right) + \eta_T + \mu_T; d > 10 \end{cases}$$

$$\sigma_{\eta_T} = 5.1;\ m_{\mu_F} = 7.1, \sigma_{\mu_F} = 4.1$$

$$L_F = 42 + 53\log_{10} d + \eta_F + \mu_F$$

$$\sigma_{\eta_F} = 8.6;\ m_{\mu_F} = 4.3, \sigma_{\mu_F} = 7.9$$

@ 500MHz

$$L_T = \begin{cases} 42 + 30\log_{10} d + \eta_T + \mu_T & d \le 10 \\ 72 + 49\log_{10}\left(d/10\right) + \eta_T + \mu_T; d > 10 \end{cases}$$

$$\sigma_{\eta_{T1}} = 4.7;\ m_{\mu_T} = 4.6, \sigma_{\mu_T} = 3.4$$

$$L_F = \begin{cases} 42 + 36\log_{10} d + \eta_F + \mu_F & d \le 10 \\ 78 + 58\log_{10}\left(d/10\right) + \eta_F + \mu_F; d > 10 \end{cases}$$

$$\sigma_{\eta_F} = 8.6;\ m_{\mu_F} = 5.1, \sigma_{\mu_F} = 7.7$$

5.3 Power based DME models

5.3.1 General Power Based DME Model

In DME modeling, the propagation environment is very important in determining the overall performance. A novel DME model first introduced in [IWT04] places a greater emphasis on the behavior of the DP power. When the sensor node is close to the reference point, the power of the DP is very strong. As a result, the first path can be easily detected which means a very accurate TOA estimation, which translates to very accurate ranging. This region of operation is usually referred to as Detected Direct Path (DDP). However as the node moves away from the reference point the strength of the DP decays gradually, where it reaches a region where the DP is no longer as strong. In fact it is weakened and in certain instances it would be Undetected Direct Path (UDP). Figure 5.2 further explains the three region DME model.

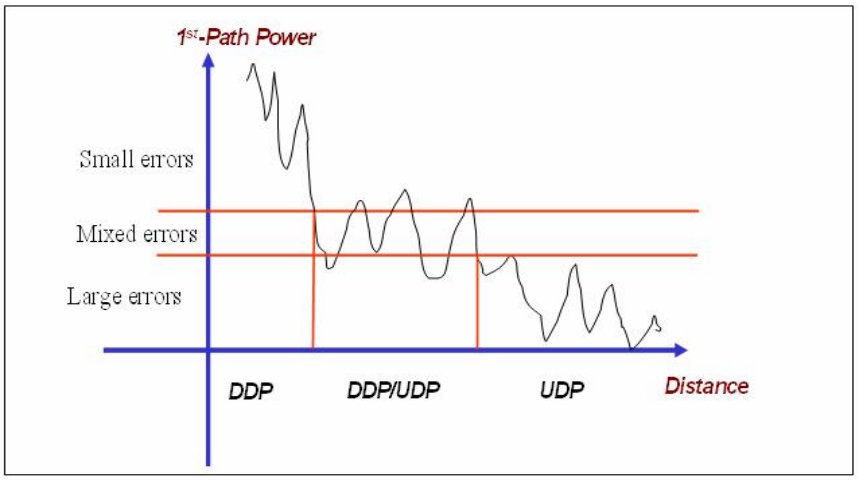

Figure 5.2: Illustration of the relationship among first-path power, distance and DME

In the second region, a mixture of DDP and UDP conditions provide acceptable ranging but occasionally large errors. Finally when the DP can no longer be detected the

third region of operation is known as UDP; where it suffers the most errors. As such it exhibits the worse ranging accuracy. Note that in all the previous mentioned regions, the total power is usually much higher than the DP power. When the sensor node's total received power falls below a certain threshold, then it is operating in the No Coverage (NC) area; where neither positioning nor communication can take place. In each performance region the error is characterized with a Gaussian random variable but with different mean and variance. Specifically the variance would provide a statistical measure of the behavior of the error in each region.

In the next section we provide DME models for different scenarios, described before.

5.3.2 DME Models for Different Scenarios

This section provides the details of DME models for all four buildings studied in phase II of the project. For the purpose of DME modeling, measurements in each building are divided into ITI and OTI. The ITI measurements are used to design an LOS and an OLOS models. The OTI measurements are used to design two models for the measurements obtained when the transmitter is located on the ground and when it is on the roof. Therefore for a given bandwidth in each building we have a maximum of four models.

1- Indoor-to-indoor
    a. LOS
    b. OLOS
2- Outdoor-to-indoor
    a. Ground mounted
    b. Roof mounted

For each bandwidth we have three models for the Fuller Laboratories, three models for 17 Schussler Road, three models for Norton Company, and one model for the Atwater Kent Laboratories. This way we have developed 20 models for the four buildings, 10 for the bandwidth of 3GHz and 10 for 500MHz bandwidth. For each model according to appearance of the DME scattered plots against the power of the first path we have defined one, two or three regions for the statistical behavior of the DME. The scattered plots, threshold between the areas, and the mean and the standard deviation of the DME for each scenario are presented in the following 10 subsections. Each scenario is presented with two scatter plots on top of the page followed by a two-column table providing the statistical characteristics of the data in each region. The top row of the table provide the bandwidth (either 3GHz or 500MHz) followed by up to two numbers in parenthesis providing the first path power thresholds separating different areas of the model. In the areas in which we can not classify the DME into different partitions we have no threshold available. In the following rows of the table we provide the mean and standard deviation of the errors in different areas. Again, if there are less than three areas for the model we indicate that in that the mean and standard deviation is not available in that region. Similar to PLM's in this section only one scenario is shown on as a sample of DME models. A complete list of the PLM's can be found in Appendix B.

5.3.2.1 Fuller DME for OTI: Ground Mounted Transmitter

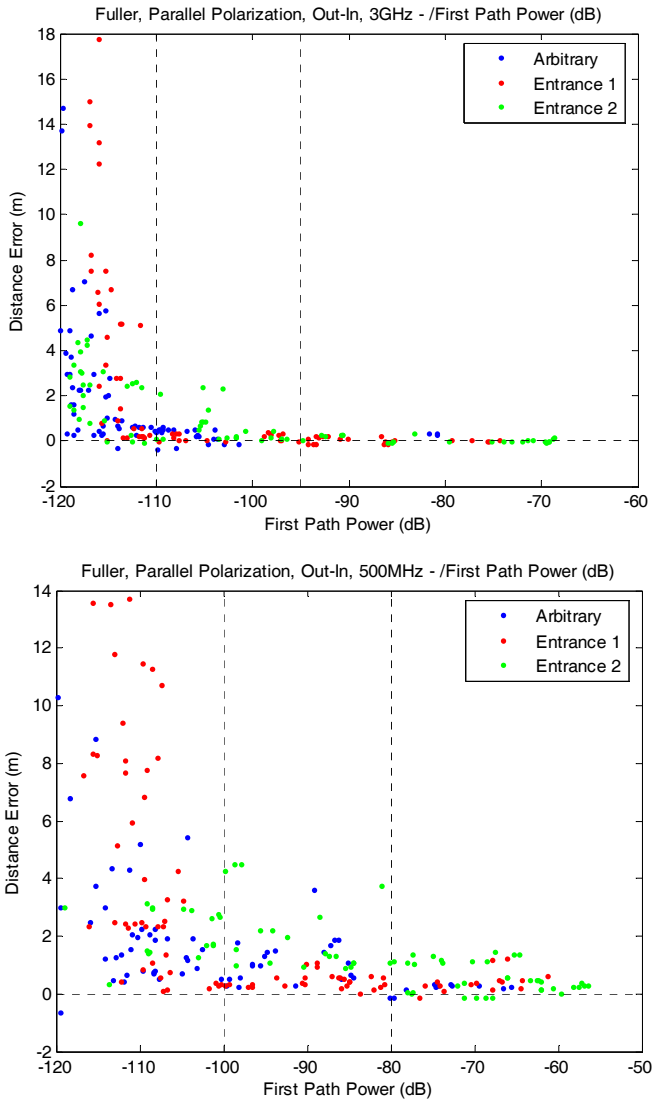

Figure 5.3: DME for Fuller, OTI – Ground Mounted Transmitter

@ 3GHz	Thresholds (-95, -110)	@ 500MHz	Thresholds (-80, -100)
Mean 1 = 0	Std. 1 = 0.1	Mean 1 = 0.3	Std. 1 = 0.3
Mean 2 = 0.2	Std. 2 = 0.2	Mean 2 = 0.7	Std. 2 = 0.6
Mean 3 = 3.4	Std. 3 = 4.1	Mean 3 = 3.6	Std. 3 = 3.6

5.4 Summary

In this chapter we analyzed the measurements described in chapter 4 in order to be useful for our distance measurement error modeling. First we introduced a general path-loss model that covers different conditions of our measurements (e.g. polarization, and roof measurements). Then we provided PLMs for each scenario in each building for two different bandwidths, 500MHz and 3GHz. Finally we introduced the power based DME model for the same two bandwidths. This model is based on the received power of the first path; they provide means and standard deviations of Gaussian distribution functions to simulate the error. The DME models we presented for each building. However, the observations state that the type of the building is effective on the PLMs but then the power based distance models are not affected as much by that. As a result we provided a combined model for DME as shown in Table 5.2, which summarizes the thresholds and statistics of the three different scenarios (ITI, OTI, and RTI) over the entire database.

Table 5.2: Summary of the DME models

		500 MHz		3 GHz	
ITI	*Threshold (dB)*	(-60, -80)		(-80, -100)	
		Mean (m)	***STD (m)***	***Mean (m)***	***STD (m)***
	Region 1	0	0.2	0	0.2
	Region 2	0.4	0.9	0.2	0.9
	Region 3	2.2	2.6	3.5	3
OTI	*Threshold (dB)*	(-80, -100)		(-90, -110)	
		Mean (m)	***STD (m)***	***Mean (m)***	***STD (m)***
	Region 1	0.4	0.5	0.1	0.2
	Region 2	0.7	0.5	0.3	0.3
	Region 3	2.6	3.2	2.7	3.5
RTI	*Threshold (dB)*	(-80, -100)		(-80, -100)	
		Mean (m)	***STD (m)***	***Mean (m)***	***STD (m)***
	Region 1	0	0.1	0	0.1
	Region 2	0.5	0.9	0.5	0.9
	Region 3	2.3	3.1	2.5	3.5

Chapter 6

Modeling of Distance Measurement Error using UWB data

6.1 Introduction

In this chapter we use the results of the measurements that we described in chapter 5 to develop an enhanced model. This model addresses the deficiencies that the previous model, introduced in chapter 2 has. The previous model is based on RT rather than actual measurements; also the modeling is not based on physical causes and instead is based on mathematical curve fitting. In this chapter first we study different components in DME and then based on the results of this study we model each of those

components separately. At the end we study the effect of bandwidth on the DME and conclude the chapter.

6.2 Components of DME

Assuming the actual distance between the Tx and the Rx is *d*; the estimated distance in a TOA positioning system is given by (1-2). The actual distance *d* is measured through physical measurement between Tx and Rx, and $\hat{d}$ is obtained by detecting TOA of the first peak above the detection threshold. Based on the above assumptions we define the distance measurement (estimation) $\varepsilon_W(d)$ error as

$$\varepsilon_W(d) = \hat{d}_W - d \tag{6-1}$$

the subscript *W* refers to the system bandwidth and this is the only addition to the basic definition of DME given in (1-3).

In modeling the distance measurement error we differentiate the small errors caused by multipath from the large errors produced by the occurrence of UDP conditions. We refer to the small distance errors caused by multipath as the multipath distance measurement error, $\varepsilon_{M,W}(d)$, and to the large errors caused by the UDP condition as UDP distance measurement error, $\varepsilon_{U,W}(d)$. The multipath error caused by neighboring paths always exists and the UDP error exists only when the UDP condition occurs. Figure 6.1 shows a channel profile with bandwidth of 1GHz when the DP is detectable, which is the DDP case.

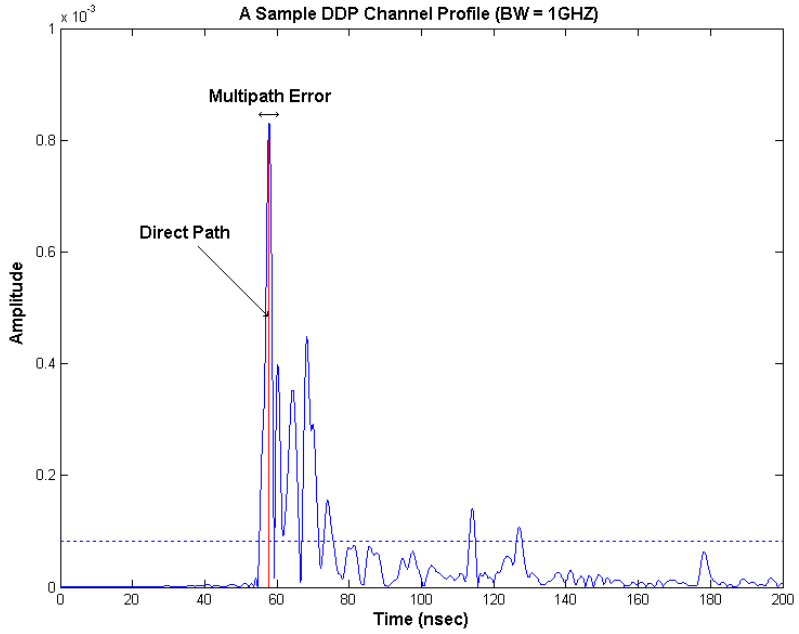

Figure 6.1: A sample DDP channel profile derived from UWB measurements with 1GHz bandwidth

Figure 6.2 shows a UDP channel profile with the same bandwidth, where the DP is not detectable. Since the power of the DP is less than the detection threshold, we have a clear UDP situation, in which the first path is detected and declared as the DP, resulting in a 5.23m distance measurement error.

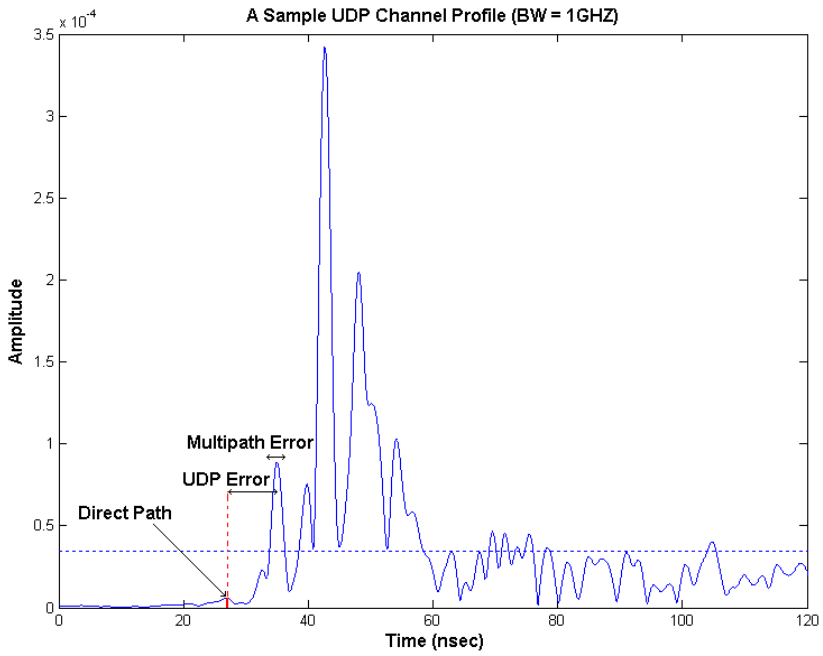

Figure 6.2: A sample UDP channel profile derived from UWB measurements with 1GHz bandwidth

We model the occurrence of the UDP condition with the random variable $\xi_W(d)$ that takes value of "1" when a UDP condition occurs and "0" otherwise.

It must be mentioned that there is also another type of error involved in this process caused by physical measurement of d, ε_P, adding to total error.

$$\varepsilon_W(d) = \varepsilon_P + \varepsilon_{M,W}(d) + \xi_W(W)\varepsilon_{U,W}(d) \tag{6-2}$$

This error comes from the inaccuracies occurring during measurement of the actual distance between the transmitter and the receiver. We have assumed that this error is a zero mean Gaussian with a variance that depends on the accuracy of the measurement error. Similar to $\varepsilon_{M,W}(d)$, this type of error always exits. Therefore it

can not be separated from $\varepsilon_{M,W}(d)$. Therefore, we don't consider this error as a separate error and assume that it is integrated in $\varepsilon_{M,W}(d)$.

$$\varepsilon_P + \varepsilon_{M,W}(d) \approx \varepsilon_{M,W}(d) \tag{6-3}$$

Therefore, our final model for $\varepsilon_W(d)$ is given by,

$$\varepsilon_W(d) = \varepsilon_{M,W}(d) + \xi_W(W)\varepsilon_{U,W}(d) \tag{6-4}$$

To determine the model parameters from the empirical data we have partitioned our database of the distance measurement errors for a given bandwidth into DDP and UDP database. The DDP distance measurement error database represents cases that are disturbed only by multipath distance measurement errors. On the other hand the UDP database represents the cases which are disturbed by both multipath and UDP DME.

In the next two sections we use the empirical data to develop a statistical model for all components of (6-4) as a function of system bandwidth and the distance between Tx and Rx.

6.3 Modeling of the Multipath-DME

In this section since we are interested in modeling the multipath-DME (MDME) we use only DDP database. Figure 6.3 shows the scatter plots of $\varepsilon_{M,W}(d)$ versus distance, *d*, for DDP channel profiles and two different bandwidths 100 MHz and 500 MHz. Naturally one expects the distance measurement error to increase with the increase of distance between the transmitter and the receiver.

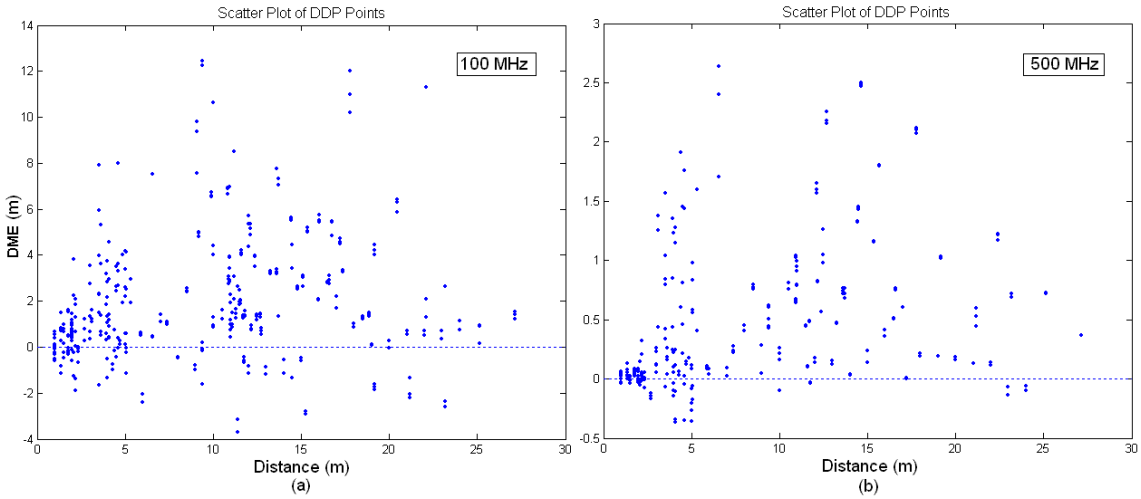

Figure 6.3: Scatter Plots of DME for DDP, (a) 100 MHz, (b) 500 MHz.

Our observation from the empirical measurement results showed that this increase has a nonlinear relationship. Therefore, to proceed with our modeling of MDME, in a manner similar to chapter 2, we introduce parameter γ_W, the normalized distance error, given by,

$$\gamma_W = \frac{\varepsilon_{M,W}(d)}{\log(1+d)} \tag{6-1}$$

The logarithm in the denominator is used to accommodate the increase pace of error below linear. The scatter plots of γ_w are shown in Fig. 6.4. It can be seen that the normalization factor has compensated the distance effect.

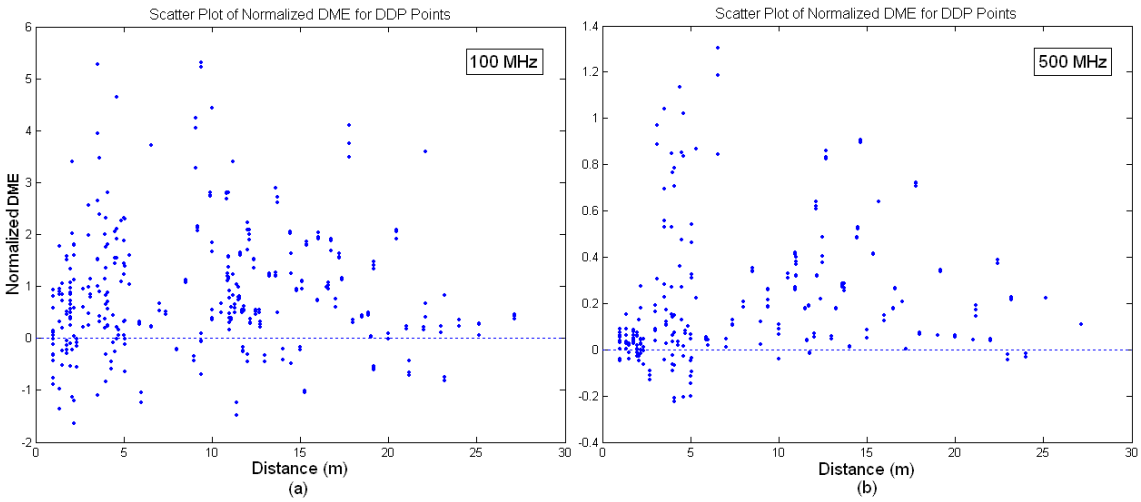

Figure 6.4: Scatter plots of normalized DME for DDP points, (a) BW = 100 MHz, (b) BW = 500 MHz.

Figure 6.5 shows the probability density function (PDF) of the $\varepsilon_{M,W}(d)$. We observe that by increasing the system bandwidth the variance of the error decreases. Also we can see that the PDF is not exactly symmetric, which is a consequence of having all arriving neighbor multi-paths on the right side of the DP.

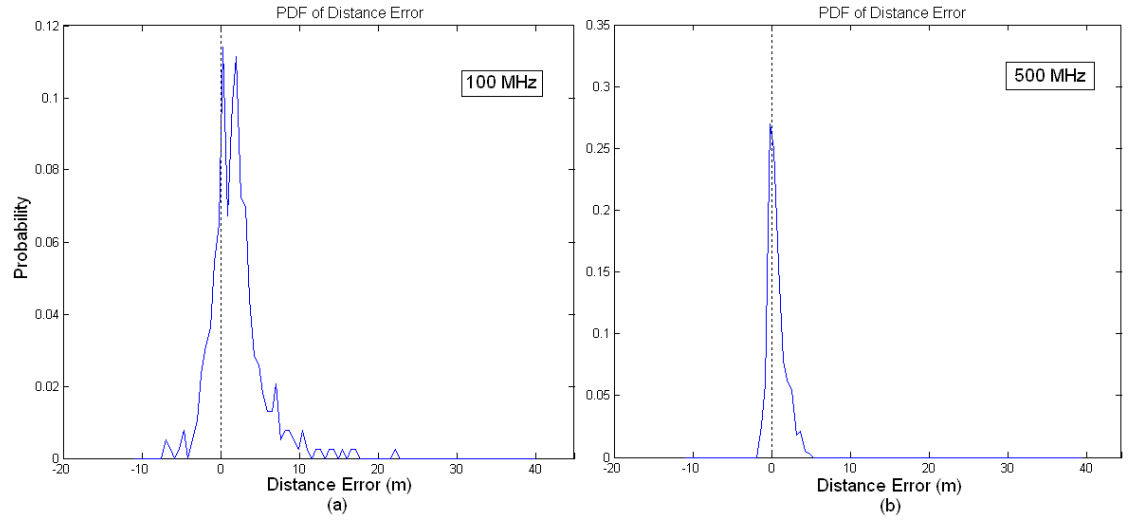

Figure 6.5: PDF's of DME for DDP, (a) 100 MHz, (b) 500 MHz

Our measurement results show that this normalization causes the resulting normalized error to form a Gaussian distribution. Therefore, the multipath error has been modeled as,

$$\begin{aligned} \varepsilon_{M,W} &= \gamma_W \log(1+d) \\ &= G\left(m_{M,W}, \sigma_{M,W}\right)\log(1+d) \end{aligned} \tag{6-2}$$

Where,

$$f_{\gamma_W}(x) = \frac{1}{\sigma_{M,W}\sqrt{2}} e^{-\frac{\left(x-m_{M,W}\right)^2}{2\sigma_{m,W}^2}} \tag{6-3}$$

and $G\left(m_{M,W}, \sigma_{M,W}\right)$ is a Gaussian random variable with mean $m_{M,W}$ and variance $\sigma_{M,W}^2$.

Table 6.1 displays typical values of these parameters. It should be noted that due to its nature, $\varepsilon_{M,W}(d)$ can be positive or negative, in fact scatter plots of the simulation in Figs 2.7 and 2.8, or measurements such as Fig. 5.17 support this fact that DME can be a negative value. Therefore, since a Gaussian number with a mean close to zero has negative values, it is capable of modeling this parameter. Figure 6.6 shows the CCDF comparison between the measurement results and the model, for the DDP points.

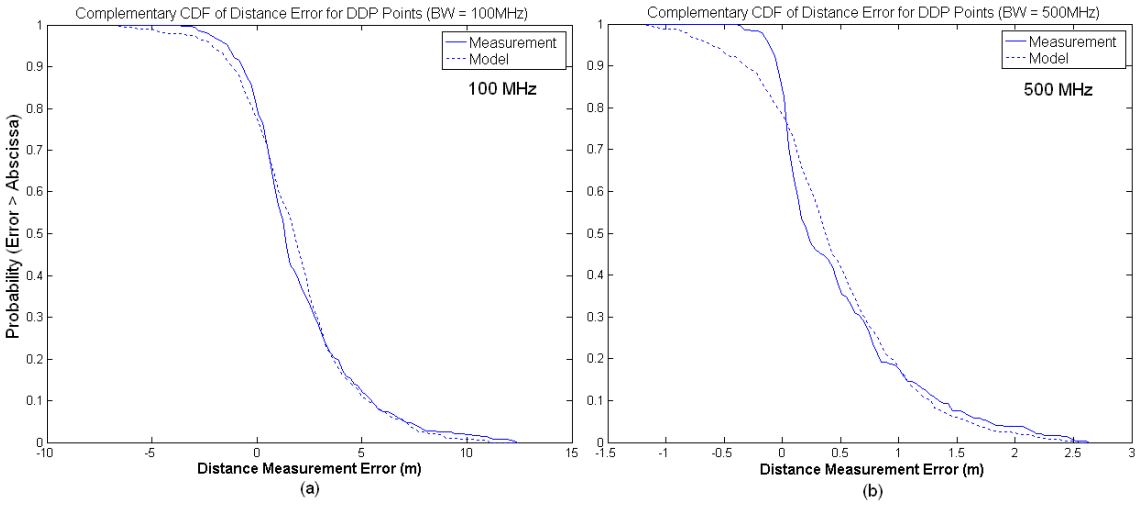

Figure 6.6: CCDF comparisons between measurements and model for DDP points, (a) BW = 100 MHz, (b) BW = 500 MHz.

6.4 Modeling of the UDP-DME

In order to model the UDP distance measurement errors we need to model two parameters, $\xi_W(d)$ and UDP-DME (UDME). The random variable $\xi_W(d)$ is a binary random variable with the probability density function shown in (6-4), where $P_{U,W}(d)$ is the probability of occurrence of UDP for a given bandwidth.

$$f_{\xi_W}(y) = \left(1 - P_{U,W}(d)\right)\delta(y) + P_{U,W}(d)\,\delta(y-1) \tag{6-4}$$

The $P_{U,W}(d)$, however, is also a function of distance. Based on the results of path-loss modeling for total power and the DP presented in section 4 we assume that the probability of UDP in locations close to the transmitter and locations far from the transmitter are substantially different and we need to partition the model. We use the 10m break-point found in chapter 5 and mentioned in other researches [Cas02] to partition the behavior of the error in the two regions. Then for distances shorter than the break-point $P_{U,W}(d)$ is modeled as $P_{close\ U,W}$ and beyond the break point as $P_{far\ U,W}$.

$$P_{U,W}(d) = \begin{cases} P_{closeU,W} & d \le 10\,m \\ P_{farU,W} & d > 10\,m \end{cases} \tag{6-5}$$

Table 6.1 shows approximations to $P_{close\ U,W}$ and $P_{far\ U,W}$ for different bandwidths. As Rx moves away from Tx the DP power decreases, resulting in an increase in the probability of occurrence of the UDP condition.

To model $\varepsilon_{U,W}(d)$ we look into PDF of $\varepsilon_{U,W}(d)$ for different bandwidths. Figure 6.7 shows these PDFs. To examine the effect of UDP error, alone, we used only the UDP cases from our measurement database. We used a Gaussian distribution to model the distribution of $\varepsilon_{U,W}(d)$ as,

$$\varepsilon_{U,W}(d) = G\left(m_{U,W}, \sigma_{U,W}\right) \tag{6-6}$$

$$f_{\varepsilon_{U,W}}(z) = \frac{1}{\sigma_{U,W}\sqrt{2}} e^{-\frac{\left(z-m_{U,W}\right)^2}{2\sigma_{U,W}^2}} \tag{6-7}$$

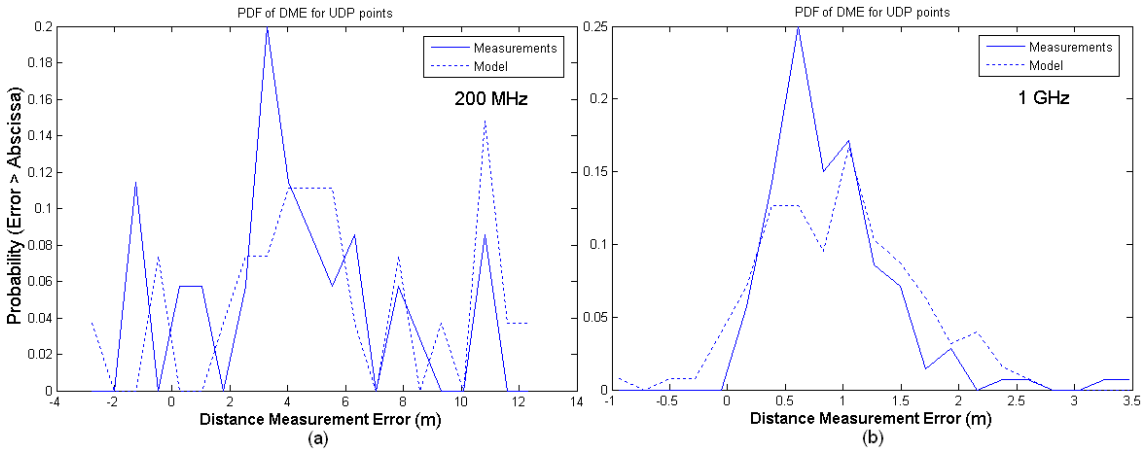

Figure 6.7: PDF's of DME for UDP, (a) 200 MHz, (b) 1 GHz

Table 6.1: Typical values of model parameters derived from the measurements

W (MHz)	$m_{M,W}$ (m)	$\sigma_{M,W}$ (cm)	$P_{closeU,W}$	$P_{farU,W}$	$m_{U,W}$ (m)	$\sigma_{U,W}$ (cm)
20	3.66	515	0	0.005	-12.83	0
50	1.57	205	0	0.009	24.48	21.1
100	0.87	115	0	0.091	5.96	358.5
200	0.47	59	0.006	0.164	3.94	289.0
500	0.21	26.9	0.064	0.332	1.62	80.9
1000	0.09	13.6	0.064	0.620	0.96	60.4
2000	0.02	5.2	0.070	0.740	0.76	71.5
3000	0.004	4.5	0.117	0.774	0.88	152.2

Table 6.1 shows the values of $m_{U,W}$ and $\sigma_{U,W}$ for different bandwidths obtained from the measurements. Figure 6.8 shows the complementary CDF comparison between the measurement results and the model for the UDP points.

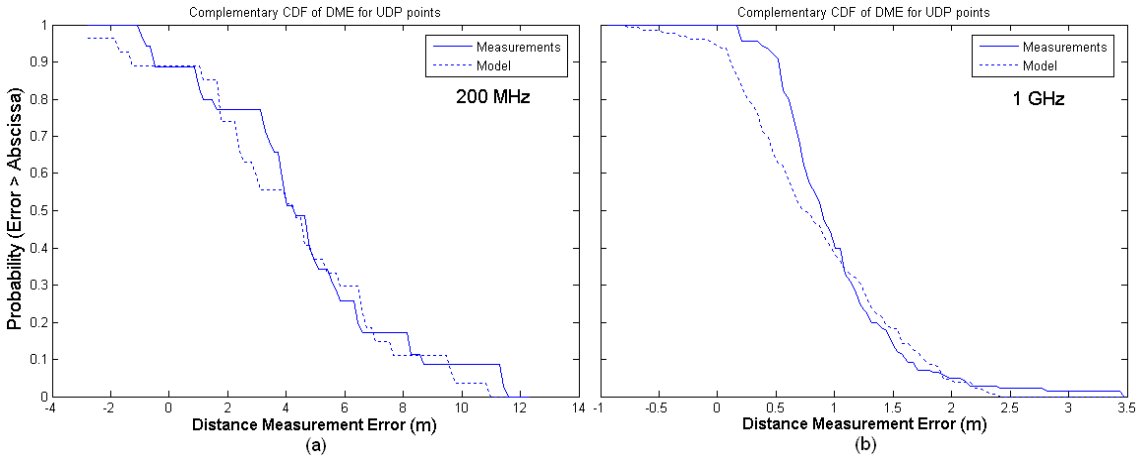

Figure 6.8: CCDF comparisons between measurements and model for UDP points, (a) BW = 200 MHz, (b) BW = 1 GHz.

6.5 The Overall DME Model

If we combine our results of multipath and UDP modeling, the overall model for estimated distance measurement is,

$$\begin{aligned}\hat{d} &= d + MDME + \xi_W(d)UDME \\ &= d + G(m_{M,W}, \sigma_{M,W})\log(1+d) + \xi_W(d)G(m_{U,W}, \sigma_{U,W})\end{aligned} \tag{6-8}$$

where,

$$f_{\xi_W}(y) = (1 - P_{U,W}(d))\delta(y) + P_{U,W}(d)\delta(y-1) \tag{6-9}$$

This model relates the distance measurement error to the distance and bandwidth of the system. Figure 6.9 shows the scatter plots of measurements and model for bandwidth of 200 MHz and fig. 6.10 shows the scatter plots for 1GHz bandwidth.

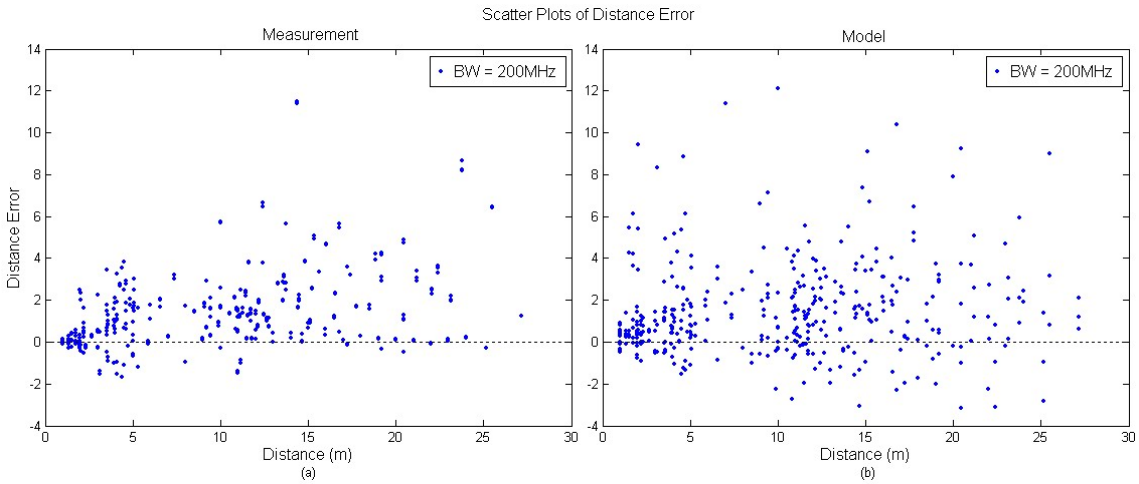

Figure 6.9: Scatter Plots of DME for 200 MHz, (a) Measurements, (b) Model

Figure 6.11 compares the complementary CDF of the distance measurement error obtained from empirical UWB measurements and the overall model described by (6-8) and (6-9) for bandwidths of 200MHz and 1GHz. The bandwidth of the UWB measurements taken at 3-8 GHz is adjusted to these two values to provide a fair comparison. The model shows close agreement with the empirical data.

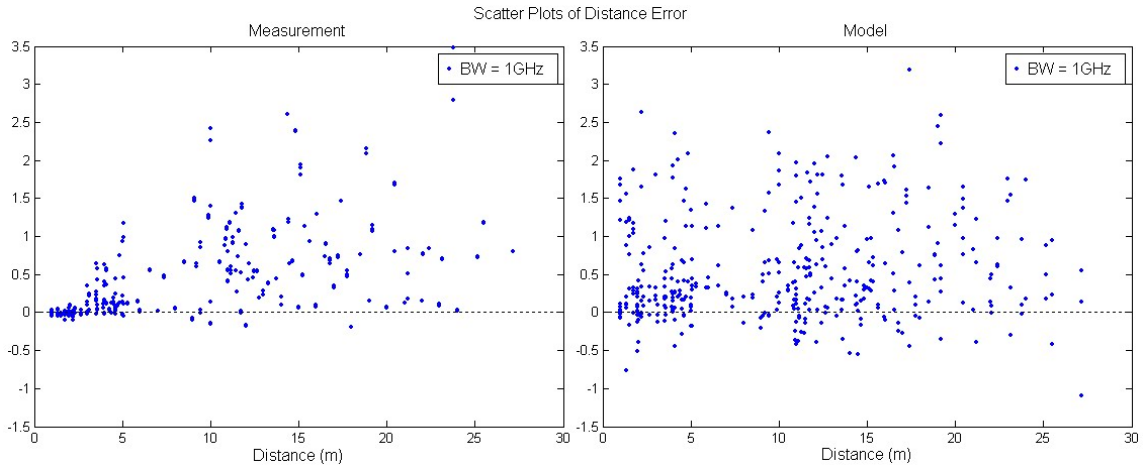

Figure 6.10: Scatter Plots of DME for 1 GHz, (a) Measurements, (b) Model

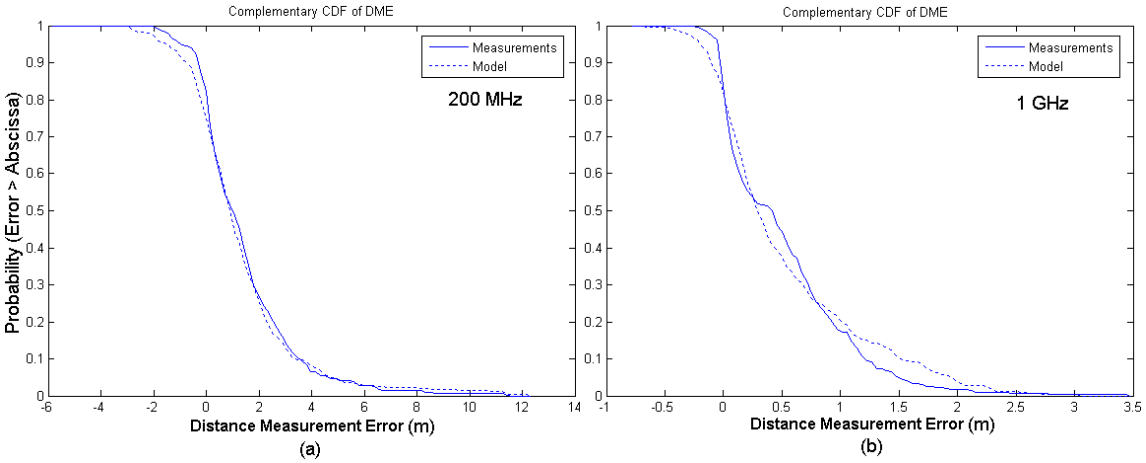

Figure 6.11: CCDF comparisons between measurements and model, (a) BW = 200 MHz, (b) BW = 1 GHz.

6.6 Effect of Bandwidth on DME

DME can be considered as a performance benchmark for ranging systems. A similar concept is Bit Error Rate (BER) in communication systems. Here we consider the effect of bandwidth on MDME and UDME separately and after that we study the bandwidth effect on total DME.

6.6.1 Effect of bandwidth on MDME

In deployment of all of wireless networks, coverage is one of the most important goals. Therefore, we design networks to have satisfactory coverage in the targeted areas. The same rule applies to indoor geolocation networks. When we have coverage for a geolocation system, this means that the covered area is mostly of the DDP type. As a result in most of the covered area MDME that we have to deal with is the DME type.

To show the effect of bandwidth on MDME first we choose a Tx-Rx location and then we examine the channel starting from a low bandwidth and moving to higher bandwidths. Fig. 6.12 shows three channel profiles of one measurement from a Tx-Rx location. The actual distance between Tx and Rx is 21 meters. In the first figure, the bandwidth of the system is 20MHz (the bandwidth reduction is accomplished using post processing) and the estimated distance is 18.5 meters. In the second figure, the bandwidth is 200MHz and the estimated distance is 20.61 meters. Finally, in the third figure, the bandwidth is 2GHz and the estimated distance is 20.86 meters.

It can be observed from the figures that when the bandwidth increases the paths of the channel profile are being resolved with increasing accuracy. Stated another way, with increasing the bandwidth, channel profile gets closer to channel impulse response. As a result, the MDME becomes smaller and smaller. It should be noted that there is some amount of error associated with each measurement that is due to error in physical measurement of the distance between Tx and Rx.

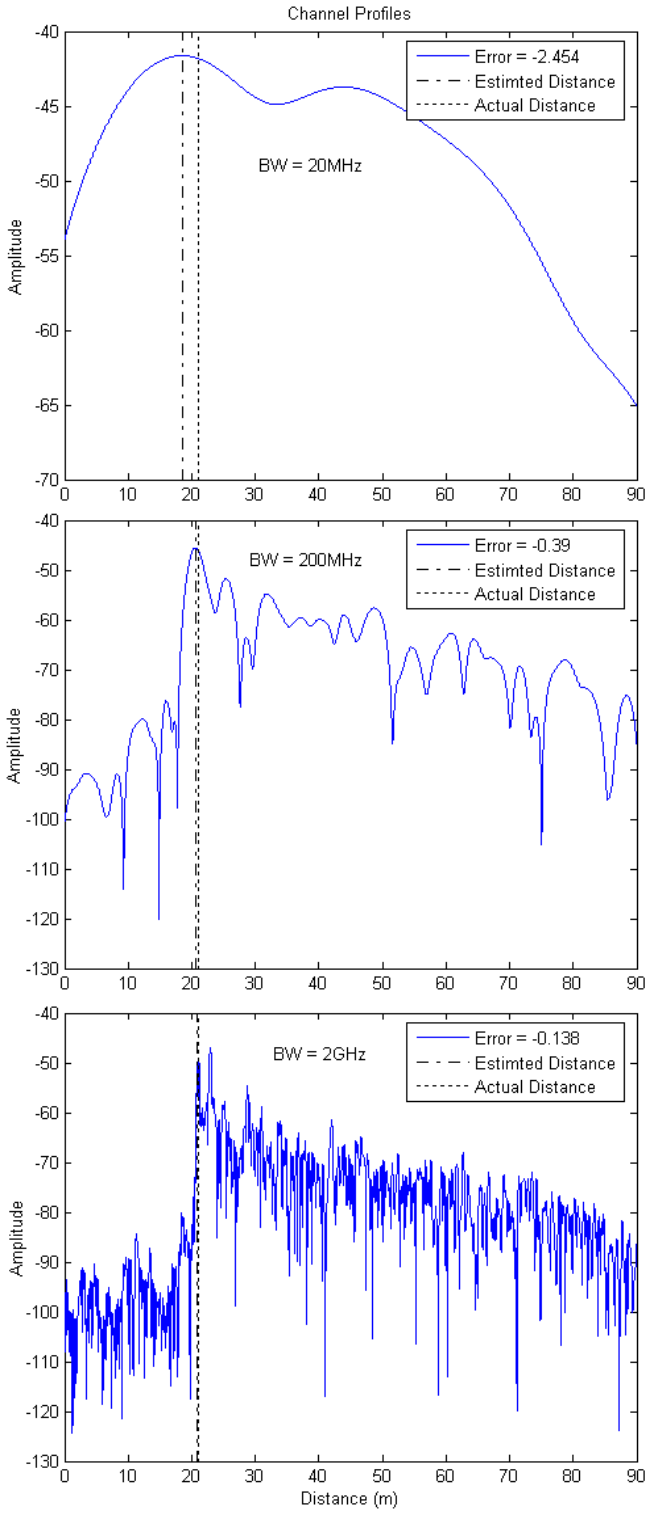

Figure 6.12: Three DDP Sample Channel Profiles from a same measurement with different bandwidths: (a) 20MHz, (b) 200MHz, (c) 2GHz

We can reach the same conclusion from another point of view. If we have a narrower bandwidth, the paths in time-domain become wider. Therefore, they become mixed with one another and the channel profile becomes a summation of these paths. As the bandwidth becomes narrower, each path becomes wider and has less resolution and turns the channel profile into form steadily more different from its original, which is the channel impulse response. Therefore, when the bandwidth decreases, MDME increases.

To validate this claim, Fig. 6.13 shows complementary CDF of MDME of the three bandwidths 20, 200, and 2000 MHz, the same set of bandwidths that was used in Fig. 6.12. It can be seen that when the bandwidth increases MDME decreases. Also, Fig. 6.14 shows Root Mean Square Error (RMSE) of MDME; it shows that by increasing the bandwidth the performance of the system in DDP areas improves i.e., MDME decreases. RMSE can be derived from,

$$RMSE\left(x\right)=\sqrt{\frac{\sum_{i=1}^{n}\left(\hat{x}_i-x_i\right)}{n}} \tag{6-10}$$

which, x is a set of values estimated by a set $\hat{x}$ and the subscript i is the i-th element of each set.

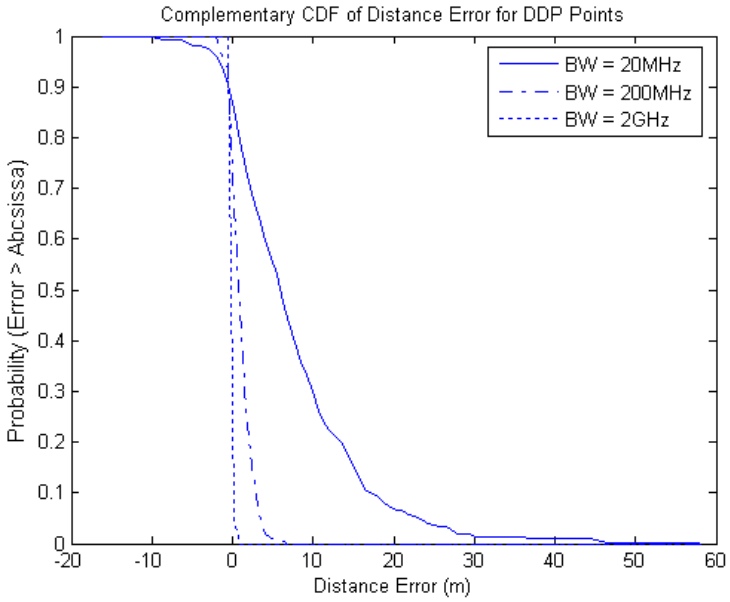

Figure 6.13: Comparison of CDFs of MDME for DDP points for three different bandwidths

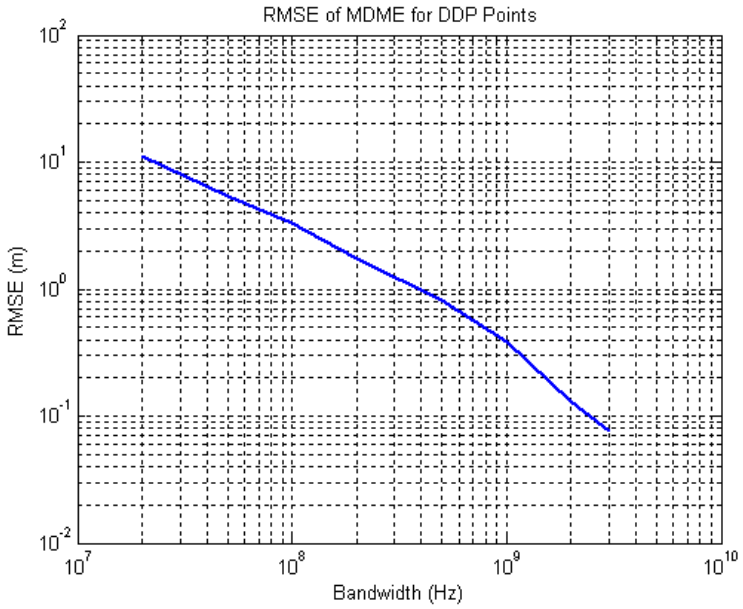

Figure 6.14: RMSE of MDME versus Bandwidth for DDP Channel Profiles

6.6.2 Effect of bandwidth on UDME

Unlike MDME, which always exists and is dominant in the covered area, UDME occurs only on occasion and it usually happens in the areas where the coverage is not certain, around the border between the covered area and the non-covered area. However, when it happens, it usually dominates the overall DME, because most of the time it has large values relative to MDME. Therefore, studying the behavior of UDME is as important as studying MDME.

If we go back to identify the cause of UDP, we realize that it happens because of the detection threshold. But the threshold, itself, is determined by two factors: noise level and amplitude of the strongest path. The former happens when the coverage is fading away, attenuating the power of the DP and other paths as well. On the other hand the latter factor is due to the limitations in dynamic range of the receiver and also side-lobe of the strongest path. Usually, the latter case occurs when the DP is shadowed, but there are other strong paths that can reach the receiver. As a result, we can divide UDP cases into UDP-Coverage and UDP-Shadow. Sometimes for one channel profile both of these causes exist, and in this case the UDP point can be in both categories.

Results of measurements show that probability of having UDP is highly dependent on the bandwidth of the system. Fig. 6.15 shows probability of having UDP versus bandwidth of the system for both types of UDP. To analyze this issue we provided Fig. 6.16, a plot of three channel profiles belonging to one measurement from a Tx-Rx pair, but with different bandwidths. It can be seen that with higher bandwidths

the amplitudes of the paths are weaker. Thus, as we increase the bandwidth, probability of having UDP will increase.

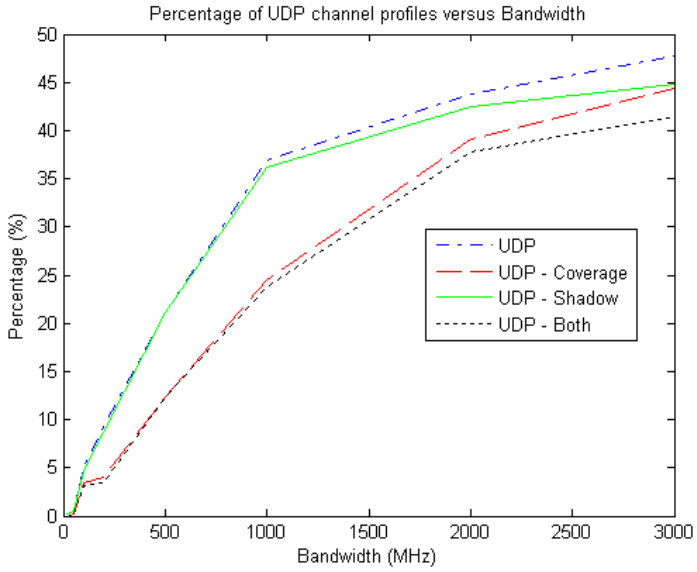

Figure 6.15: Probability of having UDP versus Bandwidth

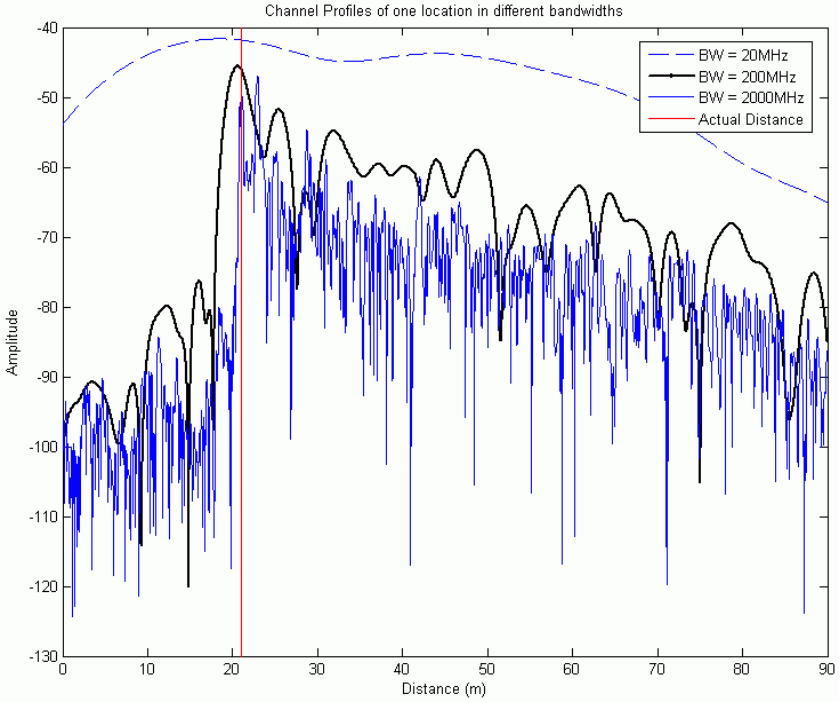

Figure 6.16: Three Sample Channel profiles from from a same measurement with different bandwidths: (a) 20MHz, (b) 200MHz, (c) 2GHz

Since the error arising from the UDP is large, one must consider that increasing the bandwidth cannot always help in improving performance of the system. Fig. 6.17 shows complementary CDF of UDME for the three bandwidths 20MHz, 200MHz, and 2GHz. In this figure, we used only the profiles that are UDP, but it must be noted that it is not possible to show only UDME results, since the MDME part always exists. Thus, even if we want to analyze UDME we cannot avoid MDME.

Fig. 6.18 shows RMSE of UDP profiles for different bandwidths. The interesting point here is that increasing the bandwidth from 2GHz to 3GHz increases UDME. Thus using this plot we can find the optimum bandwidth for UDP errors based on this specific data-set.

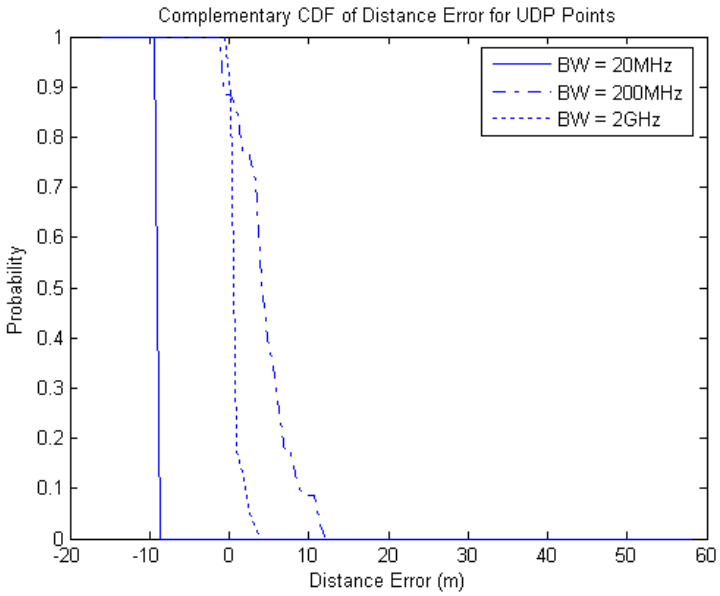

Figure 6.17: Comparison of CDFs of DME for UDP points for three different bandwidths

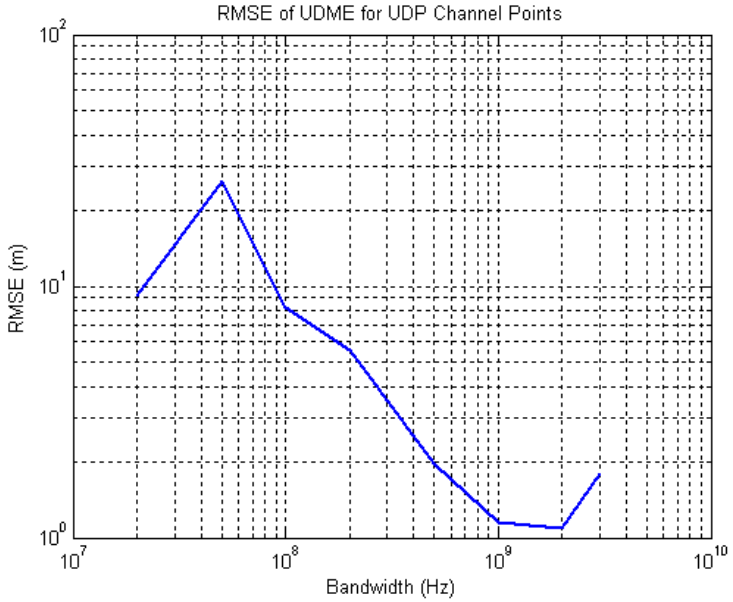

Figure 6.18: RMSE of UDME versus Bandwidth for UDP Channel Profiles

6.6.3 Effect of bandwidth on Overall DME

Thus far we have investigated and studied the effect of system bandwidth on MDME and UDME. However, based on (6-2), DME consists of both these errors. At lower bandwidths MDME has larger values and UDME occurs less frequently. On the other hand at higher bandwidths MDME has almost negligible values, though UDME occurs more often. Therefore, we can conclude that at low bandwidth, MDME is the dominant type of error and at high bandwidths UDME is the dominant error.

Fig. 6.19 shows RMSE of DME for different bandwidths. Interestingly the optimum bandwidths is somewhere between 1 and 2GHz. The values of RMSE for different bandwidths for MDME, UDME, and DME are shown in table 6.2.

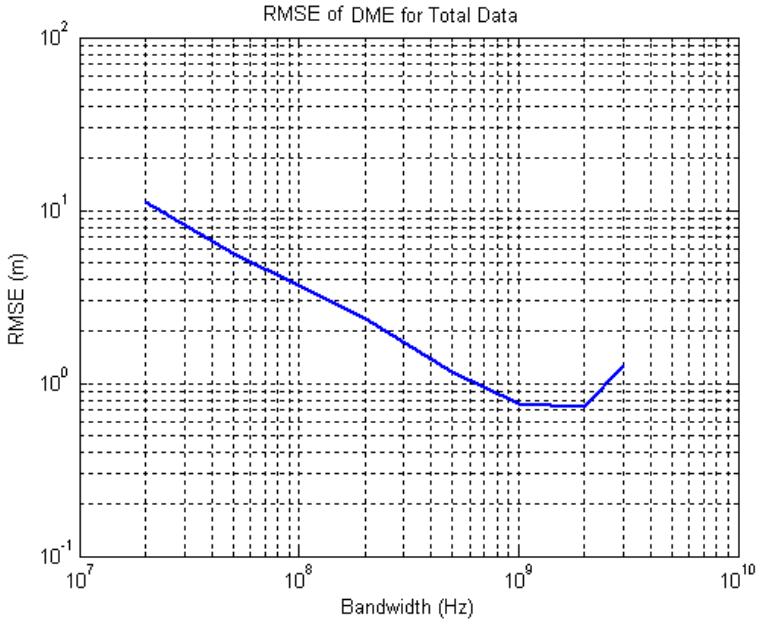

Figure 6.19: RMSE of UDME versus Bandwidth for UDP Channel Profiles

Fig. 11 shows RMSE of DME for points with short distances between the transmitter and the receiver, in this figure all the distances are less than 10m. Fig. 12 shows similar graph for points farther than 10m. It can be seen that when the distance between the Tx and Rx increases UDME becomes more important, since the graph becomes more similar to UDME graph.

Table 6.2: Typical values of RMSE for different bandwidths derived from measurements

w (MHz)	*RMSE of MDME* (m)	*RMSE of UDME* (m)	*RMSE of DME* (m)
20	11.24	9.17	11.24
50	5.36	26.18	5.67
100	3.28	8.24	3.69
200	1.72	5.55	2.35
500	0.82	1.96	1.16
1000	0.38	1.14	0.76
2000	0.13	1.09	0.73
3000	0.07	1.81	1.25

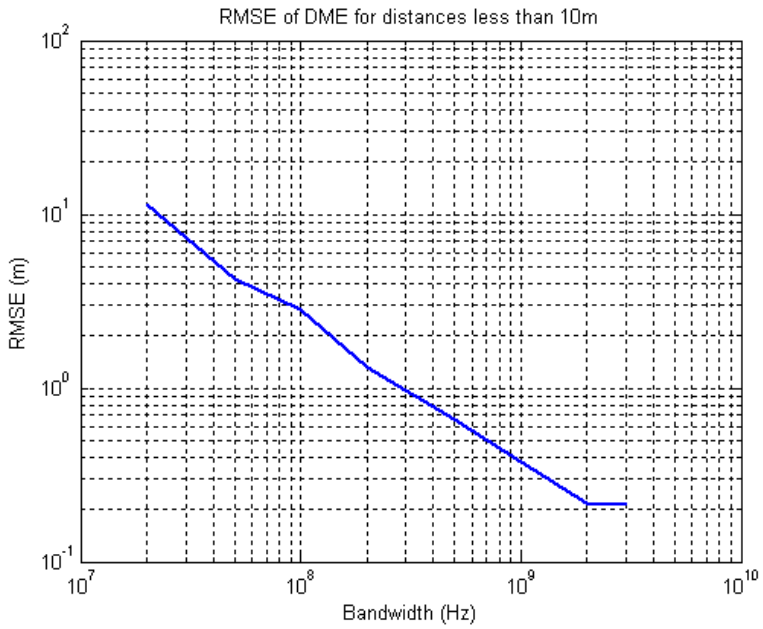

Figure 6.20: RMSE of DME versus Bandwidth for channel profiles with distances less than 10m

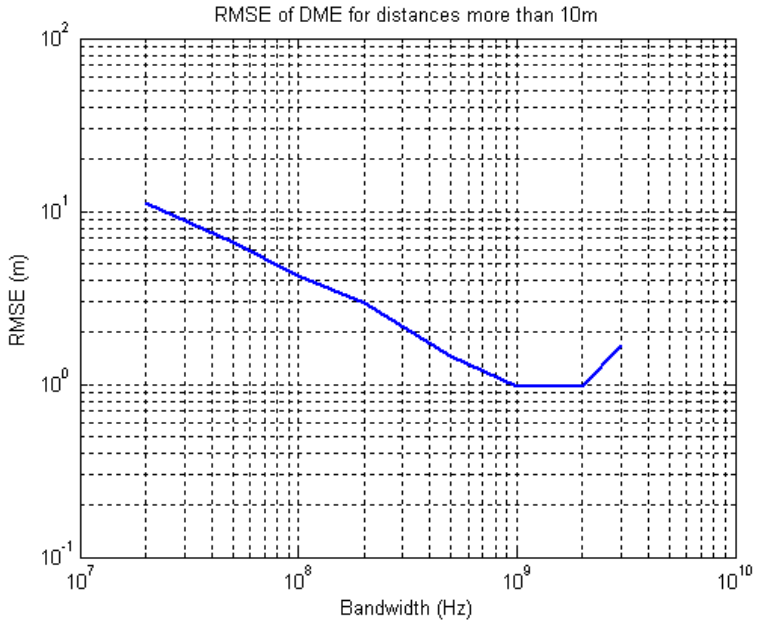

Figure 6.21: RMSE of DME versus Bandwidth for channel profiles with distances more than 10m

6.7 Summary

In this chapter we have introduced a model for DME based on UWB measurements. We have shown that the DME consists of two major elements: MDME and UDME. The MDME always exists and the UDP-DME happens only in the case of UDP occurrence. We have modeled each one of them and provided a model for the whole DME separately. We have then related the DME to the bandwidth of the system and shown that as we increase the bandwidth the MDME decreases, but the UDME has a more complicated behavior. This behavior is dependent on the distance between the receiver and the transmitter and has an optimum value. As a result the overall geolocation system has an optimum bandwidth and this bandwidth depends on the distance.

Part III

Analysis and Conclusion

The last part of this dissertation includes two chapters and is considered as a closing part. In Part III we address the following issues.

Chapter 7: An analytical approach to calculating probability of UDP

This chapter provides an innovative approach to calculate the probability of UDP occurrence. It uses the power of DP and the total power and shows that when the average DP power goes below the threshold then we will have UDP.

Chapter 8: Conclusion and future work

This chapter summarizes the works done during this dissertation and provides some directions for continuation of in this field.

Chapter 7

An Analytical Approach to Calculating Probability of UDP

7.1 Introduction

In chapter 6 during the process of modeling the DME it has been shown that the major challenge of the indoor geolocation is the occurrence of UDP. In this chapter first we have an introduction to the concept of UDP in and then review the existing literature on this topic, followed by different definitions. Then based on the concept of the UDP we provide an innovative approach to calculate the probability of UDP from site-specific information such as size of the rooms and building materials. As an alternative approach we can use the path-loss models developed in chapter 5 to find the

UDP probability. And at the end we compare the results of the analysis with the results of measurements.

7.2 The Concept and Definitions of UDP

The main challenge for indoor geolocation using TOA is the existence of the UDP that was first reported in [Pah98]. In UDP conditions the DP is blocked by objects and is buried under the noise level, so the receiver detects an erroneous path as the direct path, and it causes significant distance measurement errors. Fig. 1 represents a typical UWB measurement of the channel impulse response with a bandwidth of 3GHz to describe the occurrence of the UDP condition. The vertical axis shows the signal strength and the horizontal axis is the distance $d = \tau c$ in which τ is the delay of arrival of a path and c is the speed of light. The actual distance between the transmitter and the receiver is 25.5 meters and due to UDP condition this distance is detected as 38.5 m resulting in 13 meters error in distance measurement using TOA.

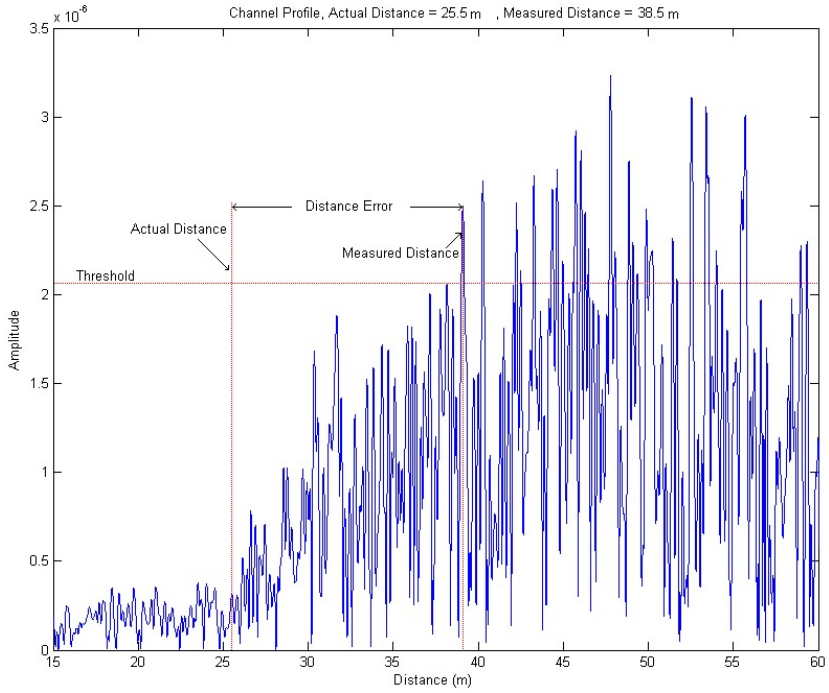

Figure 7.1: A typical UWB measurement UDP channel profile in time domain with a bandwidth of 3GHz

7.2.1 Existing reports on UDP

First report on UDP case observation originally goes back to [Pah98] [Kri99b], where it was addressed as one of the three classes of channel profile (dominant DP, non-dominant DP, and UDP).

In [Als04] performances of TOA estimation algorithms in these three classes of environments were studied. It was concluded that in UDP cases, due to large error, neither complex TOA detection algorithms like EV/FBCM [Li04] nor increasing the system bandwidth helps detecting the DP.

In [Ala03a] modeling of the distance error was considered, and Ray-Tracing software was used for this purpose. It was concluded that UDP cases follow a different pattern in distance error, where their corresponding error was modeled differently.

Finally, in [Ala04] [Ala05b], UDP cases were considered separately for distance error modeling. The results showed that as the bandwidth of the system increases, probability of having UDP increases. The common note in all of the above papers is that when we have a UDP case, we can not detect the first path and this can cause large errors in geolocation systems and degrades the performance of TOA estimation algorithms.

7.2.2 Definitions

As it appears from its name, we say that a channel profile is UDP, when it is not possible to detect the DP. But in order to differentiate between channel profiles in a systematic method, we need to have a more specific definition to be able to implement UDP detection algorithms.

One method is the theoretical definition that fits in the case where we have infinite bandwidth. We can use ray tracing as an example of an infinite bandwidth system. Fig. 7.2 shows a sample of a UDP point that has 3.1 meter distance between Tx and Rx. As you can see the DP has lost it's amplitude due to the obstacles in LOS path and has gone below the threshold. The threshold is adjusted by the noise power, side-lobe amplitude, and dynamic range of the receiver. In this method we assume that all the paths are resolved, so we can decide whether a channel profile is a UDP or not. Also in this method, which is the closest one to the original concept of UDP, bandwidth has no effect, only two parameters are important: DP power and threshold. But the problem of this method is that since in most of the cases our input is the channel profile we can not have access to individual paths.

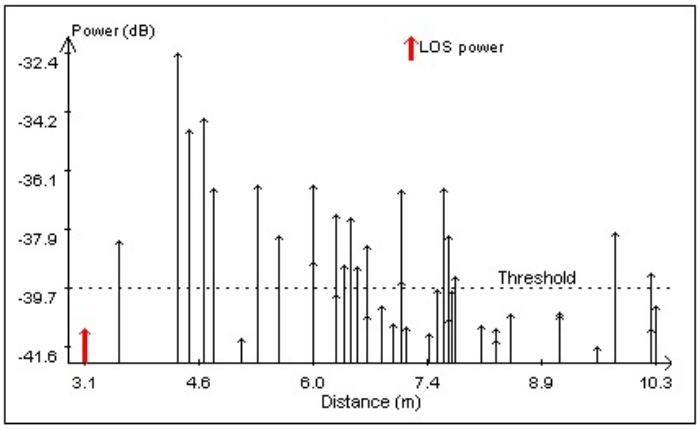

Figure 7.2: A sample UDP channel impulse response showing suppressed amplitude for the DP

The second method, which is more practical, indirectly detects the UDP. It says that when the error in the TOA estimation exceeds inverse of the system bandwidth we have a UDP case. Based on figure 7.3 we have:

$$Pulsewidth = \frac{2}{Bandwidth} \tag{7-1}$$

The error that is caused by the multipath [Ala04] almost always lies between TOA of the DP plus/minus half of the pulse-width. So, whenever absolute value of the error is greater than half of the pulse-width, or inverse of the system bandwidth, we have UDP error.

$$\begin{aligned} |Error| &> \frac{1}{Bandwidth} \quad \Rightarrow \quad UDP \\ |Error| &\leq \frac{1}{Bandwidth} \quad \Rightarrow \quad NUDP \end{aligned} \tag{7-2}$$

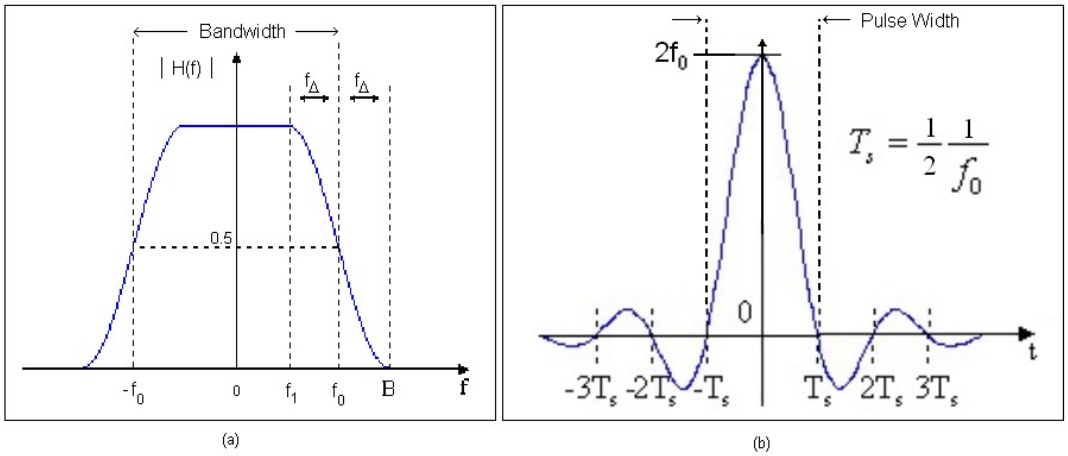

Figure 7.3: A sample of raised cosine filter in both time and frequency domain

Based on this definition UDP occurrence depends on the bandwidth. This method does not use the original definition of UDP to detect such a case; rather it uses a practical method.

The third definition is both practical and directly defines UDP. That is: In a channel profile if the amplitude of the DP is less than the threshold, then we have a UDP case. Threshold is described in the first method. The difference between this and the first one is that in here UDP case depends on the system bandwidth, but as the bandwidth increases the two definitions become equivalent.

In the analysis described in here, for developing the model we assume infinite bandwidth; hence we use the first definition for that part. But when we want to compare with the results of measurements, we use the third method for detecting UDP cases in our measurement database.

7.2.3 Three regions of DP detection

In [Pah98], [Als03], and [Als04] the indoor locations were divided into three regions of dominant DP, non-dominant DP, and UDP. In the first two categories, DP is detectable. It's only for the UDP case that DP is not detectable. When the receiver is close to the transmitter, the power of the DP is very strong. As a result, the DP can be easily detected which means very accurate ranging. This region of operation is usually referred to as DDP. However as the node moves away from the reference point the strength of the DP decays gradually, where it reaches a region where the DP is no longer as strong. In fact it is weakened and in certain instances it would be UDP. Figure 7.4 further explains the three region DME model.

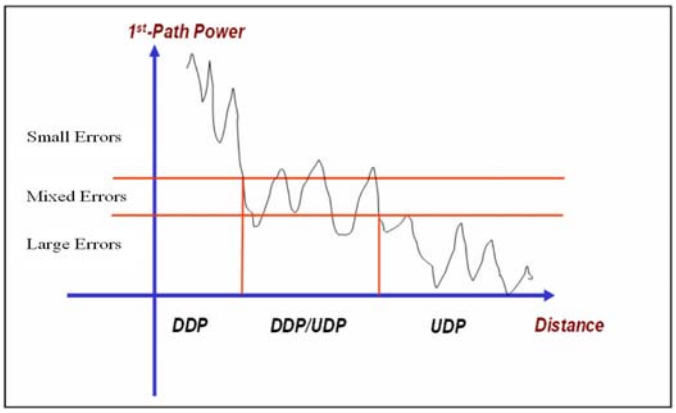

Figure 7.4: Illustration of the relationship among first-path power, distance and DME

Therefore, we can say that we enter the UDP region when the power of DP goes below the detection threshold, and we come out of UDP and enter NC region when the total power goes below the threshold. Figure 7.5 shows an illustration for the statistical average power of the DP and the total power. We can observe that as long as the average power of the DP is above the threshold we have DDP as the dominant case.

When it goes below the threshold, UDP case becomes dominant. And when total power reaches below the threshold we have NC, since we don't receive any signal. It should be noted that in practice, change from a region to another happens gradually, but in each region the corresponding case is the dominant one.

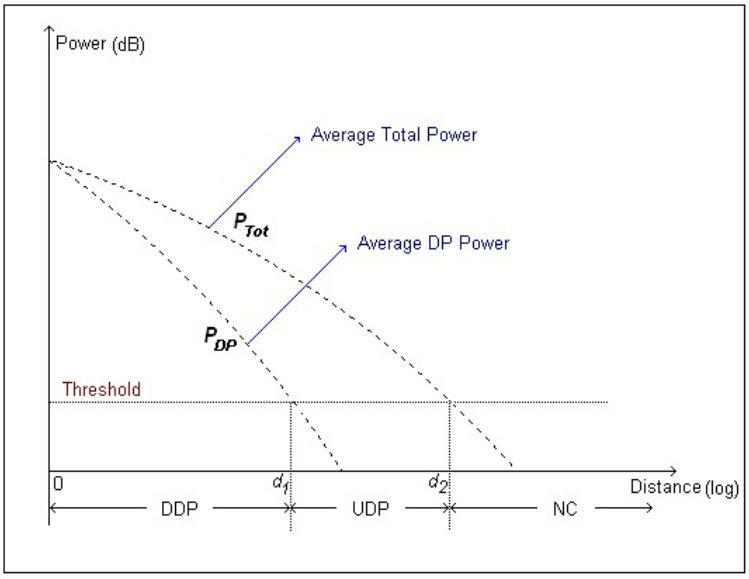

Figure 7.5: A sample for average of the DP and the total power and corresponding regions

7.3 Calculating Probability of UDP

7.3.1 Simple one-zero model

In this section we want to develop an analysis for calculating the probability of UDP. Based on the three regions of DP detection we want to calculate the average probability of UDP in a typical indoor environment. For simplicity, we assume that in the DDP region, probability of UDP is zero and in the UDP region it is one.

$$P_{UDP} = \begin{cases} 0 & d \le d_1 \\ 1 & d_1 < d \le d_2 \\ N/A & d_2 < d \end{cases} \quad (7\text{-}3)$$

where distances d_1 and d_2 are the radii of the boundaries of the regions that are determined from a Fig. 7.5.

Since the boundaries of each region are determined with the distance from Tx, which we assume that is constant in every direction, the shapes of the boundaries are circles. Figure 7.6 shows these regions. The first region is DDP and we assume that in this region probability of having UDP is zero. The second region is UDP and the probability of having UDP is assumed to be one. In the third region since there is no coverage probability is not defined.

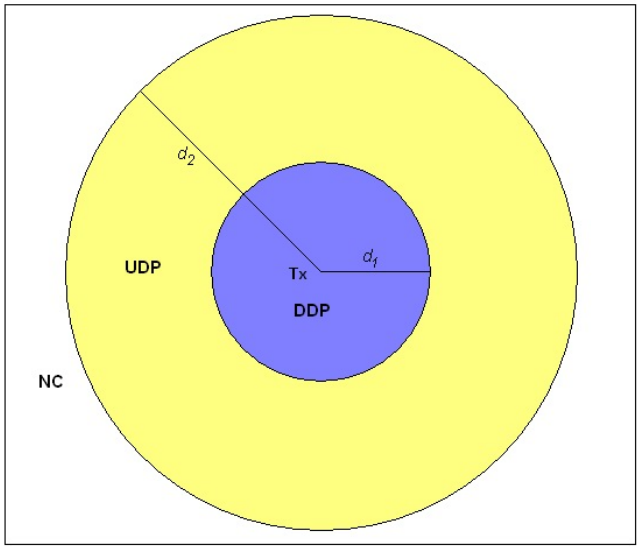

Figure 7.6: **Three regions of DP detection in 2-D plane**

To calculate the average probability of UDP, we assume that a point will be selected uniformly within the bigger circle, so that it includes the smaller one also. As a

result, the probability of having a DDP case is proportional to the area of the DDP region and for UDP it is proportional to the area of the UDP region. Hence,

$$Prob_{DDP} = \frac{Area_{DDP}}{Area_{Total}} = \frac{\pi d_1^2}{\pi d_2^2} = \left(\frac{d_1}{d_2}\right)^2 \tag{7-4}$$

$$Prob_{UDP} = \frac{Area_{UDP}}{Area_{Total}} = \frac{\pi d_2^2 - \pi d_1^2}{\pi d_2^2} = 1 - \left(\frac{d_1}{d_2}\right)^2 \tag{7-5}$$

As shown in the figure, unlike the free space, in an indoor environment the power line is not a straight line anymore. In some literature they estimate this curve with one or two straight lines [Pah05]. In chapter 5 we introduced path-loss equations with one or no break-points to deal with this issue. In this chapter however we use the results of our proposed model for the powers to calculate d_1 and d_2, this model will be introduced in the next section. Assuming that the received power of DP is shown by $P_{DP}(d)$ and total received power by $P_{Tot}(d)$. It can be seen from Fig. 7.5 that in distances d_1 and d_2 both $P_{DP}(d)$ and $P_{Tot}(d)$ are equal to "Threshold" (P stands for power):

$$P_{DP}\left(d_1\right) = P_{Tot}\left(d_2\right) = Threshold \tag{7-6}$$

So, once we have $P_{DP}(d)$ and $P_{Tot}(d)$ then d_1 and d_2 can be derived from the plots of P_{DP} and P_{Tot} versus distance.

7.3.2 Modeling the received power

In previous section we explained how information about the received signal strength of DP and total power can help us calculating the average probability of UDP in an area.

One approach is to use path-loss models introduced in chapter 5 to calculate probability of UDP. The other approach is to use a model for calculating the power of DP and total power, which will be explained in the following section.

7.3.2.1 A site-specific model for the received power

In this section we want to introduce a model to calculate the received DP power and total power. The DP power can be considered as one path that passes through walls and reaches to the receiver. Its behavior between the two intersections with the walls is like free space, but at each intersection there is some loss that depends on the type of wall or any other obstacle.

Figure 7.7 shows what happens to DP power clearly. The solid blue line is the DP power assuming that the frequency of occurrences of the obstacles is steady. In other words we can consider an average number as the distance between the two intersections, we show it with d_f or average free space distance. We also assumed that the power drop in each of these intersections is the same, so we consider it as average loss of walls, or L_W. But since the distance scale is logarithmic, these equal distances do not appear equal in the plot. As a result the average DP power no longer will stay as a straight line as shown with a dotted line in the figure. In fact, as mentioned before people estimate it with one, two, or more straight lines [Pah05], as we did for some of our path-loss models in chapter 5.

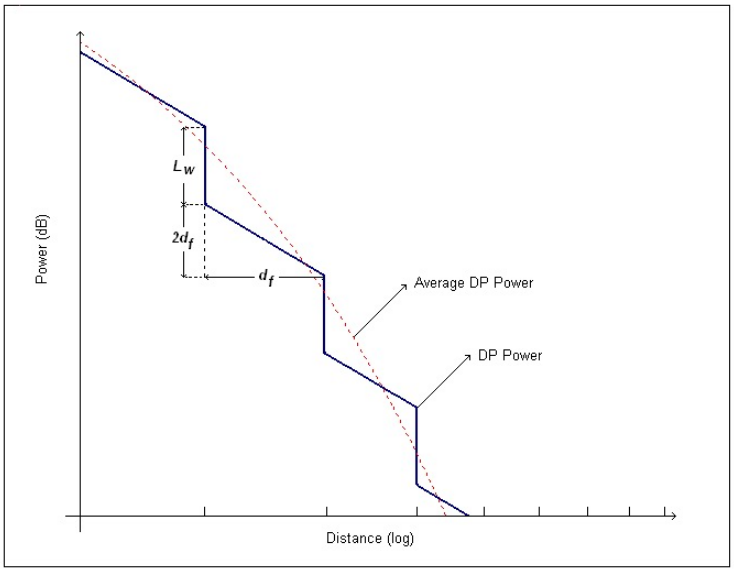

Figure 7.7: A sample of typical DP power and average DP power versus distance in an indoor area

If we assume that the DP has passed through *n* transmissions and *m* reflections, and the total path length is *d*, then:

$$P_{DP}(d) = \frac{P_0 T^{2n} R^{2m}}{d^2} \tag{7-7}$$

where P_0 is the received power at one meter, and T and R are transmission and reflection coefficients. In DP case we only have transmission, so (7-7) can be rewritten and transformed into dB as follows:

$$P_{DP}(d) = P_0 + n \cdot 10\log\left(T^2\right) - 20\log(d) \tag{7-8}$$

Matching (7-8) with Fig. 7.7 results in:

$$L_w = -10\log\left(T^2\right) \tag{7-9}$$

But the following relation holds for *n*:

$$n = \frac{d}{d_f} \tag{7-10}$$

Therefore, the final formula for DP power is as follows:

$$P_{DP}(d) = P_0 - \frac{d}{d_f} L_W - 20\log(d) \tag{7-11}$$

The values of L_W and d_f depend on the site geometrics and materials of the building. Depending on type of the wall, L_W can have values between 3-12 dB [Pah02b]. To find d_f we assume the rooms have rectangular shapes, and then we can find the average free space distance as follows [Has02]. If we consider the average size of the room with length "*a*" and width "*b*", then we have:

$$d_f = \frac{4}{6}\overline{\rho}_A + \frac{1}{6}\overline{\rho}_W + \frac{1}{6}\overline{\rho}_L \tag{7-12}$$

in which $\overline{\rho}_A$, $\overline{\rho}_W$, and $\overline{\rho}_L$ can be derived from (17) of [Has02].

Now we have enough information to calculate average DP power. In order to calculate total power once more we use the results of [Has02]. If we define *P(l)* as received power from the path length "*l*", then we have the following relation to calculate *P(l)*:

$$\begin{aligned} &for\ l \neq d && P(l) = P_0 l^{-2} e^{-\lambda l} e^{\lambda l (qT^2 + pR^2)} \\ &for\ l = d && P(l) = P_0 [l^{-2} e^{-\lambda l} e^{\lambda l (qT^2 + pR^2)} \\ & && + \left(d^{-2} T^{2n} - d^{-2} e^{-\lambda d (1 - T^2)} \right)] \end{aligned} \tag{7-13}$$

P_0 is the received power in one meter. λ is equal to the inverse of d_f, R and T are the average reflection and transmission coefficients, n is the number of walls between Tx and Rx, and p and q are functions of "l" and are probabilities of having reflection and transmission given intersection, respectively:

$$p(l) = \frac{1 - e^{-\lambda(l-d)}}{2} \tag{7-14}$$

$$q(l) = 1 - p(l) = \frac{1 + e^{-\lambda(l-d)}}{2} \tag{7-15}$$

Then the total received power is equal to the summation of all the received powers of any length.

$$P_{Tot}(d) = \sum_{i=0}^{\infty} P(d + i\delta) \tag{7-16}$$

where δ is a small amount of distance that can be chosen based on the desired resolution. Now to find d_1 and d_2 we just need to plug (7-11) and (7-13) into (7-6). But because of the complexity of the formulas there is no compact solution to derive d_1 and d_2 and they should be derived from the graphs and simulations.

7.4 Comparison between the results of measurements and models

7.4.1 Site-Specific Model

We used the phase I measurements to validate this model. Details of these measurements are explained in chapter 4.

In order to use the model three parameters must be determined for the model: average free-space distance (d_f), transmission (T), and reflection (R) coefficients. In [Has02] some parts of the third floor of AK building has been investigated. But we seek the average for all the three floors. It should be noted that the analysis has been done regardless of the bandwidth of the system, in another word the bandwidth is assumed infinity. Hence, to be consistent with the analysis the measurement is also done in UWB with 3GHz bandwidth. The average value for d_f, has been calculated as 3, using a=4 and b=6. The average values for T and R, are 0.5 and 0.4.

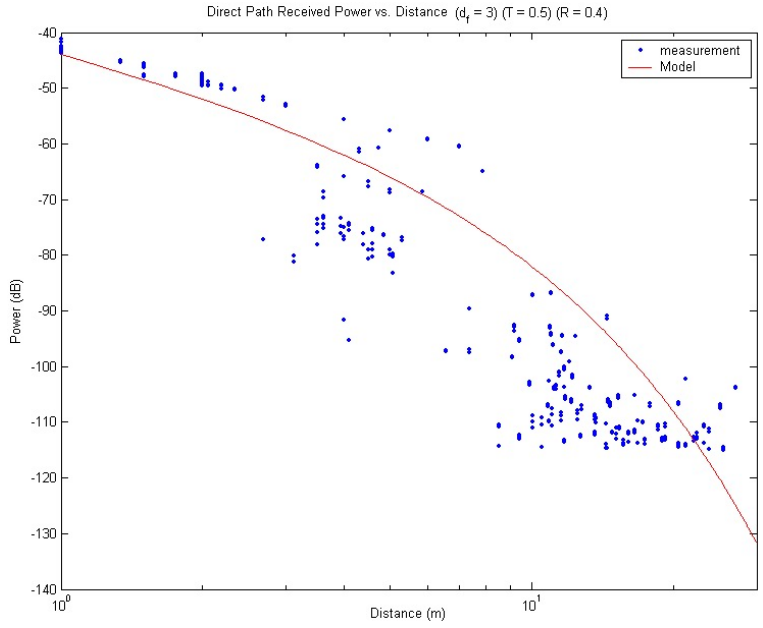

Figure 7.8: Comparison between received DP power from measurements and model

Figure 7.8 shows the DP power from measurements data and model. Similarly, Fig. 7.9 shows the total power from measurements data and model. As it can be seen the received measured powers vary a lot, there are two causes for this: The first one is shadow fading and the second one is the existence of different scenarios together in one plot. Our measurement plan consists of LOS, and OLOS data from different rooms and floors. Overall there is a match between the average of the received power from measurements and model. This helps us to determine the boundaries of DDP, UDP, and NC regions and calculate probability of UDP.

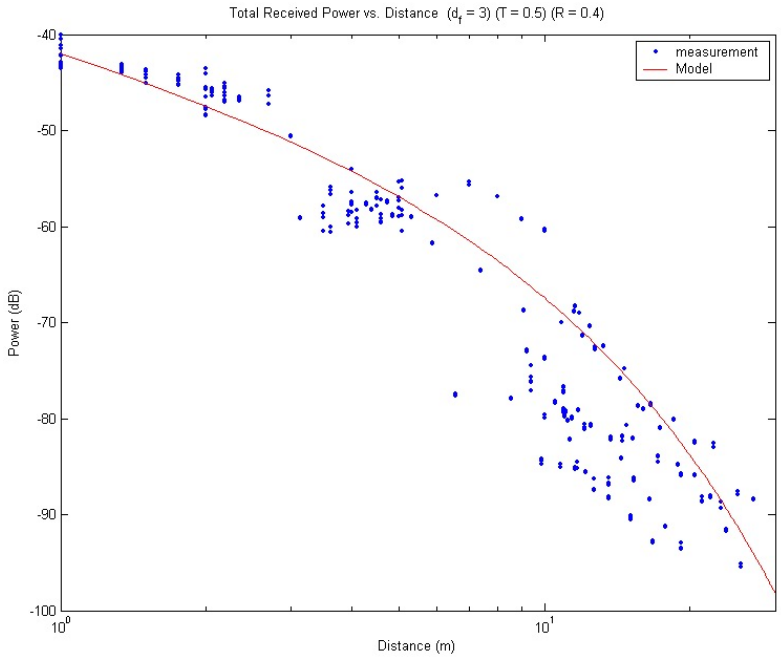

Figure 7.9: Comparison between received total power from measurements and model

Fig. 7.10 shows the total power, DP power, and free-space power as a comparison. Based on the threshold of -110 dB, d_1 and d_2 are determined as 20 and 39 meters, respectively. So now using (7-4) and (7-5) we can calculate probability of UDP, but we have to pay attention that our measurement data is not uniformly distributed on a

circle with radius d_2. As a matter of fact our longest distance is about 30 meters so we have to replace the value of d_2 with 30 meters to make our estimation closer to reality.

$$Prob_{UDP} = 1 - \left(\frac{d_1}{d_2}\right)^2 = 1 - \left(\frac{20}{30}\right)^2 = \frac{5}{9} = 0.55 \tag{7-17}$$

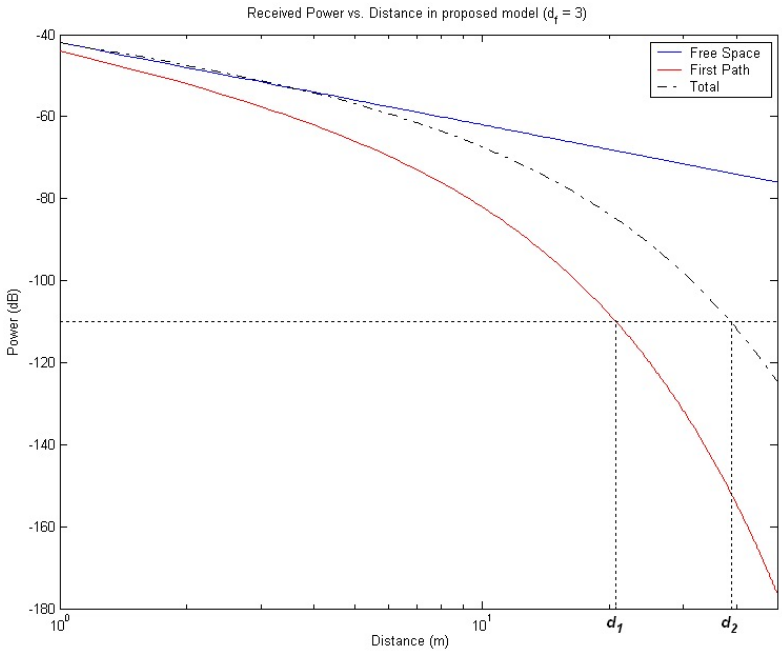

Figure 7.10: Comparison between received DP power, total power, and free-space power

The results of the measurements in 3 GHz show that out of 405 points, 195 points are UDP and 210 points are DDP. This results to UDP probability of 0.481 that shows our estimation is very close to the measurement data. To facilitate accessing the information, Table 7.1 shows the parameters derived from the measurement data and model. The standard deviation of the measurements from the model is 12.86 dB for the DP power and 6.01 dB for the total power.

Table 7.1: Typical values of model parameters derived from the measurements

Parameter	Value	Unit
L_w	-6	dB
d_f	3	Meter
d_1	20	Meter
d_2	39 (30)	Meter
R	0.4	N/A
T	0.5	N/A
P_{UDP}	~0.5	N/A

7.4.2 Path-Loss Model

To explain how we can calculate the probability of UDP here through an example we show the procedure. We use one of the path-loss models from the measurements in phase II and calculate the DDP and UDP regions. The detailed values of the path-loss models can be found in Appendix A, as a sample we use Fuller Labs. OTI, inter-floor, arbitrary point in section A.1.5. It must be noted that the path-loss models provided in chapter 5 are for total power and FDP. But the site-specific analysis provides the received power of the DP. The FDP and DP are not always the same; especially in UDP cases FDP has a higher power since the DP goes below the detection threshold. Because of this difference this method always carries some amount of error.

The average path-loss model for the total power in this scenario is given by,

$$L_T = \begin{cases} 42 + 35\log_{10} d & d \le 10 \\ 77 + 42\log_{10}\left(d/10\right)_T & d > 10 \end{cases} \quad (7\text{-}18)$$

The average path-loss model for the FDP power in this scenario is given by,

$$L_F = 42 + 53\log_{10} d \tag{7-19}$$

Since we are using the average power and we assume that the polarization of the antennas are parallel the random variables are all neglected. If we consider the detection threshold similar to previous case to -115 dB then for the total power coverage we have:

$$P_{F\min} = -115 = -42 - 53\log_{10}(d_1) \tag{7-20}$$

$$d_1 = 10^{\frac{115-42}{53}} = 23m \tag{7-21}$$

$$P_{T\min} = -115 = -77 - 42\log_{10}(d_2/10) \tag{7-22}$$

$$d_2 = 10 \times 10^{\frac{115-77}{42}} = 80m \tag{7-23}$$

$$Prob_{UDP} = 1 - \left(\frac{23}{80}\right)^2 = 0.91 \tag{7-24}$$

Therefore if we use this whole area uniformly probability of UDP is close to 90 percent.

7.5 Summary

In this chapter we have described the importance of UDP in indoor geolocation and discussed the concept and different definitions of UDP. We have also proposed a method for calculating the probability of UDP. Then we have introduced a model for the received power that helps calculation of probability of UDP using the above mentioned method. The results of the model show close prediction between measurements data and the model.

Chapter 8

Conclusions and Future Research

8.1 Conclusions
8.2 Future Research

8.1 Conclusions

In this section we provide a summary and conclusions on the research, which are drawn during the previous chapters. It should be noted that at the end of each chapter a summary of that chapter is provided. We explained that despite a considerable amount of research in indoor geolocation technologies, precise indoor geolocation still remains as a challenge. The fundamental problem is severe multipath conditions and frequent occurrence of UDP conditions in indoor areas. Therefore we devised empirical models for the behavior of the DME for development of more precise indoor geolocation systems. It was shown that a direct model provides a better fit for the DME than an indirect multipath model.

In Part I we have developed a model using measurement-calibrated RT software. It was shown that LOS and OLOS exhibit different behavior. The LOS locations all follow the same type of error and were modeled with a zero mean Gaussian distribution random variable proportional to distance. On the other hand the OLOS locations

sometimes behave much differently and follow another pattern. This pattern exhibits a larger amount of error, which is always positive. We have modeled these locations with an exponential distribution random variable. Then the OLOS model based on the data set used in chapter 2 consists of a weighted mixture of Gaussian and exponential. The summary of the model is provided in (8-1), showing that the parameters of the Gaussian parts of the model are function of the system bandwidth, but the exponential part is not.

$$\hat{d} = d + \begin{cases} d \cdot G\left(0, \sigma_{L,W}\right) & LOS \\ d.\left(W_G \cdot G\left(0, \sigma_{O,W}\right) + W_{Exp} \cdot Exp\left(\lambda\right)\right) & OLOS \end{cases} \tag{8-1}$$

In Part II of the thesis we enhanced our DME model with massive UWB measurements. We used four different buildings to consider different types of environments; these four types include a residential building, two different types of office buildings, and a manufacturing floor. One factor that differentiates these sets of measurements with other measurements is that they are targeted for geolocation applications. In each measurement we are interested in power of the DP and total power and DME. The DP power and DME are two essential factors for geolocation application and the total power is essential for communication coverage.

We then used the results of the measurements to develop a model for DME. We observed that the exponential errors reported in part I are in fact the result of a case called UDP. We then showed that DME has two different elements, MDME and UDME. The first one always exists, but the second one exists only when the DP is not detected. Therefore we provided a model to incorporate both of these errors. The model is shown in (8-2). We used a binary random variable ξ to incorporate the occurrence of

UDP cases. This model follows the results of measurements closely in a wide range of bandwidths from 50 MHz to 3 GHz.

$$\begin{aligned}\hat{d} &= d + MDME + \xi_W(d)UDME \\ &= d + G(m_{M,W}, \sigma_{M,W})\log(1+d) + \xi_W(d)G(m_{U,W}, \sigma_{U,W})\end{aligned} \tag{8-2}$$

Table 8.1 compares two models developed in this thesis in terms of conceptual aspects. Due to the reason that the database of the measurements and database of RT are not taken from the same area the parametric comparison or DME performance comparison is meaningless. Therefore in here we only provide the conceptual comparison.

Table 8.1: Comparison of the two models

RT Based Model	**Measurement Based Model**
LOS/OLOS	DDP/UDP
Based on mathematical results	Based on physical facts
Using RT results	Using UWB measurements
DME has linear relation with distance	MDME has log relation with distance
Gaussian and Exponential for OLOS	Only Gaussian for all
30 MHz – 3 GHz	50 MHz – 5 GHz

Finally we used the results of previous work [Has02] to develop a model for calculating DP power from site-specific information and using that model to calculate probability of UDP.

8.2 Future Research

There are a few directions that one might take to extend this research. The first is to enhance the DME model by providing different models for each building type

based on the collected measurement data. There might be separate models for different scenarios (e.g. OTI, ITI etc.) or perhaps it can be one model for each building. Another aspect of enhancement of the model is to examine various sets of distances and bandwidths.

The second direction is to enhance the model analytically, more specifically by finding the probability distribution function of UDME by analysis of arrival time of the next detected path. In this research we are approximated that first by an exponential distribution function and then by a positive mean Gaussian distribution.

The third research direction is to model the dynamic behavior of the DME by taking advantage of the previous state of the channel profile. This approach has already started [Hei06] but much further work is needed. In [Hei06] the UDP cases based on their causes are divided into two categories of natural UDP and shadowed UDP, a definition similar to what given in chapter 7 of this dissertation, and then a Markov model is used to incorporate the previous state of the channel profile.

The fourth one is to provide a unified model that fits to both ray-tracing and measurements. In other words combine the attributes of each of these models and create one model.

Finally one can work on improved detection algorithms to decrease the overall DME and then develop improved models for the newly drawn DME values.

Appendix A

Path-Loss Models

A.1 Fuller Laboratories – Modern Office

Fuller laboratories represent a modern office with diversified material and architecture providing for a variety of radio propagation scenarios. To develop path-loss models for the OLOS data, the ITI measurements in the Fuller laboratories are divided into three partitions: an area blocked by an elevator causing significant

degradation in the received signal strength, inter-floor open areas with significantly strong received signal power between the floors, and a blocked inter-floor data set with weak received signal power. The OTI measurements in this building show no differentiation for the data measured at different floors and the data for single and inter-floor is combined to form a multi-floor set for modeling purposes. This way we have seven path-loss scenarios for radio propagation in the Fuller laboratories, four indoor-to- indoors and three outdoor-to-indoors.

1- ITI
    a. LOS (for the open area around the Entrance in the first floor
    b. OLOS
        i. Same floor - with elevator
        ii. Inter-floor – open
        iii. Inter-floor - not open
2- OTI
    a. Multi-floor – arbitrary point
    b. Multi-floor – Entrance 1
    c. Multi-floor – Entrance 2

The following plots and equations provide the path-loss models developed for the total power and the first path for only a selected number of these scenarios, ITI LOS, ITI OLOS Inter-floor – not open, and OTI Arbitrary point. A complete list of them can be found in [IWT05].

A.1.1 Fuller PLM for ITI: LOS

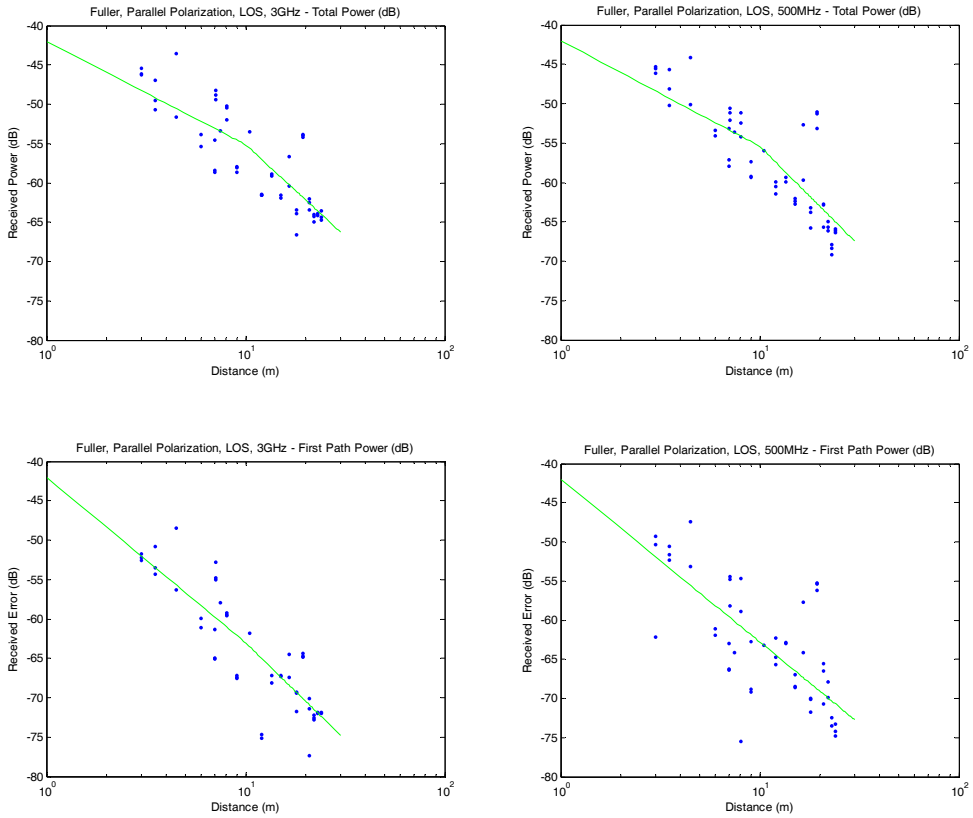

Figure A.1: PLM for Fuller, ITI – LOS

@ 3GHz

$$L_T = \begin{cases} 42 + 13\log_{10} d + \eta_T + \mu_T & d \le 10 \\ 55 + 24\log_{10}\left(d/10\right) + \eta_T + \mu_T ; d > 10 \end{cases}$$

$$\sigma_{\eta_T} = 3.4;\ m_{\mu_T} = 1.2, \sigma_{\mu_T} = 18$$

$$L_F = \begin{cases} 42 + 20\log_{10} d + \eta_F + \mu_F & d \le 10 \\ 62 + 25\log_{10}\left(d/10\right) + \eta_F + \mu_F ; d > 10 \end{cases}$$

$$\sigma_{\eta_F} = 3.5;\ m_{\mu_F} = -5.9, \sigma_{\mu_F} = 29.9$$

@ 500MHz

$$L_T = \begin{cases} 42 + 13\log_{10} d + \eta_T + \mu_T & d \le 10 \\ 55 + 25\log_{10}\left(d/10\right) + \eta_T + \mu_T ; d > 10 \end{cases}$$

$$\sigma_{\eta_T} = 3.7;\ m_{\mu_T} = 4.4, \sigma_{\mu_T} = 10$$

$$L_F = 42 + 20\log_{10} d + \eta_F + \mu_F$$

$$\sigma_{\eta_F} = 5.5;\ m_{\mu_F} = 6.5, \sigma_{\mu_F} = 18$$

A.1.2 Fuller PLM for ITI: OLOS Same Floor with Elevator

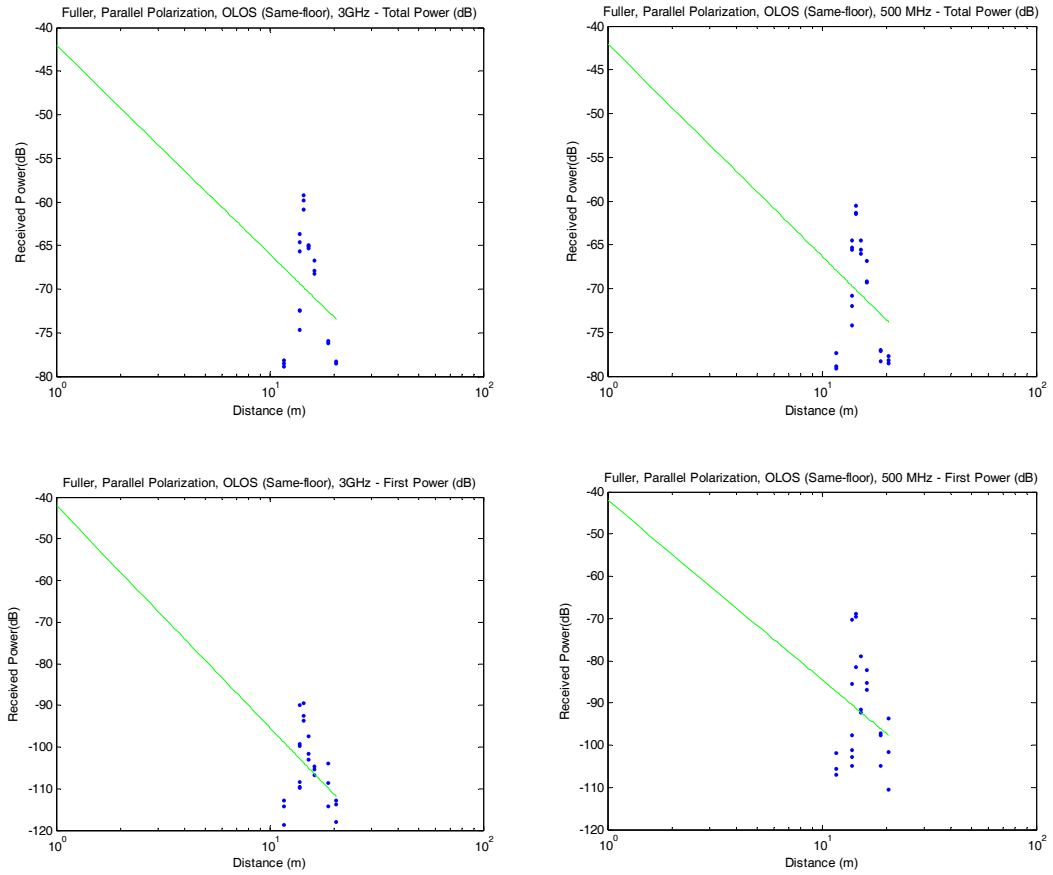

Figure A.2: PLM for Fuller, ITI – OLOS (Same Floor with Elevator)

@ 3GHz

$$L_T = 42 + 27\log_{10} d + \eta_T + \mu_T$$
$$\sigma_{\eta_T} = 10;\ m_{\mu_T} = 5.1, \sigma_{\mu_T} = 3.4$$

$$L_F = 42 + 53\log_{10} d + \eta_F + \mu_F$$
$$\sigma_{\eta_F} = 10;\ m_{\mu_F} = 5.8, \sigma_{\mu_F} = 4.6$$

@ 500MHz

$$L_T = 42 + 24\log_{10} d + \eta_T + \mu_T$$
$$\sigma_{\eta_T} = 6.3;\ m_{\mu_T} = 4.4, \sigma_{\mu_T} = 4$$

$$L_F = 42 + 42\log_{10} d + \eta_F + \mu_F$$
$$\sigma_{\eta_F} = 12;\ m_{\mu_F} = 4.8, \sigma_{\mu_F} = 9.8$$

A.1.3 Fuller PLM for ITI: OLOS Inter-Floor – Not Open

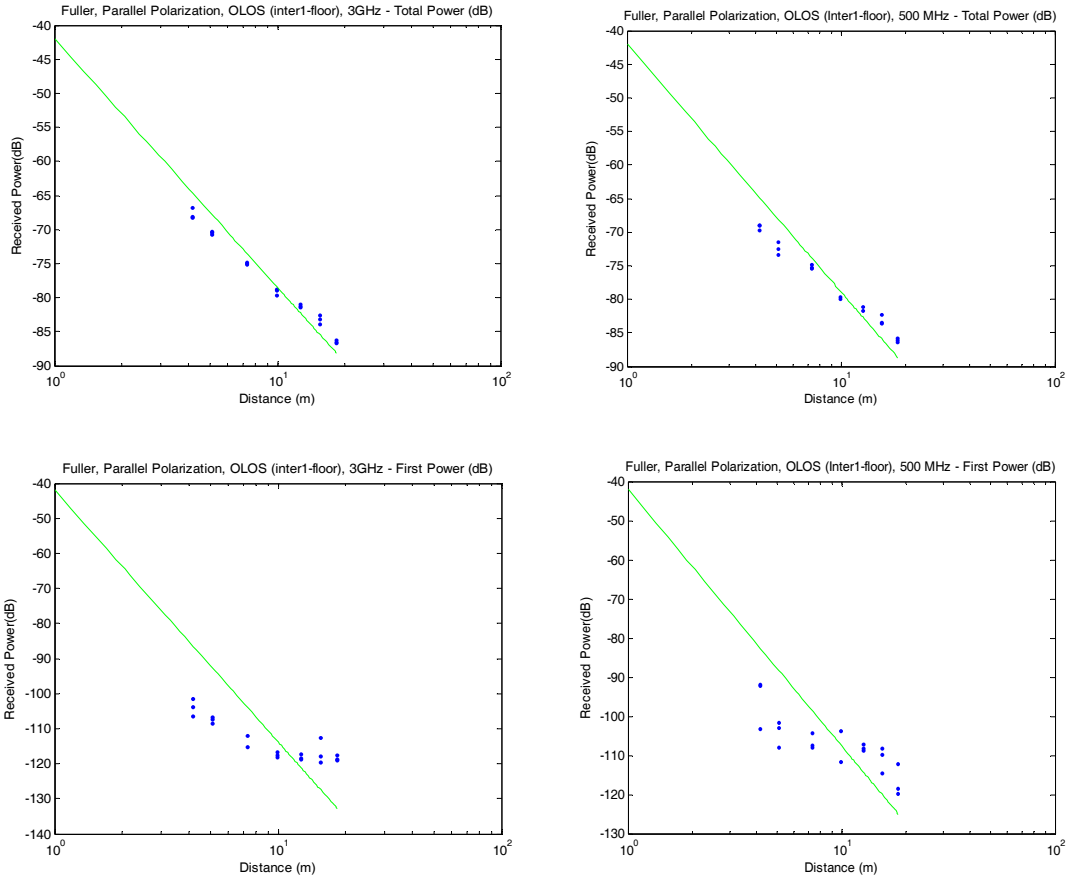

Figure A.3: PLM for Fuller, ITI – OLOS (Inter-floor, not open)

@ 3GHz

$$L_T = 42 + 36\log_{10} d + \eta_T + \mu_T$$
$$\sigma_{\eta_T} = 2.1;\ m_{\mu_T} = -1.3, \sigma_{\mu_T} = 2$$

$$L_F = 42 + 72\log_{10} d + \eta_F + \mu_F$$
$$\sigma_{\eta_F} = 11.9;\ m_{\mu_F} = -0.6, \sigma_{\mu_F} = 3.1$$

@ 500 MHz

$$L_T = 42 + 36\log_{10} d + \eta_T + \mu_T$$
$$\sigma_{\eta_T} = 2.7;\ m_{\mu_T} = -1.9, \sigma_{\mu_T} = 2.3$$

$$L_F = 42 + 65\log_{10} d + \eta_F + \mu_F$$
$$\sigma_{\eta_F} = 10.4;\ m_{\mu_F} = -2.8, \sigma_{\mu_F} = 6.7$$

A.1.4 Fuller PLM for ITI: OLOS Inter-Floor - Open

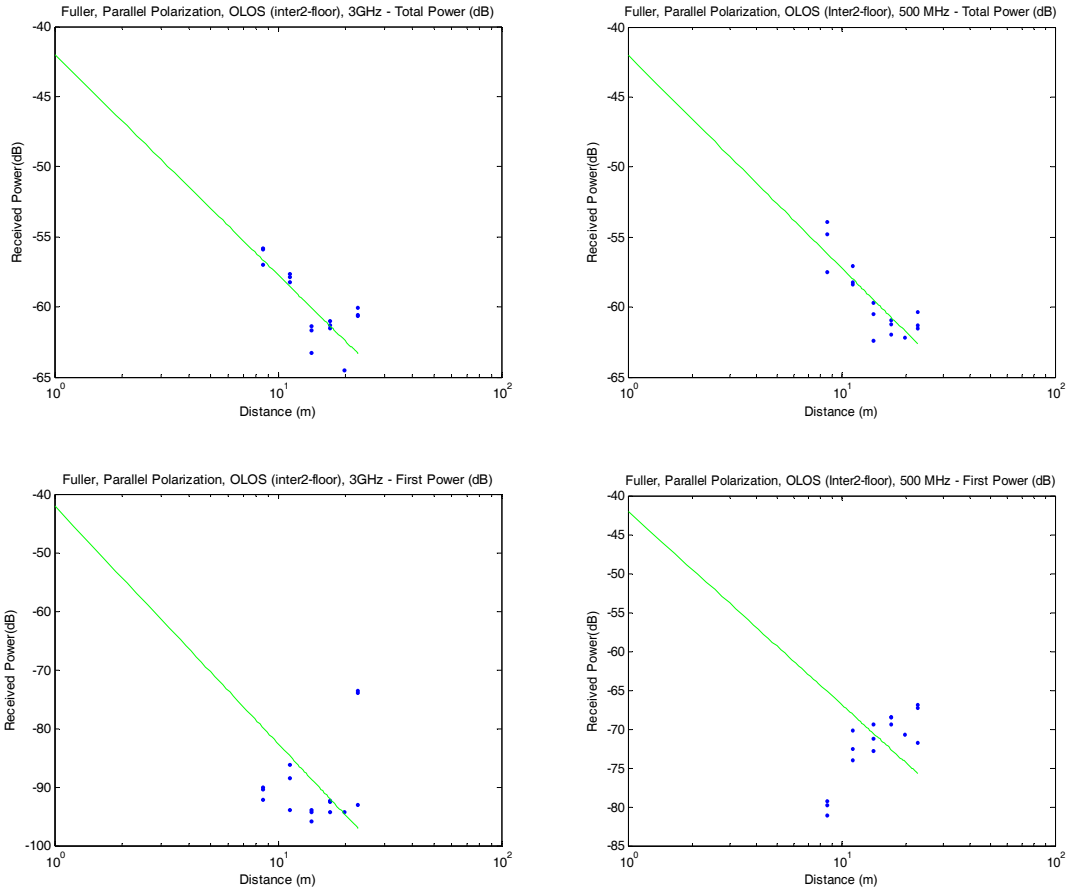

Figure A.4: PLM for Fuller, ITI – OLOS (Inter-floor, open)

@ 3GHz

$$L_T = 42 + 16\log_{10} d + \eta_T + \mu_T$$
$$\sigma_{\eta_T} = 1.8; m_{\mu_T} = 7.2, \sigma_{\mu_T} = 3.2$$

$$L_F = 42 + 40\log_{10} d + \eta_F + \mu_F$$
$$\sigma_{\eta_F} = 10;\ m_{\mu_F} = 11.8, \sigma_{\mu_F} = 5.3$$

@ 500MHz

$$L_T = 42 + 15\log_{10} d + \eta_T + \mu_T$$
$$\sigma_{\eta_T} = 1.3;\ m_{\mu_T} = 7.1, \sigma_{\mu_T} = 4.3$$

$$L_F = 42 + 25\log_{10} d + \eta_F + \mu_F$$
$$\sigma_{\eta_F} = 7.5;\ m_{\mu_F} = 9.9, \sigma_{\mu_F} = 7.6$$

A.1.5 Fuller PLM for OTI: Inter-Floor - Arbitrary Point

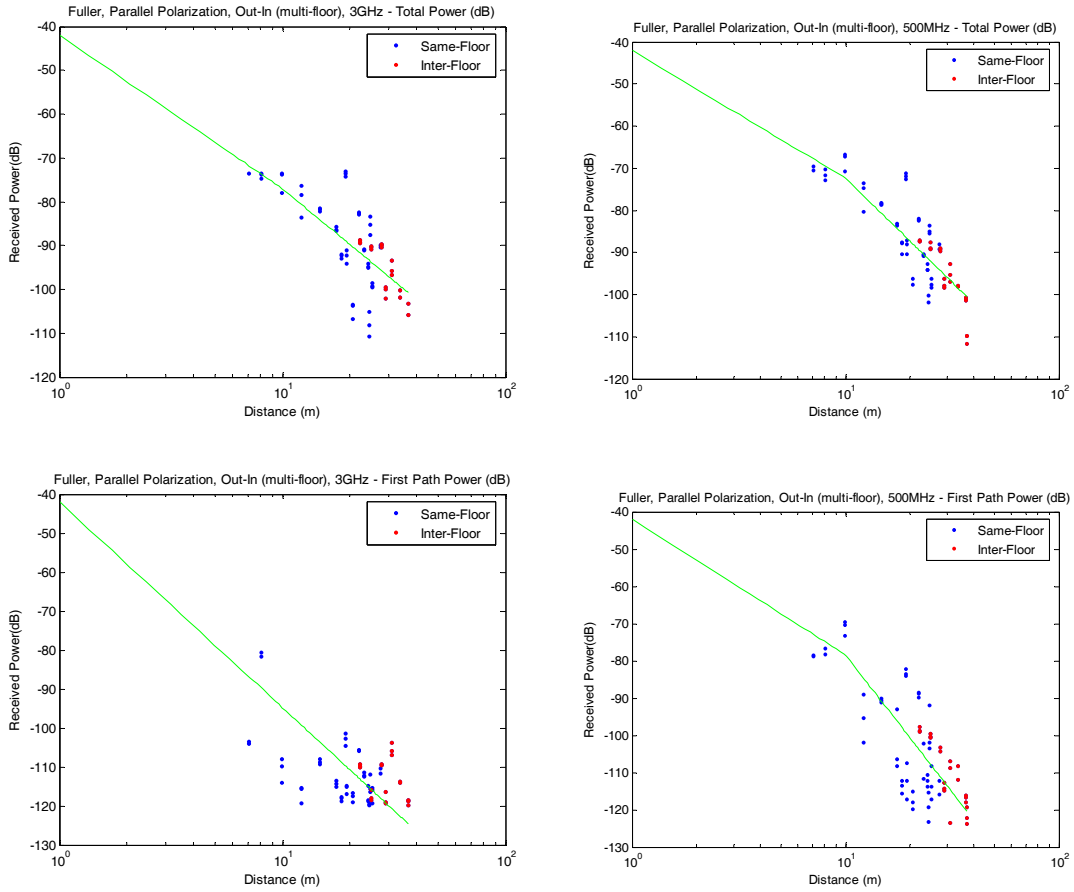

Figure A.5: PLM for Fuller, OTI –Inter-floor, Arbitrary Point

@ 3GHz

$$L_T = \begin{cases} 42 + 35\log_{10} d + \eta_T + \mu_T & d \le 10 \\ 77 + 42\log_{10}(d/10) + \eta_T + \mu_T; & d > 10 \end{cases}$$

$$\sigma_{\eta_T} = 5.1;\ m_{\mu_F} = 7.1, \sigma_{\mu_F} = 4.1$$

$$L_F = 42 + 53\log_{10} d + \eta_F + \mu_F$$

$$\sigma_{\eta_F} = 8.6;\ m_{\mu_F} = 4.3, \sigma_{\mu_F} = 7.9$$

@ 500MHz

$$L_T = \begin{cases} 42 + 30\log_{10} d + \eta_T + \mu_T & d \le 10 \\ 72 + 49\log_{10}(d/10) + \eta_T + \mu_T; & d > 10 \end{cases}$$

$$\sigma_{\eta_{T1}} = 4.7;\ m_{\mu_T} = 4.6, \sigma_{\mu_T} = 3.4$$

$$L_F = \begin{cases} 42 + 36\log_{10} d + \eta_F + \mu_F & d \le 10 \\ 78 + 58\log_{10}(d/10) + \eta_F + \mu_F; & d > 10 \end{cases}$$

$$\sigma_{\eta_F} = 8.6;\ m_{\mu_F} = 5.1, \sigma_{\mu_F} = 7.7$$

A.1.6 Fuller PLM for OTI: Inter-Floor - Entrance 1

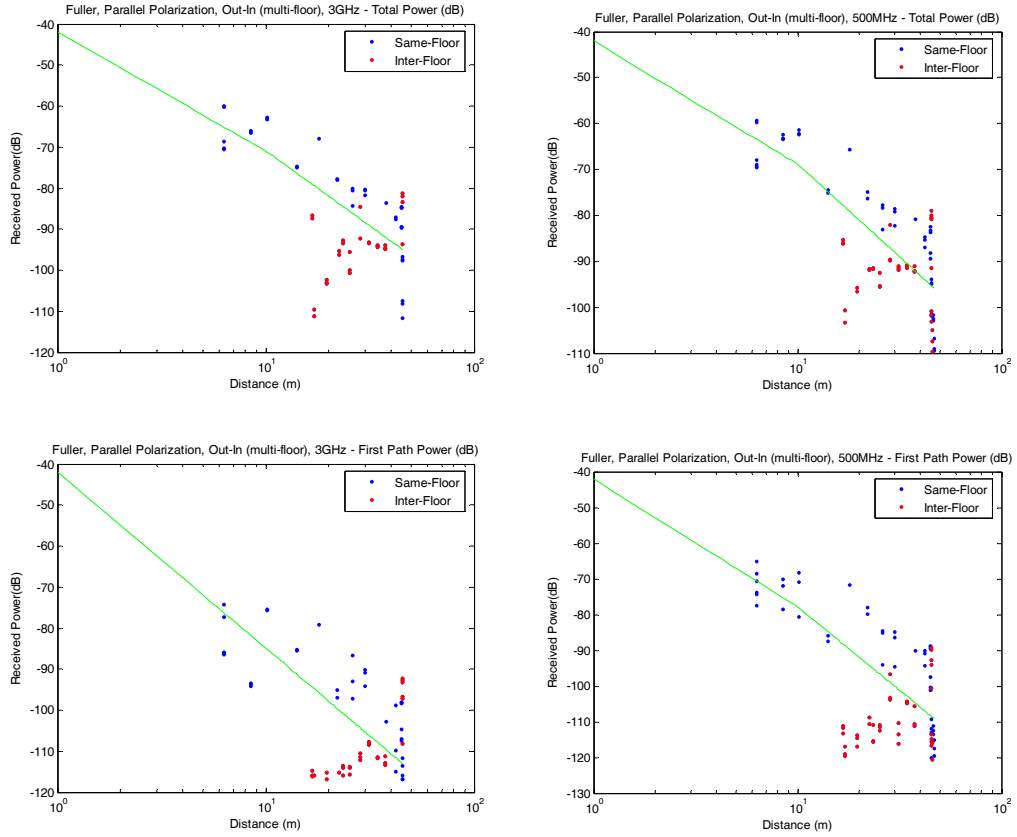

Figure A.6: PLM for Fuller, OTI –Inter-floor, Entrance 1

@ 3GHz

$$L_T = \begin{cases} 42 + 29\log_{10} d + \eta_T + \mu_T & d \le 10 \\ 71 + 42\log_{10}(d/10) + \eta_T + \mu_T; d > 10 \end{cases}$$

$\sigma_{\eta_{T1}} = 8;\ m_{\mu_T} = 12.3, \sigma_{\mu_T} = 6.5$

$$L_F = 42 + 43\log_{10} d + \eta_F + \mu_F$$

$\sigma_{\eta_F} = 11.8;\ m_{\mu_F} = 11.8, \sigma_{\mu_F} = 8.3$

@ 500MHz

$$L_T = \begin{cases} 42 + 27\log_{10} d + \eta_T + \mu_T & d \le 10 \\ 69 + 40\log_{10}(d/10) + \eta_T + \mu_T; d > 10 \end{cases}$$

$\sigma_{\eta_{T1}} = 7.9;\ m_{\mu_T} = 10.6, \sigma_{\mu_T} = 5.2$

$$L_F = \begin{cases} 42 + 36\log_{10} d + \eta_F + \mu_F & d \le 10 \\ 78 + 46\log_{10}(d/10) + \eta_F + \mu_F; d > 10 \end{cases}$$

$\sigma_{\eta_{F1}} = 10.4;\ m_{\mu_F} = 11.8, \sigma_{\mu_F} = 9.3$

A.1.7 Fuller PLM for OTI: Inter-Floor - Entrance 2

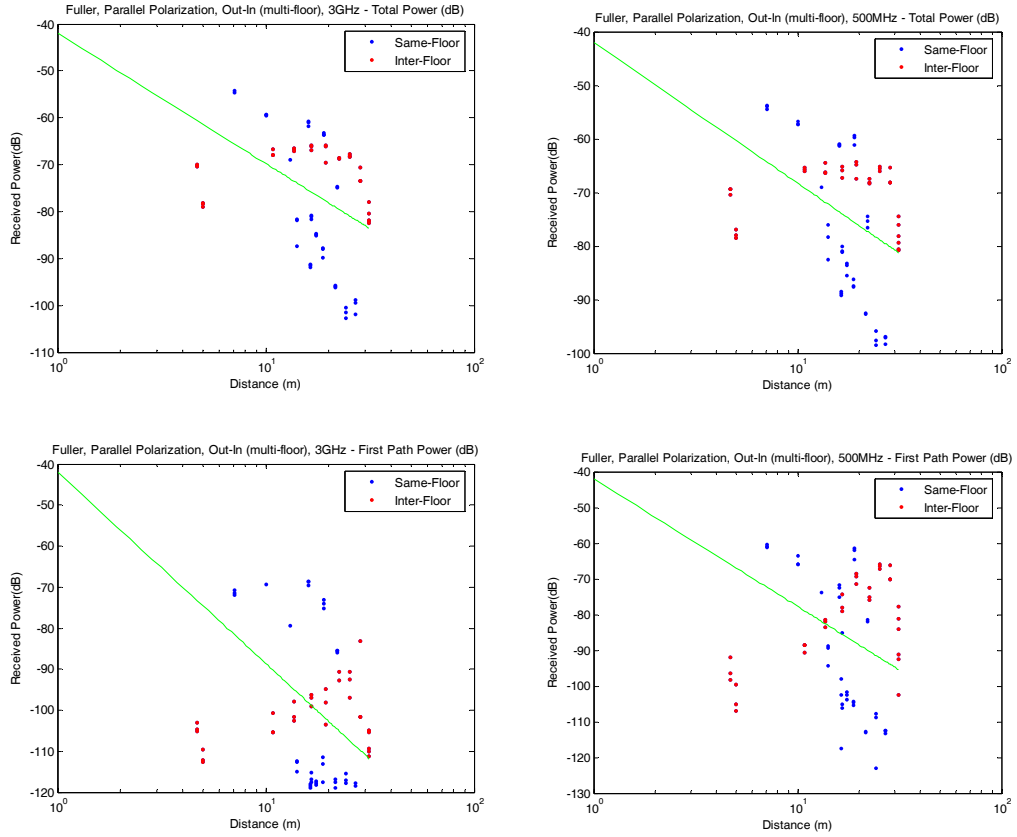

Figure A.7: PLM for Fuller, OTI –Inter-floor, Entrance 2

@ 3GHz

$$L_T = 42 + 28\log_{10} d + \eta_T + \mu_T$$
$$\sigma_{\eta_T} = 11;\ m_{\mu_T} = 6.5, \sigma_{\mu_T} = 5.6$$

$$L_F = 42 + 47\log_{10} d + \eta_F + \mu_F$$
$$\sigma_{\eta_F} = 17;\ m_{\mu_F} = 6.6, \sigma_{\mu_F} = 8.3$$

@ 500MHz

$$L_T = 42 + 26\log_{10} d + \eta_T + \mu_T$$
$$\sigma_{\eta_T} = 11.4;\ m_{\mu_T} = 6.1, \sigma_{\mu_T} = 6$$

$$L_F = 42 + 36\log_{10} d + \eta_F + \mu_F$$
$$\sigma_{\eta_F} = 18;\ m_{\mu_F} = 9.4, \sigma_{\mu_F} = 10.6$$

A.2 17 Schussler Road – Residential House

The inter-floor indoor-to-indoor propagations for the 17 Schussler Road were clearly different from the single floor propagation and two separate models are designed for these ITI cases. However, in the same building when the outdoor-to-indoor measurements are considered, similar to the Fuller, we did not observe significant difference between the single and inter-floor behavior and we combined the two sets to form a multi-floor set for the modeling. The OTI behavior in the front end of the building with wooden construction, however, shows considerable difference from the measurements in the brick constructed area in the back of the building where the kitchen is located and metallic objects such as refrigerator, washing and drying machines exists. Therefore, we have developed two separate multi-floor path-loss models for the OTI measurements at 17 Schussler Road house, two indoor-to- indoors and two outdoor-to-indoor.

1- ITI
    a. OLOS – same floor
    b. OLOS – inter-floors
2- OTI
    a. Multi-floor – area 1 (wooden)
    b. Multi-floor – area 2 (bricks)

The following plots and equations provide the PLM developed for the total power and the first path for only a selected number of these scenarios, OLOS – same floor, and Multi floor – area 1 (wooden). A complete list of them can be found in [IWT05].

A.2.1 Schussler PLM for ITI: OLOS Same Floor

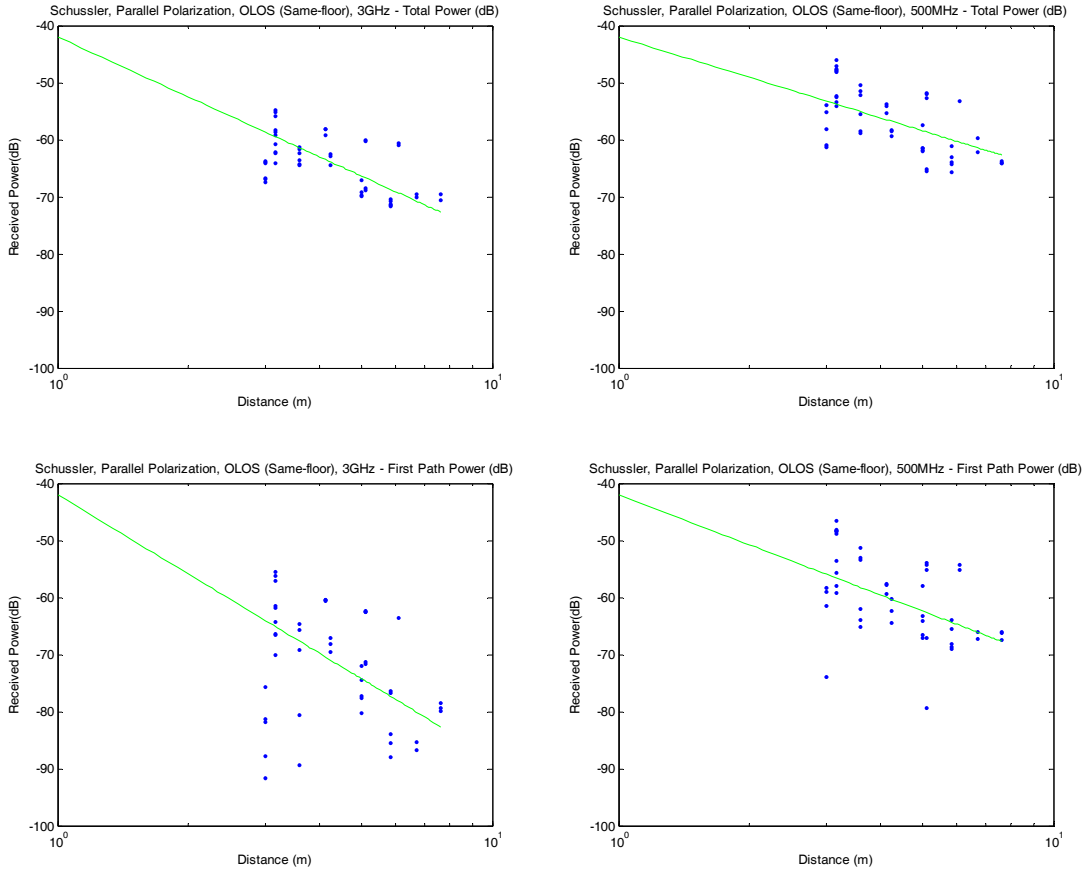

Figure A.8: PLM for Schussler, ITI – OLOS, Same-floor

@ 3GHz

$$L_T = 42 + 27\log_{10} d + \eta_T + \mu_T$$
$$\sigma_{\eta_T} = 3.9 \qquad m_{\mu_T} = 7.4, \sigma_{\mu_T} = 2.2$$

$$L_F = 42 + 39\log_{10} d + \eta_F + \mu_F$$
$$\sigma_{\eta_F} = 9.2 \qquad m_{\mu_F} = 9.5, \sigma_{\mu_F} = 7.9$$

@ 500MHz

$$L_T = 42 + 23\log_{10} d + \eta_T + \mu_T$$
$$\sigma_{\eta_T} = 4.4 \qquad m_{\mu_T} = 7.9, \sigma_{\mu_T} = 3.3$$

$$L_F = 42 + 29\log_{10} d + \eta_F + \mu_F$$
$$\sigma_{\eta_F} = 6.8 \qquad m_{\mu_F} = 10.3, \sigma_{\mu_F} = 6.7$$

A.2.2 Schussler PLM for ITI: OLOS Inter-Floors

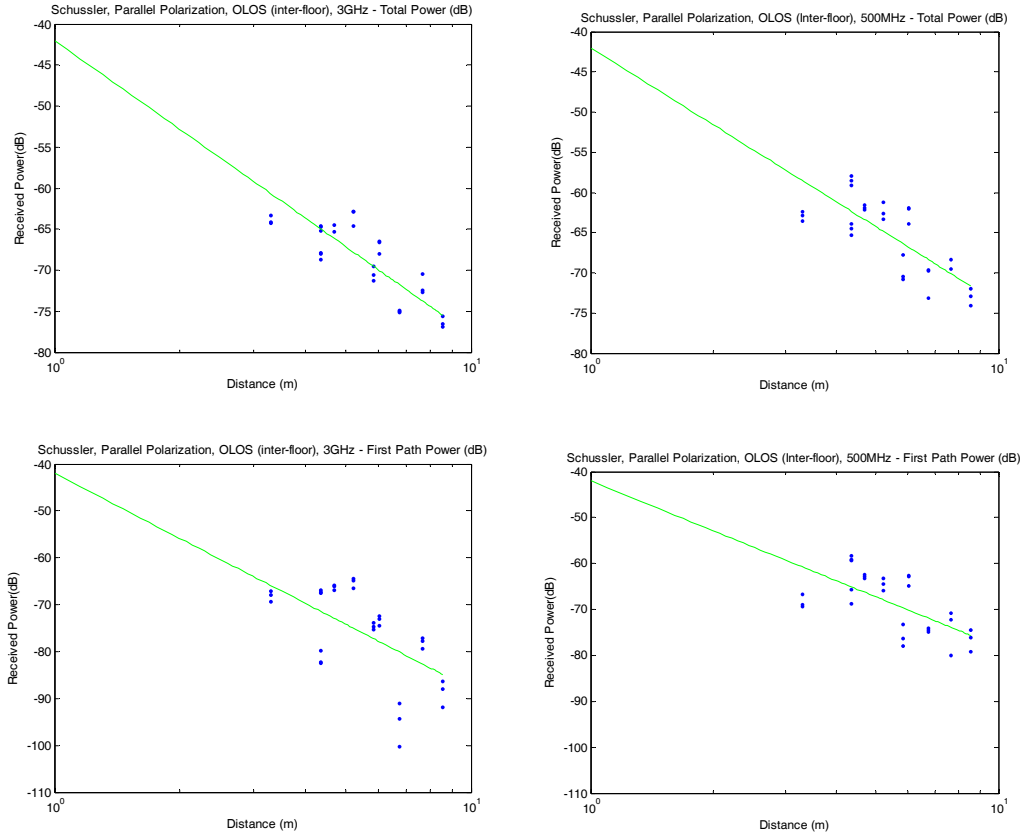

Figure A.9: PLM for Schussler, ITI – OLOS, Inter-floor

@ 3GHz

$$L_T = 42 + 36\log_{10} d + \eta_T + \mu_T$$
$$\sigma_{\eta_T} = 2.7 \qquad m_{\mu_T} = 2.4, \sigma_{\mu_T} = 1.6$$

$$L_F = 42 + 46\log_{10} d + \eta_F + \mu_F$$
$$\sigma_{\eta_F} = 7.7 \qquad m_{\mu_F} = 4.3, \sigma_{\mu_F} = 4.7$$

@ 500MHz

$$L_T = 42 + 32\log_{10} d + \eta_T + \mu_T$$
$$\sigma_{\eta_T} = 3.1 \qquad m_{\mu_T} = 3.3, \sigma_{\mu_T} = 3.2$$

$$L_F = 42 + 36\log_{10} d + \eta_F + \mu_F$$
$$\sigma_{\eta_F} = 5 \qquad m_{\mu_F} = 6.9, \sigma_{\mu_F} = 6.9$$

A.2.3 Schussler PLM for OTI: Multi-Floor –Area 1 (Wooden)

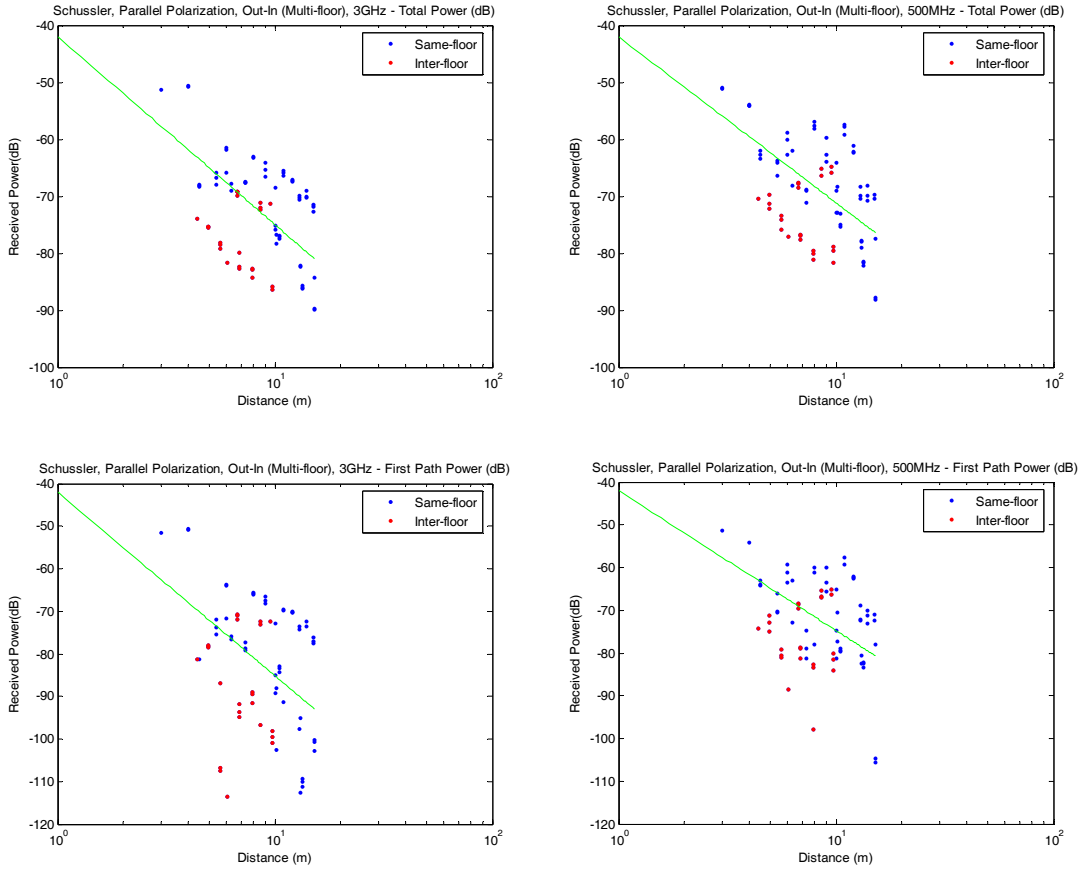

Figure A.10: PLM for Schussler, OTI – Multi-floor, Area 1 (Wooden)

@ 3GHz

$$L_T = 42 + 33\log_{10} d + \eta_T + \mu_T$$
$$\sigma_{\eta_T} = 8 \qquad m_{\mu_T} = 6.5, \sigma_{\mu_T} = 3.5$$

$$L_F = 42 + 43\log_{10} d + \eta_F + \mu_F$$
$$\sigma_{\eta_F} = 14 \qquad m_{\mu_F} = 8.9, \sigma_{\mu_F} = 11.7$$

@ 500MHz

$$L_T = 42 + 29\log_{10} d + \eta_T + \mu_T$$
$$\sigma_{\eta_T} = 7.6 \qquad m_{\mu_T} = 6.4, \sigma_{\mu_T} = 4.7$$

$$L_F = 42 + 33\log_{10} d + \eta_F + \mu_F$$
$$\sigma_{\eta_F} = 10 \qquad m_{\mu_F} = 7.2, \sigma_{\mu_F} = 7.8$$

A.2.4 Schussler PLM for OTI: Multi-Floor –Area 2 (Bricks)

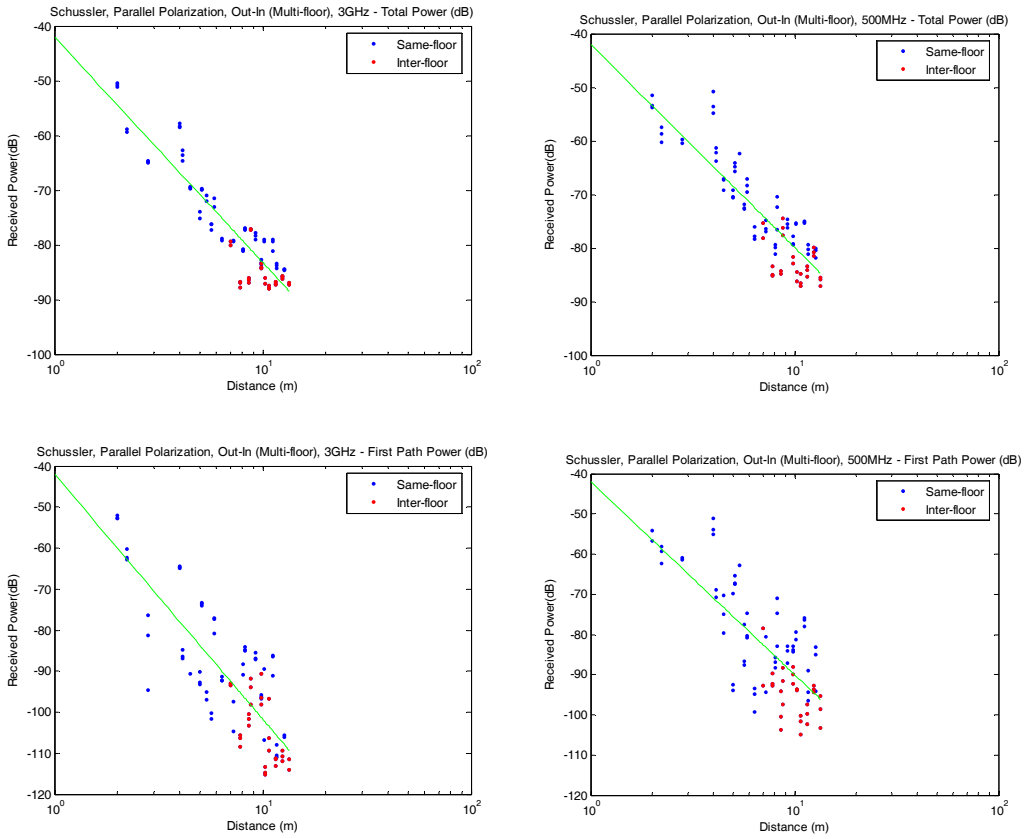

Figure A.11: PLM for Schussler, OTI – Multi-floor, Area 2 (Bricks)

@ 3GHz

$$L_T = 42 + 41\log_{10} d + \eta_T + \mu_T$$
$$\sigma_{\eta_T} = 3.7 \qquad m_{\mu_T} = 5.3, \sigma_{\mu_T} = 1.8$$

$$L_F = 42 + 60\log_{10} d + \eta_F + \mu_F$$
$$\sigma_{\eta_F} = 9.2 \qquad m_{\mu_F} = 6.7, \sigma_{\mu_F} = 8.4$$

@ 500MHz

$$L_T = 42 + 38\log_{10} d + \eta_T + \mu_T$$
$$\sigma_{\eta_T} = 4.5 \qquad m_{\mu_T} = 5.4, \sigma_{\mu_T} = 3.1$$

$$L_F = 42 + 48\log_{10} d + \eta_F + \mu_F$$
$$\sigma_{\eta_F} = 8.8 \qquad m_{\mu_F} = 5.6, \sigma_{\mu_F} = 8.9$$

A.3 Norton Company– Manufacturing Floor

Norton Company is the largest building among all the sites considered in this campaign and its interior includes a huge open area with variety of machinery providing for different LOS scenarios. Also, the flat roof of this building allowed us to take roof-to-indoor measurements. The indoor-to-indoor measurements for the LOS condition allowed us two scenarios taken in two areas, one along a long pathway and the other, crowded with machinery. The openness of building does not allow sufficient OLOS measurements for meaningful statistical modeling.

The manufacturing floor at the Norton Company is a single floor building with variety of LOS propagation scenarios. We developed two LOS path-loss models for this building. The first LOS path-loss model represents an open area with crowded machinery and other LOS path-loss model describes an open area in a long pathway without much of metallic machinery. The OTI models for the Norton Company include two models for the cases where the transmitter is located close and away from the entrance of the building as well as a model for propagation from the roof. The measurements from the roof show two distinct behaviors for the areas under a window and the area with no window.

1- ITI
    a. LOS: Open area with machinery
    b. LOS: Straight walkway
2- OTI
    a. Single-floor – Entrance
    b. Single-floor – Arbitrary point
    c. Multi-floor – Roof

The following plots provide the PLMs developed for the total power and the first path for all of these scenarios.

A.3.1 Norton PLM for ITI: LOS (Open area with Machinery)

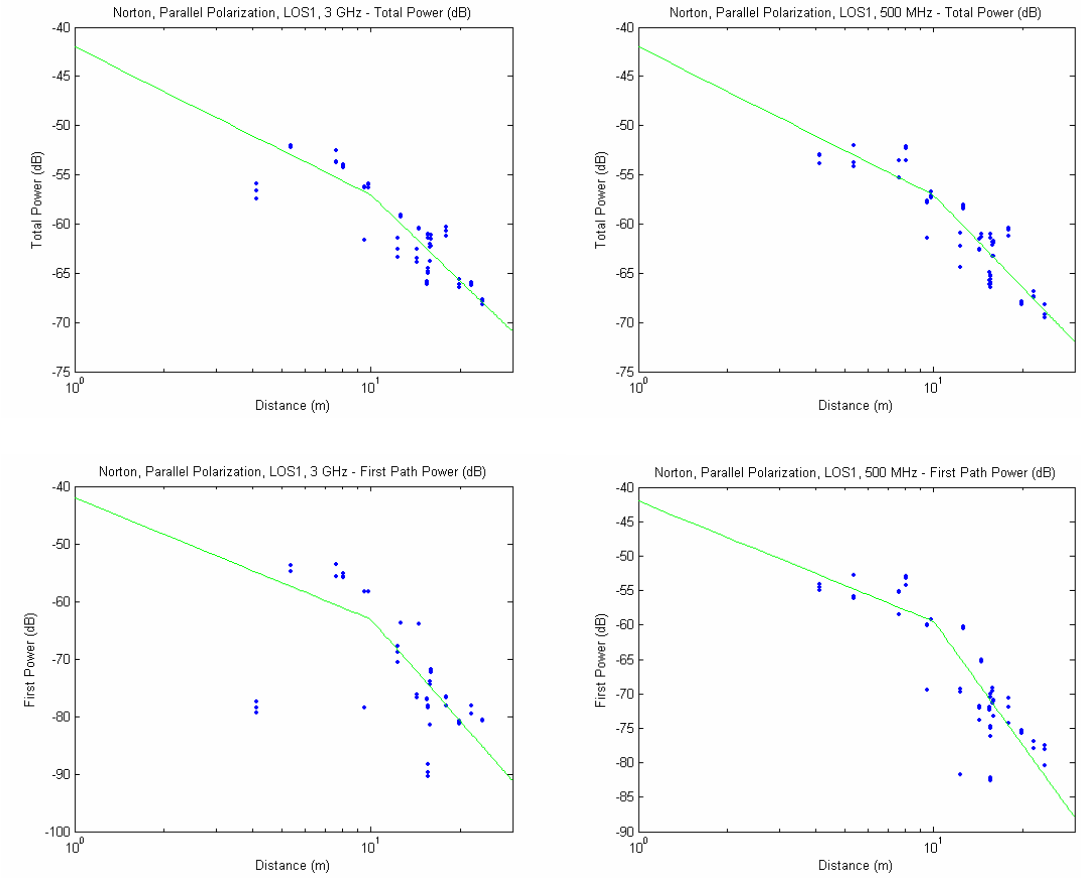

Figure A.12: PLM for Norton, ITI – LOS (Open area with Machinery)

@ 3GHz

$$L_T = \begin{cases} 42 + 15\log_{10} d + \eta_T + \mu_T & d \le 10 \\ 57 + 29\log_{10}(d/10) + \eta_T + \mu_T; d > 10 \end{cases}$$

$$\sigma_{\eta_{T1}} = 2.4;\ m_{\mu_T} = 4.9, \sigma_{\mu_T} = 1.8$$

@ 500MHz

$$L_T = \begin{cases} 42 + 15\log_{10} d + \eta_T + \mu_T & d \le 10 \\ 57 + 31\log_{10}(d/10) + \eta_T + \mu_T; d > 10 \end{cases}$$

$$\sigma_{\eta_{T1}} = 2.1;\ m_{\mu_T} = 5.2, \sigma_{\mu_T} = 2.5$$

$$L_F = \begin{cases} 42 + 21\log_{10} d + \eta_F + \mu_F & d \le 10 \\ 63 + 59\log_{10}\left(d/10\right) + \eta_F + \mu_F; d > 10 \end{cases}$$

$\sigma_{\eta_{F1}} = 5.7;\ m_{\mu_F} = 13.8, \sigma_{\mu_F} = 8.4$

$$L_F = \begin{cases} 42 + 17\log_{10} d + \eta_F + \mu_F & d \le 10 \\ 59 + 59\log_{10}\left(d/10\right) + \eta_F + \mu_F; d > 10 \end{cases}$$

$\sigma_{\eta_{F1}} = 4.1;\ m_{\mu_F} = 13.8, \sigma_{\mu_F} = 7.2$

A.3.2 Norton PLM for ITI: LOS (straight walkway)

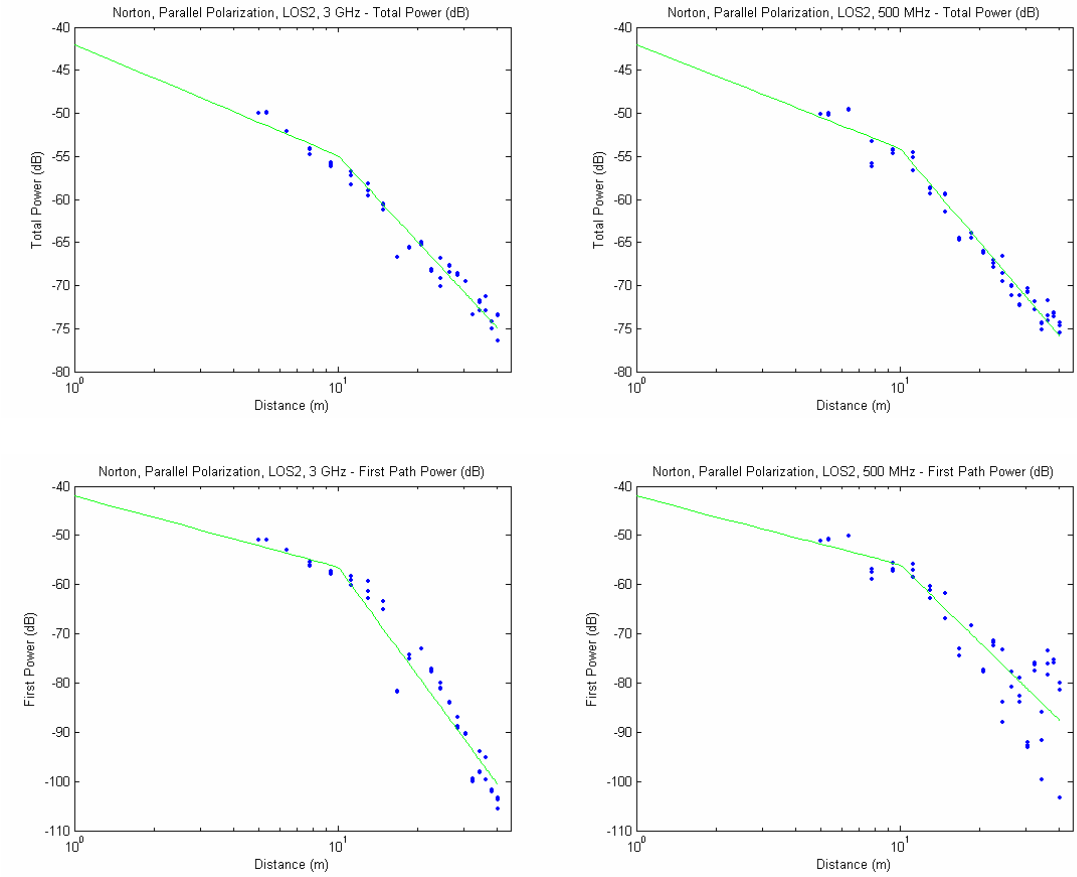

Figure A.13: PLM for Norton, ITI – LOS (Straight Walkway)

@ 3GHz

$$L_T = \begin{cases} 42 + 13\log_{10} d + \eta_T + \mu_T & d \le 10 \\ 55 + 33\log_{10}(d/10) + \eta_T + \mu_T; & d > 10 \end{cases}$$

$\sigma_{\eta_{T1}} = 1.3;\ m_{\mu_T} = 6.7, \sigma_{\mu_T} = 2.1$

$$L_F = \begin{cases} 42 + 14\log_{10} d + \eta_F + \mu_F & d \le 10 \\ 56 + 73\log_{10}(d/10) + \eta_F + \mu_F; & d > 10 \end{cases}$$

$\sigma_{\eta_{F1}} = 3.1;\ m_{\mu_F} = 11.4, \sigma_{\mu_F} = 6.4$

@ 500MHz

$$L_T = \begin{cases} 42 + 12\log_{10} d + \eta_T + \mu_T & d \le 10 \\ 53 + 36\log_{10}(d/10) + \eta_T + \mu_T; & d > 10 \end{cases}$$

$\sigma_{\eta_{T1}} = 1.4;\ m_{\mu_T} = 7.6, \sigma_{\mu_T} = 2.7$

$$L_F = \begin{cases} 42 + 14\log_{10} d + \eta_F + \mu_F & d \le 10 \\ 56 + 52\log_{10}(d/10) + \eta_F + \mu_F; & d > 10 \end{cases}$$

$\sigma_{\eta_{F1}} = 4.6;\ m_{\mu_F} = 10.2, \sigma_{\mu_F} = 8.9$

A.3.3 Norton PLM for OTI: Entrance

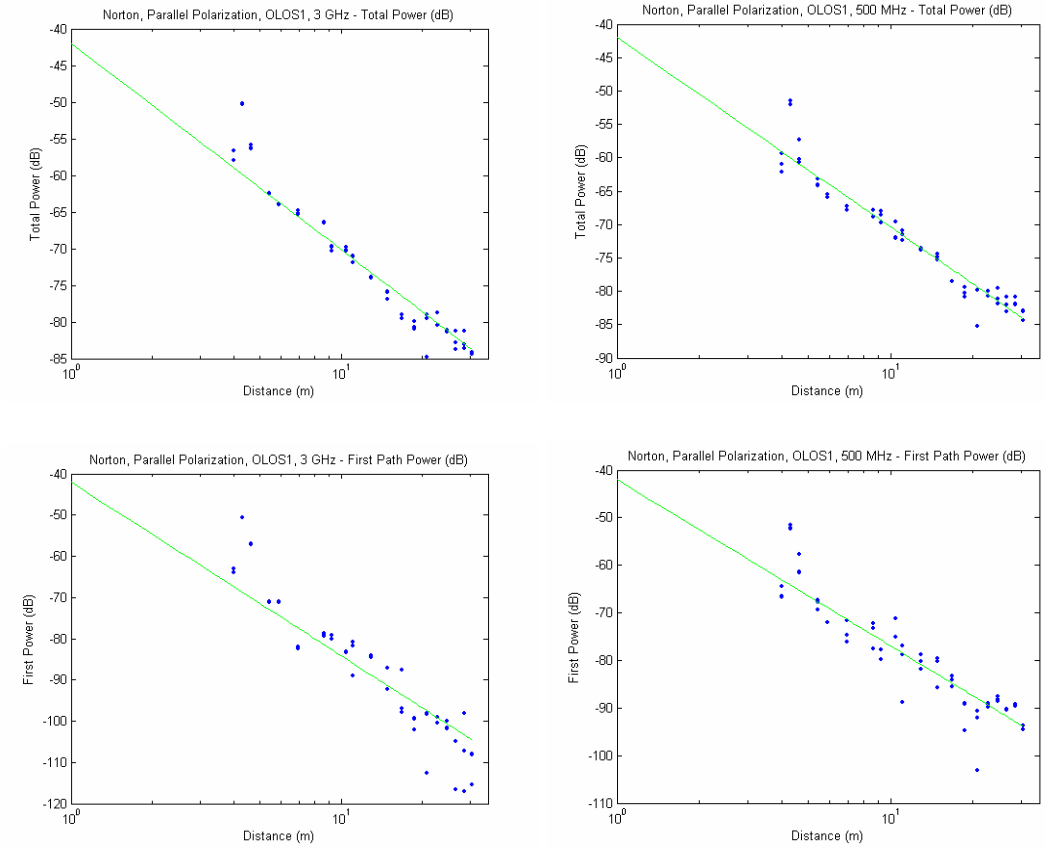

Figure A.14: PLM for Norton, OTI – Entrance

@ 3GHz

$$L_T = 42 + 28\log_{10} d + \eta_T + \mu_T$$
$$\sigma_{\eta T} = 2.8;\ m_{\mu_T} = 5.9, \sigma_{\mu_T} = 2.9$$

$$L_F = 42 + 42\log_{10} d + \eta_F + \mu_F$$
$$\sigma_{\eta_F} = 6.8;\ m_{\mu_F} = 14.8, \sigma_{\mu_F} = 8.0$$

@ 500MHz

$$L_T = 42 + 28\log_{10} d + \eta_T + \mu_T$$
$$\sigma_{\eta T} = 2.4;\ m_{\mu_T} = 5.2, \sigma_{\mu_T} = 3.3$$

$$L_F = 42 + 35\log_{10} d + \eta_F + \mu_F$$
$$\sigma_{\eta_F} = 4.7;\ m_{\mu_F} = 10.1, \sigma_{\mu_F} = 6.6$$

A.3.4 Norton PLM for OTI: Arbitrary Point

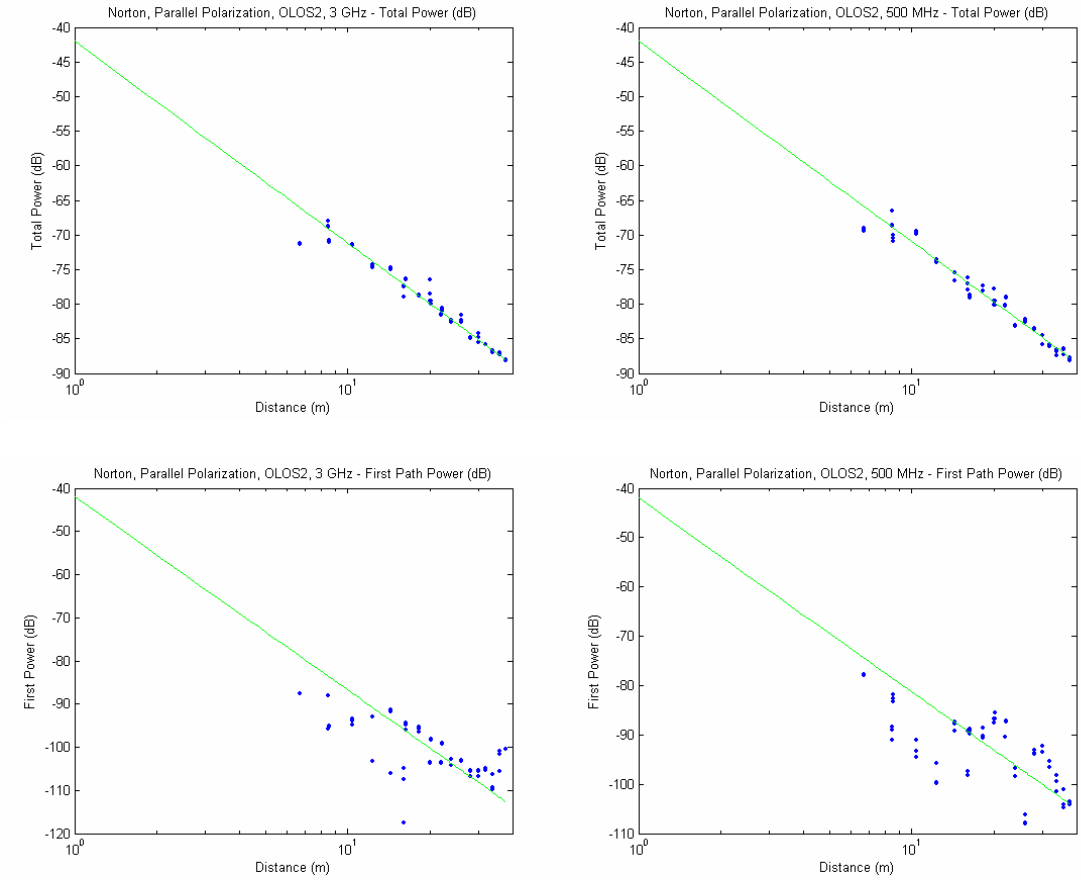

Figure A.15: PLM for Norton, OTI – Arbitrary Point

@ 3GHz

$$L_T = 42 + 29\log_{10} d + \eta_T + \mu_T$$
$$\sigma_{\eta T} = 1.4;\ m_{\mu_T} = 5.8, \sigma_{\mu_T} = 1.9$$

$$L_F = 42 + 45\log_{10} d + \eta_F + \mu_F$$
$$\sigma_{\eta_F} = 6.7;\ m_{\mu_F} = 12.1, \sigma_{\mu_F} = 4.9$$

@ 500MHz

$$L_T = 42 + 29\log_{10} d + \eta_T + \mu_T$$
$$\sigma_{\eta T} = 1.3;\ m_{\mu_T} = 5.5, \sigma_{\mu_T} = 2.3$$

$$L_F = 42 + 39\log_{10} d + \eta_F + \mu_F$$
$$\sigma_{\eta_F} = 6.5;\ m_{\mu_F} = 10.1, \sigma_{\mu_F} = 8.4$$

A.3.5 Norton PLM for OTI: Roof

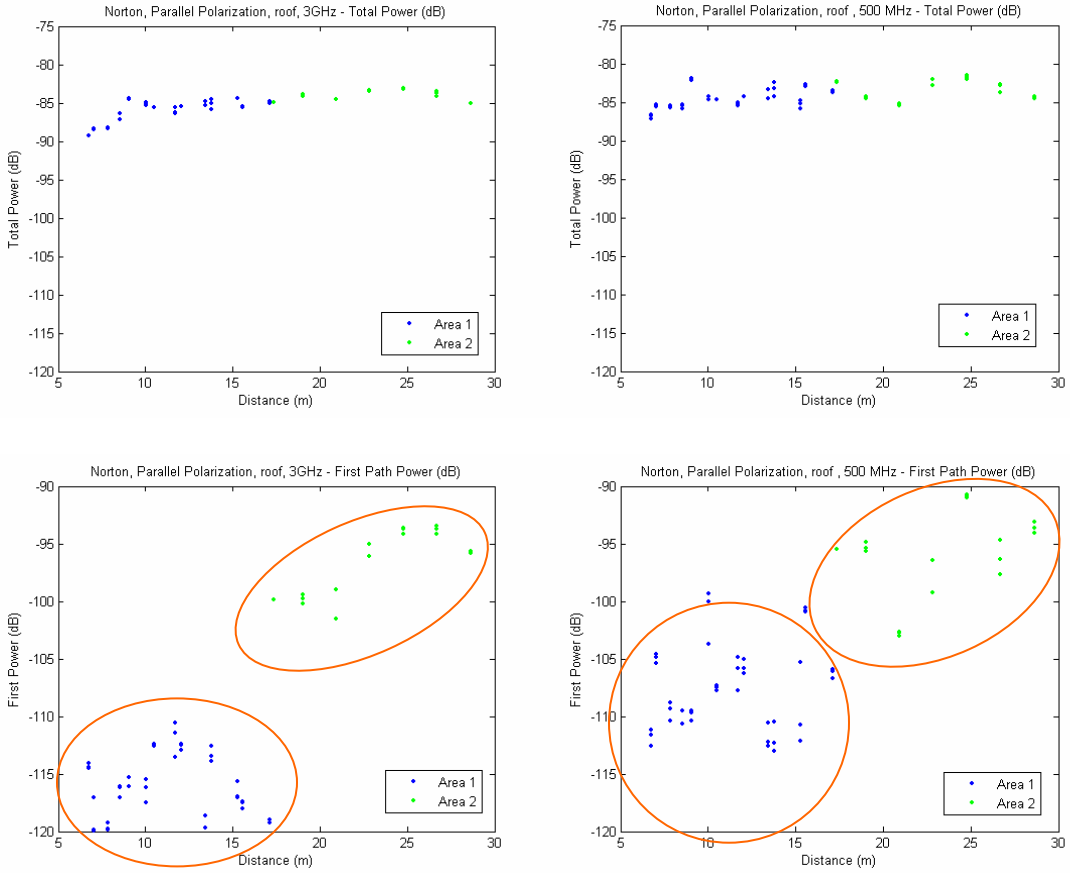

Figure A.16: PLM for Norton, OTI – Roof

The total received power in these measurements showed no sensitivity to the distance and the received power was around -85dBm for all points. The first path power, however, formed two clusters. One of this clusters, is around -95dBm for which there was a window on top of the ceiling facilitating propagation of the signal to the inside of the building. The other cluster provides around 20dB weaker first path signal strengths. One explanation for this behavior is the structure of the roof. There are glass windows throughout the entire roof. As it happened, the part of the measurements that

were under the glass window received stronger signal than the ones that didn't have access to the window. Figure 5.11 shows the site of the measurements. As you can see in the top right of the figure, there is a strip of glass windows lining up along side the measurements. As a result, the portions of the measurements that have stronger first path power lie underneath it and receive greater signal with the earlier ones.

Figure A.17: Norton Roof Measurements. (The glass windows on the roof contribute to stronger first path power to those measurements down the aisle.)

A.4 Atwater Kent – Old Office

The roof-to-indoor measurements in Atwater Kent Laboratory showed a distinct differentiation in different rooms due to their window structure and location of the measurements relative to windows. In addition, the behavior of the roof measurements was distinctly different from other OTI and ITI scenarios. We partitioned the roof measurements in the Atwater Kent Laboratory into four different scenarios for path-loss modeling. The first model is developed for the behavior in the corridors where we have no direct window to the outside. The next three models are for different size rooms with windows to outside. These models are for the smaller AK 311 and AK 312 rooms and AK 320, the larger CWINS laboratory, in which the behavior of location close and away from the window are substantially different. Therefore, we have four sets of path-loss models developed for the roof of the Atwater Kent Laboratory, four indoor-to-indoors and three outdoor-to-indoors.

1- Roof-to-indoor (***RTI***) – Corridors
2- Roof-to-indoor (***RTI***) – AK 311
3- Roof-to-indoor (***RTI***) – AK 312
4- Roof-to-indoor (***RTI***) – AK 320

The following plots provide the PLM developed for the total power and the first path for only AK320 scenario. A complete list can be found in [IWT05].

A.4.1 AK – Roof PLM for RTI: Corridors

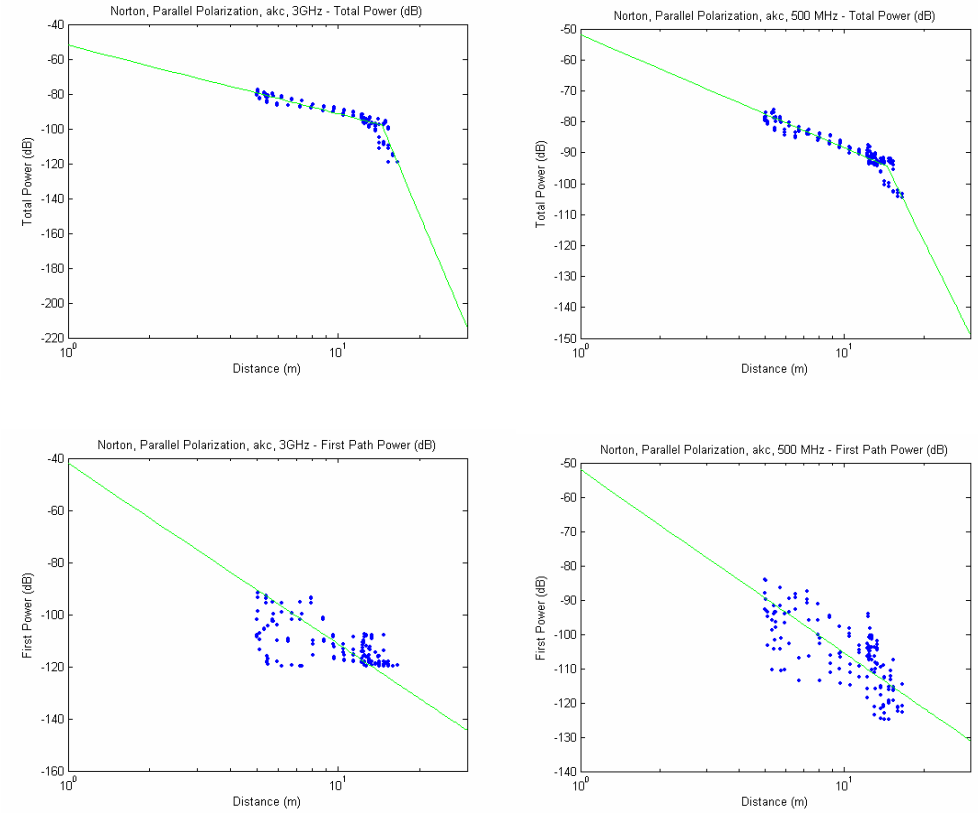

Figure A.18: PLM for AK, RTI - Corridors

@ 3GHz

$$L_T = \begin{cases} 52 + 40\log_{10} d + \eta_T + \mu_T & d \le 14.5 \\ 98 + 386\log_{10}\left(d/14.5\right) + \eta_T + \mu_T; d > 14.5 \end{cases}$$

$\sigma_{\eta_{T1}} = 4.3;\ m_{\mu_T} = 0.5, \sigma_{\mu_T} = 3.9$

$L_F = 52 + 59\log_{10} d + \eta_F + \mu_F$

$\sigma_{\eta_F} = 7.8;\ m_{\mu_F} = 0.6, \sigma_{\mu_F} = 8.3$

@ 500MHz

$$L_T = \begin{cases} 52 + 36\log_{10} d + \eta_T + \mu_T & d \le 14.5 \\ 98 + 172\log_{10}\left(d/14.5\right) + \eta_T + \mu_T; d > 14.5 \end{cases}$$

$\sigma_{\eta_{T1}} = 2.4;\ m_{\mu_T} = 1.0, \sigma_{\mu_T} = 1.6$

$L_F = 52 + 54\log_{10} d + \eta_F + \mu_F$

$\sigma_{\eta_F} = 7.4;\ m_{\mu_F} = 0.2, \sigma_{\mu_F} = 8.3$

Note: the last points on the right hand side belong to the last segment of the corridor with minimal received signal strength and the model for that part is not reliable.

A.4.2 AK – Roof PLM for RTI: AK311

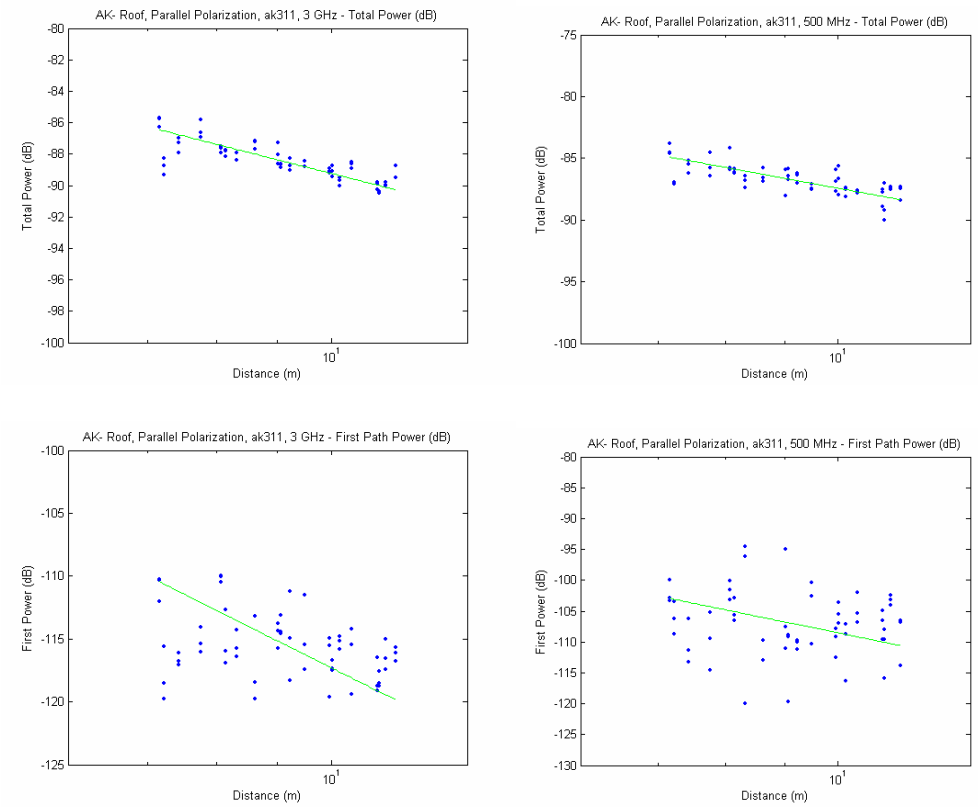

Figure A.19: PLM for AK, RTI – AK311

@ 3GHz

$$L_T = 42 + 19\log_{10} d + L_R + \eta_T + \mu_T$$
$$\sigma_{\eta T} = 0.8;\ m_{\mu_T} = 1.8, \sigma_{\mu_T} = 0.9$$
$$L_R = 28$$

$$L_F = 42 + 47\log_{10} d + L_R + \eta_F + \mu_F$$
$$\sigma_{\eta_F} = 3.2;\ m_{\mu_F} = -0.6, \sigma_{\mu_F} = 4.5$$
$$L_R = 28$$

@ 500MHz

$$L_T = 42 + 17\log_{10} d + L_R + \eta_T + \mu_T$$
$$\sigma_{\eta T} = 0.9;\ m_{\mu_T} = 1.8, \sigma_{\mu_T} = 1.3$$
$$L_R = 28$$

$$L_F = 42 + 39\log_{10} d + L_R + \eta_F + \mu_F$$
$$\sigma_{\eta_F} = 5.5;\ m_{\mu_F} = -0.8, \sigma_{\mu_F} = 7.6$$
$$L_R = 28$$

Note: The low value of the distance power gradient for the total received power illustrates the fact that the existence of a window has substantial effect on the behavior of the received signal power.

A.4.3 AK – Roof PLM for RTI: AK312

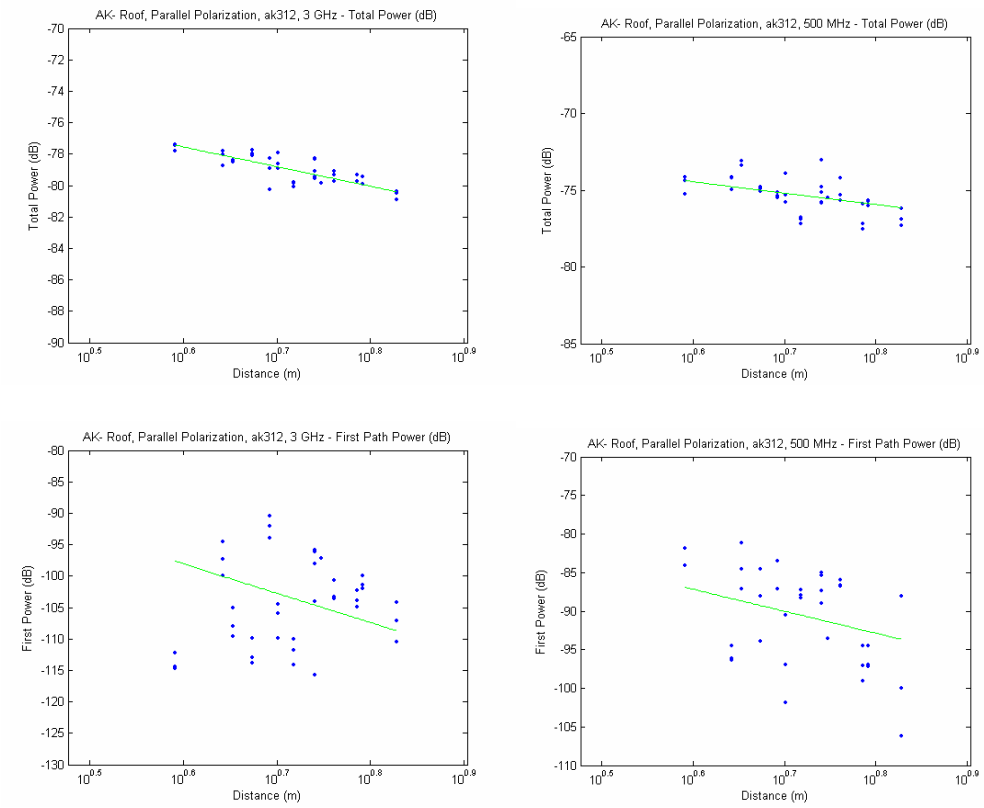

Figure A.20: PLM for AK, RTI – AK312

@ 3GHz

$$L_T = 42 + 13\log_{10} d + L_R + \eta_T + \mu_T$$
$$\sigma_{\eta T} = 0.53;\ m_{\mu_T} = 0.4, \sigma_{\mu_T} = 1.4$$
$$L_R = 28$$

$$L_F = 42 + 47\log_{10} d + L_R + \eta_F + \mu_F$$
$$\sigma_{\eta_F} = 8.1;\ m_{\mu_F} = 0.1, \sigma_{\mu_F} = 8.7$$
$$L_R = 28$$

@ 500MHz

$$L_T = 42 + 7\log_{10} d + L_R + \eta_T + \mu_T$$
$$\sigma_{\eta T} = 0.9;\ m_{\mu_T} = 1; .7, \sigma_{\mu_T} = 1.4$$
$$L_R = 28$$

$$L_F = 42 + 29\log_{10} d + L_R + \eta_F + \mu_F$$
$$\sigma_{\eta_F} = 5.3;\ m_{\mu_F} = 1.4, \sigma_{\mu_F} = 10$$
$$L_R = 28$$

A.4.4 AK – Roof PLM for RTI: AK320

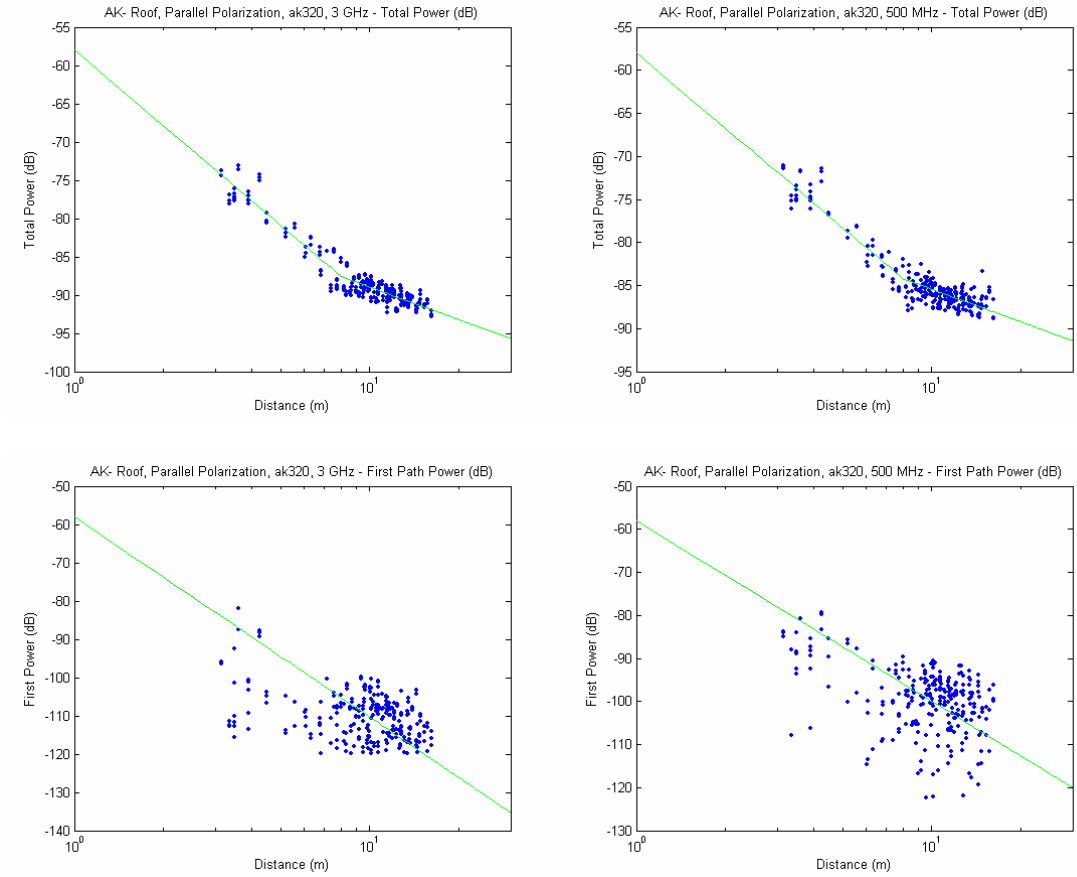

Figure A.21: PLM for AK, OTI – Roof (AK320)

@ 3GHz

$$L_T = \begin{cases} 42 + 33\log_{10} d + L_R + \eta_T + \mu_T & d \le 8 \\ 88 + 14\log_{10}(d/8) + \eta_T + \mu_T; & d > 8 \end{cases}$$

$\sigma_{\eta_{T1}} = 1.3;\ m_{\mu_T} = 0.2, \sigma_{\mu_T} = 3.6$

$L_R = 16$

$L_F = 42 + 52\log_{10} d + L_R + \eta_F + \mu_F$

$\sigma_{\eta_F} = 8.4;\ m_{\mu_F} = 0.2, \sigma_{\mu_F} = 9.5$

$L_R = 16$

@ 500MHz

$$L_T = \begin{cases} 42 + 29\log_{10} d + L_R + \eta_T + \mu_T & d \le 8 \\ 88 + 13\log_{10}(d/8) + \eta_T + \mu_T; & d > 8 \end{cases}$$

$\sigma_{\eta_{T1}} = 8.1;\ m_{\mu_T} = 0.6, \sigma_{\mu_T} = 1.2$

$L_R = 16$

$L_F = 42 + 42\log_{10} d + L_R + \eta_F + \mu_F$

$\sigma_{\eta_F} = 7.9;\ m_{\mu_F} = -1.1, \sigma_{\mu_F} = 9.2$

$L_R = 16$

Note: The unusual hockey stick shape of the total received power is caused by the window effects. The points on the hockey stick are located close to the window and the rest of the points are away from the window.

Appendix B

DME Models

B.1 DME Models for the Fuller Laboratories

B.1.1 Fuller DME for ITI: LOS

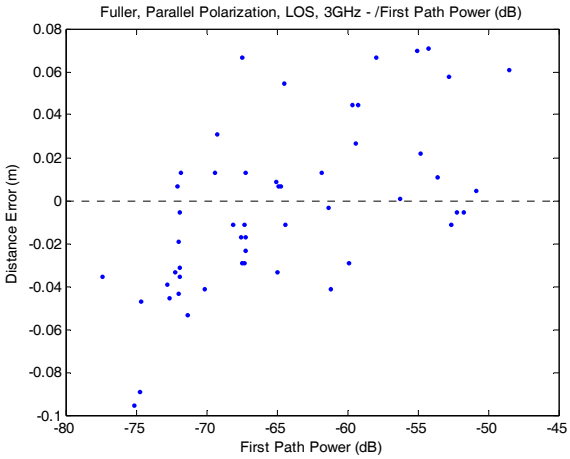

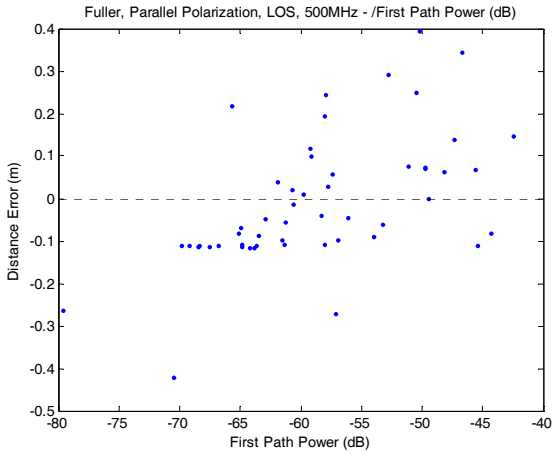

Figure B.1: DME for Fuller, ITI – LOS

@ 3GHz (N/A)		@ 500MHz (N/A)	
Mean 1 = 0	Std. 1 = 0.04	Mean 1 = 0	Std. = 0.14
Mean 2 = N/A	Std. 2 = N/A	Mean 2 = N/A	Std. = N/A
Mean 3 = N/A	Std. 3 = N/A	Mean 3 = N/A	Std. = N/A

B.1.2 Fuller DME for ITI: OLOS

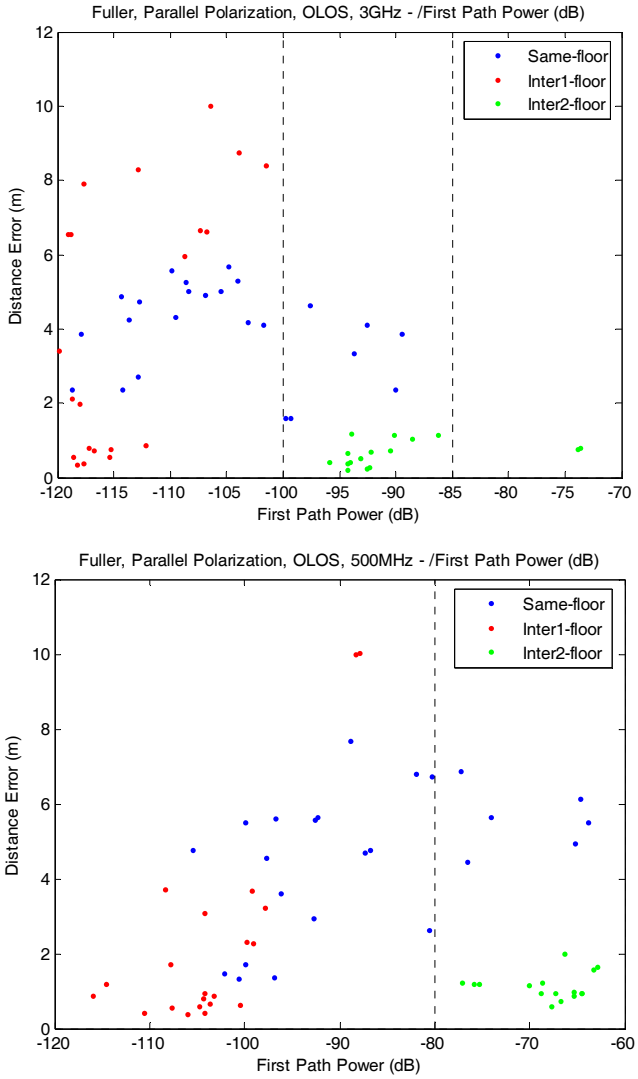

Figure B.2: DME for Fuller, ITI – OLOS

@ 3GHz	Thresholds (-85, -100)	@ 500MHz Thresholds (-80)	
Mean 1 = 0.8	Std. 1 = 0.1	Mean 1 = N/A	Std. 1 = N/A
Mean 2 = 1.4	Std. 2 = 1.3	Mean 2 = 2.2	Std. 2 = 2
Mean 3 = 4.3	Std. 3 = 2.6	Mean 3 = 3.2	Std. 3 = 2.6

B.1.3 Fuller DME for OTI: Ground Mounted Transmitter

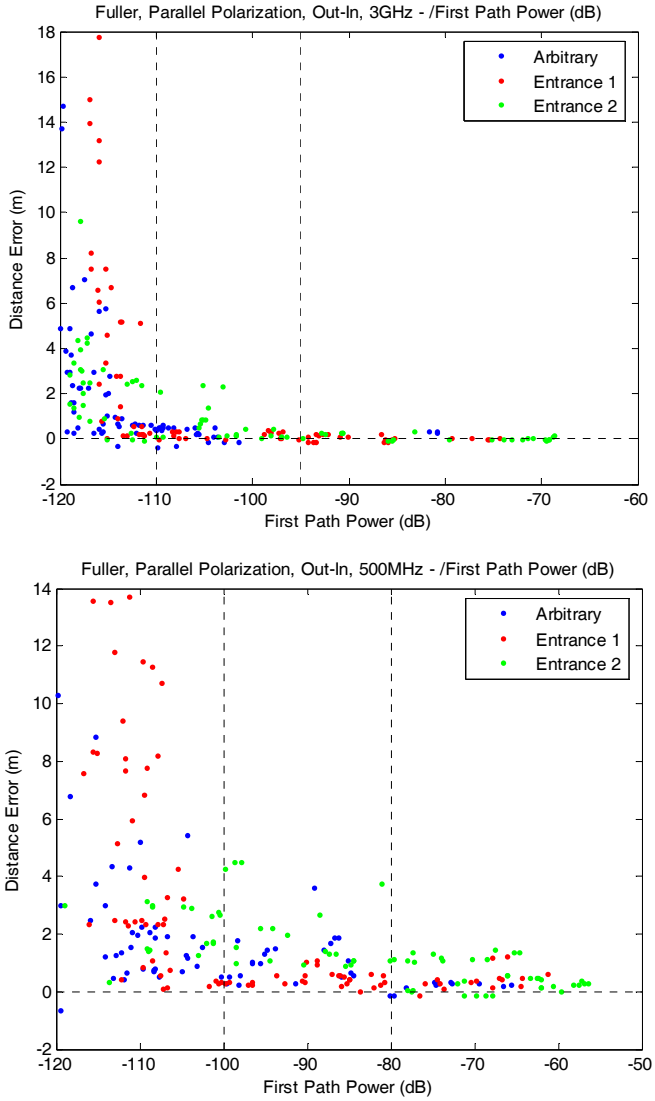

Figure B.3: DME for Fuller, OTI – Ground Mounted Transmitter

@ 3GHz	Thresholds (-95, -110)	@ 500MHz	Thresholds (-80, -100)
Mean 1 = 0	Std. 1 = 0.1	Mean 1 = 0.3	Std. 1 = 0.3
Mean 2 = 0.2	Std. 2 = 0.2	Mean 2 = 0.7	Std. 2 = 0.6
Mean 3 = 3.4	Std. 3 = 4.1	Mean 3 = 3.6	Std. 3 = 3.6

B.2 DME Models for the 17 Schussler Road

B.2.1 Schussler DME for ITI: OLOS

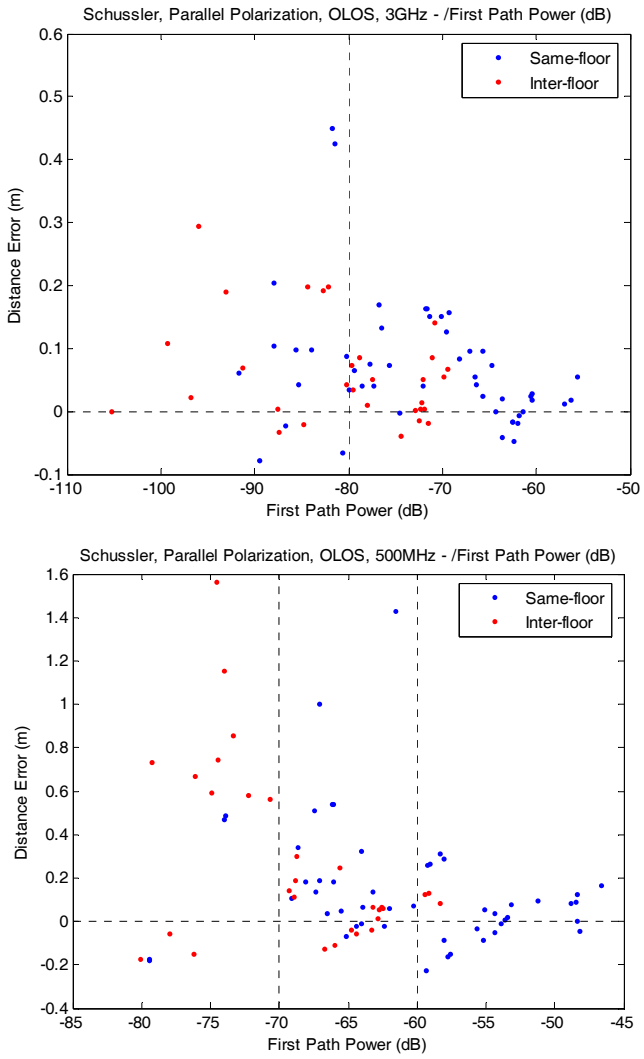

Figure B.4: DME for Schussler, ITI – OLOS

@ 3GHz	Thresholds (-80)	@ 500MHz Thresholds (-60,-70)	
Mean 1 = 0	Std. 1 = 0.1	Mean 1 = 0.1	Std. = 0.1
Mean 2 = 0.1	Std. 2 = 0.1	Mean 2 = 0.2	Std. = 0.3
Mean 3 = N/A	Std. 3 = N/A	Mean 3 = 0.5	Std. = 0.5

B.2.2 Schussler DME for OTI: Ground Mounted Transmitter

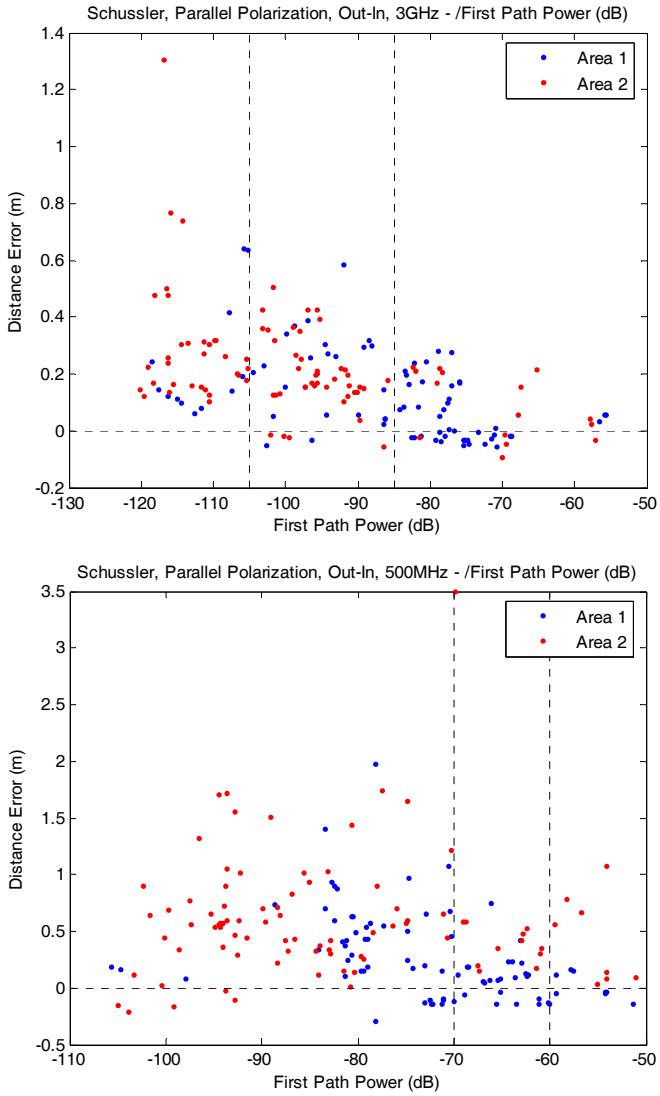

Figure B.5: DME for Schussler, OTI – Ground Mounted Transmitter

@ 3GHz	Thresholds (-85, -105)	@ 500MHz Thresholds (-60, -70)	
Mean 1 = 0.1	Std. = 0.1	Mean 1 = 0.2	Std. = 0.3
Mean 2 = 0.2	Std. = 0.1	Mean 2 = 0.3	Std. = 0.6
Mean 3 = 0.3	Std. = 0.2	Mean 3 = 0.5	Std. = 0.4

B.3 DME Models for the Norton Company

B.3.1 Norton DME for ITI: LOS

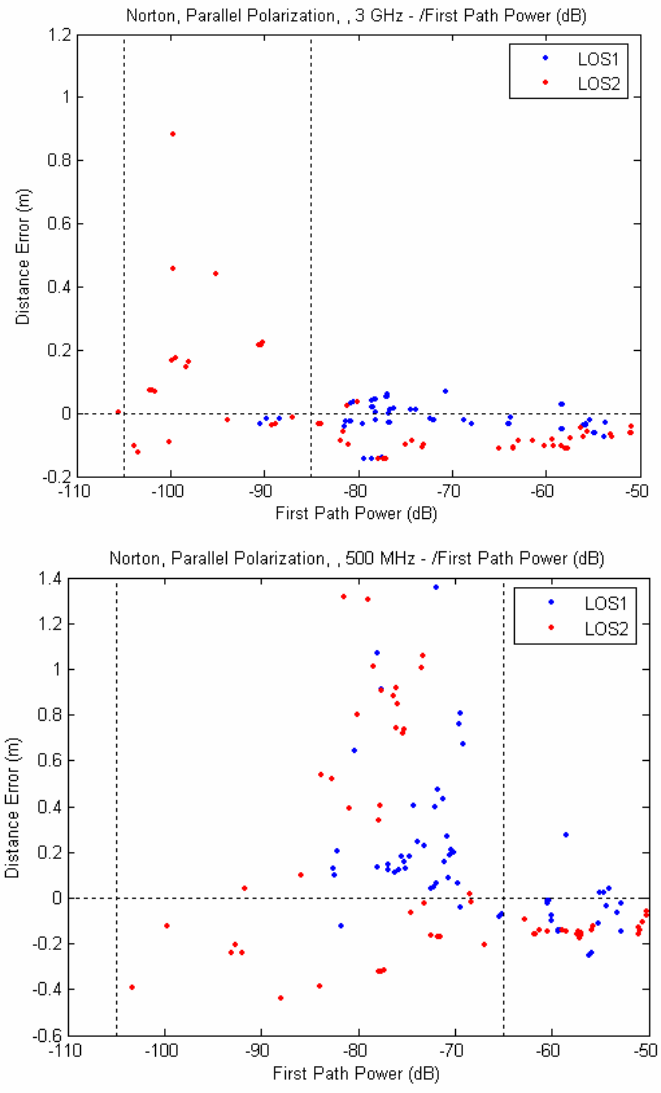

Figure B.6: DME for Norton, ITI – LOS

@ 3GHz ; Thresholds (-85, -105)

Mean 1 = -0.04 Std. 1 = 0.05
Mean 2 = 0.12 Std. 2 = 0.23
Mean 3 = N/A Std. 3 = N/A

@ 500MHz; Thresholds (-65, -105)

Mean 1 = -0.1 Std. 1 = 0.09
Mean 2 = 0.27 Std. 2 = 0.44
Mean 3 = N/A Std. 3 = N/A

B.3.2 Norton DME for OTI: OLOS

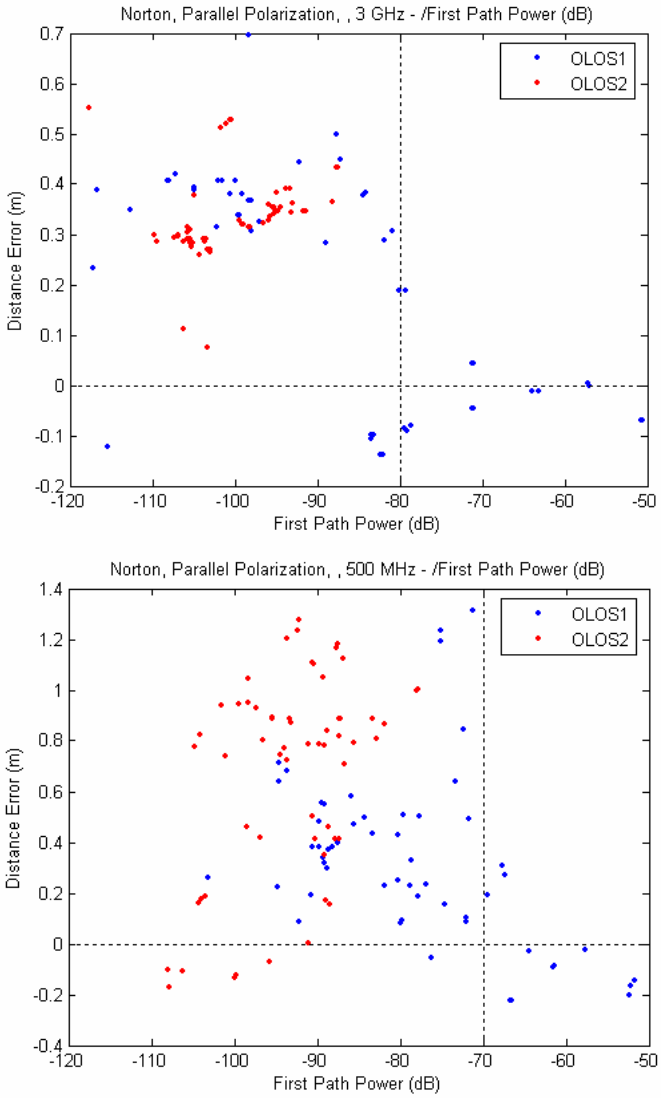

Figure B.7: DME for Norton, OTI – OLOS

@ 3GHz	Thresholds (-80, -120)	@ 500MHz	Thresholds (-70, -120)
Mean 1 = -0.01	Std. 1 = 0.08	Mean 1 = -0.04	Std. 1 = 0.19
Mean 2 = 0.32	Std. 2 = 0.15	Mean 2 = 0.57	Std. 2 = 0.38
Mean 3 = N/A	Std. 3 = N/A	Mean 3 = N/A	Std. 3 = N/A

B.3.3 Norton DME for RTI: Roof Mounted Transmitter

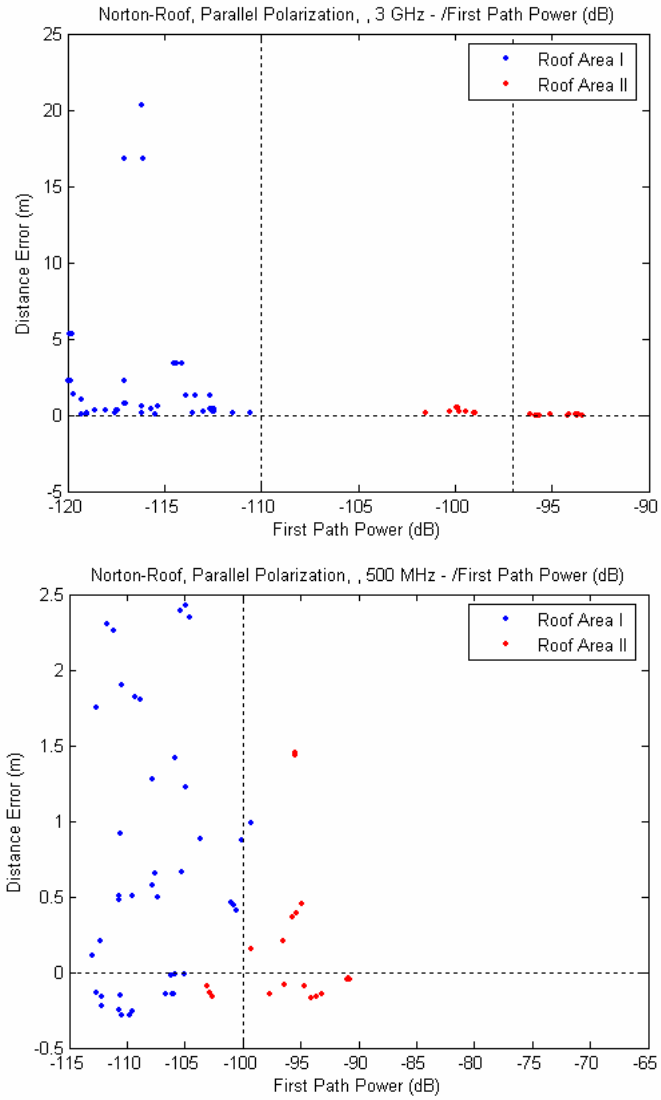

Figure B.8: DME for Norton, RTI – Roof Mounted Transmitter

@ 3GHz Thresholds (-95, -110)

Mean 1 = -0.01 Std. 1 = 0.04
Mean 2 = 0.30 Std. 2 = 0.15
Mean 3 = 2.29 Std. 3 = 4.61

@ 500MHz Thresholds (-85, -100)

Mean 1 = N/A Std. 1 = N/A
Mean 2 = 0.32 Std. 2 = 0.58
Mean 3 = 0.65 Std. 3 = 0.88

B.4 DME Models for the Atwater Kent Laboratory

B.4.1 AK – Roof PLM for OTI: Roof Mounted Transmitter

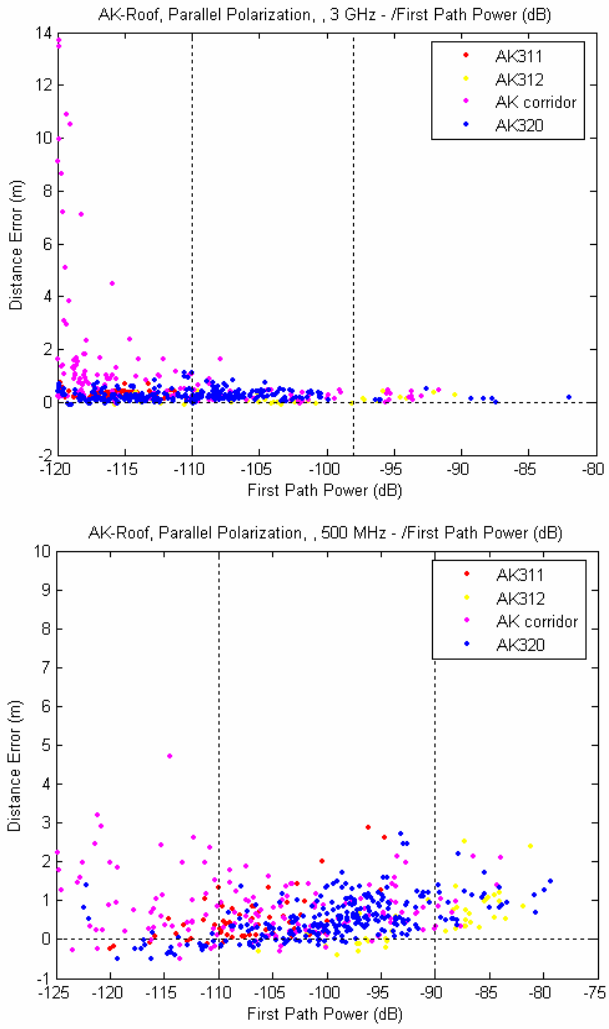

Figure B.9: DME for Norton, RTI – Roof Mounted Transmitter

@ 3GHz	Thresholds (-97, -110)	@ 500MHz	Thresholds (-90, -110)
Mean 1 = 0.19	Std. 1 = 0.14	Mean 1 = 0.96	Std. 1 = 0.57
Mean 2 = 0.26	Std. 2 = 0.22	Mean 2 = 0.57	Std. 2 = 0.52
Mean 3 = 0.76	Std. 3 = 1.81	Mean 3 = 0.60	Std. 3 = 0.99

Bibliography

[Ala03a] B. Alavi and K. Pahlavan, "Bandwidth effect on distance error modeling for indoor geolocation," *Proc. IEEE 14th Annual IEEE International Symposium on Personal Indoor and Mobile Radio Communications (PIMRC 2003)*, Vol. 3, 7-10 Sept. 2003, pp. 2198 – 2202.

[Ala03b] B. Alavi and K. Pahlavan, "Modeling of The Distance Error for Indoor Geolocation", *Proc. IEEE Wireless Communications and Networking Conference (WCNC)*, 2003, Vol. 1, 16-20 March 2003, pp. 668 – 672.

[Ala04] B. Alavi, K. Pahlavan, X. Li, and N. Alsindi, "Indoor Geolocation Distance Error Modeling with UWB Technology," *Proceedings of IASTED 2nd International Conference on Communication and Computer Networks, CCN* 2004, Nov. 8-10 2004.

[Ala05a] B. Alavi and K. Pahlavan, "Analysis of Undetected Direct Path in Time of Arrival Based UWB Indoor Geolocation," *Proc. IEEE 62nd Vehicular Technology Conference 2005 (VTC-Fall 2005)*, 25-28 September 2005, Dallas, Texas.

[Ala05b] B. Alavi, K. Pahlavan, N. Alsindi, and X. Li, "Indoor Geolocation Distance Error Modeling using UWB Channel Measurements", *IEEE 16th Annual IEEE International Symposium on Personal Indoor and Mobile Radio Communications (PIMRC 2005)*, 11-14 Sept. 2005.

[Ala05c] B. Alavi, N. Alsindi, K. Pahlavan, "Report on Measurement and Modeling," Internal report for Defense Advanced Research Projects Agency (DARPA), Innovative Methods for Geolocation and Communication with UWB Mobile Radio Networks (UWB-MRN), July 2005.

[Ala06a] B. Alavi and K. Pahlavan, "Modeling of the TOA based Distance Measurement Error Using UWB Indoor Radio Measurements," *IEEE Communication Letters*, Vol. 10, No. 4, April 2006.

[Ala06b] B. Alavi and K. Pahlavan, "Studying the Effect of Bandwidth on Performance of UWB Positioning Systems," IEEE WCNC 2006, Las Vegas, USA, April 3-6, 2006.

[Als03] N. Alsindi, Performance of TOA estimation algorithms in different indoor multipath conditions, M.S. thesis, Worcester Polytechnic Institute, Worcester, MA, May 2003.

[Als04] N. Alsindi, X. Li, and K. Pahlavan, "Performance of TOA estimation algorithms in different indoor multipath conditions," *Proc. IEEE WCNC 2004*, Atlanta, GA, Apr. 2004.

[And93] H. R. Anderson, "A ray-tracing propagation: model for digital broadcast systems in urban areas," *IEEE Trans. Broadcast.*, AB-39, 309-317, 1993.

[And94] J. B. Anderson, T. S. Rappaport, and S. Yoshida, "Propagation measurements and models for wireless communications channels," *IEEE Communication Magazine*, January 1995.

[Bah00a] P. Bahl and V.N. Padmanabhan, and A. Balachandran, "Enhancements to the RADAR User Location and Tracking System," *Tech. Rep. MSR-TR-00-12, Microsoft Research*, Feb. 2000.

[Bah00b] P. Bahl and V.N. Padmanabhan, "RADAR: An in-Building RF-based user location and tracking system," *Proc. Of IEEE INFOCOM 2000.*, vol. 2, pp. 775 - 784 , March 2000.

[Ben99] J. Beneat, K. Pahlavan, and P. Krishnamurthy, “Radio channel characterization for indoor and urban geolocation at different frequencies,” *Proc. IEEE PIMRC ’99,* Osaka, Japan, September 1999.

[Cas02] D. Cassioli; M. Z. Win, A. F. Molisch, “The ultra-wide bandwidth indoor channel: from statistical model to simulations,” *Selected Areas in Communications, IEEE Journal on* , Vol. 20, No. 6, Aug. 2002, pp. 1247 – 1257.

[Che99] P. C. Chen, “A Non-Line-of-Sight Error Mitigation Algorithm in Location Estimation,” *IEEE WCNC*, 1999, pp. 316-320.

[Fal96] A. Falsafi, K. Pahlavan, and G. Yang, “Transmission techniques for radio LAN's-a comparative performance evaluation using ray tracing,” *IEEE Journal on Sel. Areas in Commun.*, vol. 14, no. 33, Apr. 1996, pp 477-491.

[Foe02] J. Foerster and Q. Li, *UWB Channel Modeling Contribution from Intel*, Working Group for Wireless Personal Area Networks (WPANs), IEEE 802.15-02/279r0-SG3a, June 24, 2002.

[Fon01] R. Fontana, “Advances in ultrawideband indoor geolocation systems,” presented at the 3rd IEEE Workshop on WLAN, Boston, September 2001.

[Gez05] S. Gezici, Z. Tian, G. G. , H. K. amd A.F. Molisch, H. Poor, and Z. Sahinoglu, “Localization via ultra-wideband radios: a look at positioning aspects for future sensor networks,” IEEE Signal Processing Mag., vol. 22, no. 4, pp. 70–84, July 2005.

[Gha03a] S. S. Ghassemzadeh, L. J. Greenstein, A. Kaveiae, T. Sveinsson, and V. Tarokh, “UWB indoor delay profile model for residential and commercial buildings,” *Proc. IEEE 58th Vehicular Technology Conference 2003 (VTC-Fall 2003),* 6-9 October 2003, Lake Buena Vista, FL, Fall 2003, pp. 3120-3125.

[Gha03b] S.S. Ghassemzadeh, L.J. Greenstein, A. Kavcic, T. Sveinsson, and V. Tarokh, “UWB indoor path loss model for residential and commercial buildings,” *IEEE VTC 2003-*Fall,Volume: 5, 6-9 Oct. 2003, Pages:3115 – 3119.

[Gha04] M. Ghavami, L. B. Michael, and R. Kohno, *Ultra-wideband Signals and Systems in Communication Engineering*, Wiley, Hoboken, NJ, 2004.

[Gre97] L. J. Greenstein, V. Erceg, Y. S. Yeh, and M. V. Clark, “A New Path-Gain/Delay-Spread Propagation Model for Digital Cellular Channels,” *IEEE Trans. VT*, vol. 46, no. 2, May 1997, pp. 477-485.

[Hah04] D. Hahnel, W. Burgard, D. Fox, K. Fishkin, M. Philipose, "Mapping and localization with RFID technology," IEEE International Conference on Robotics and Automation (ICRA '04), Vol. 1, 2004 pp. 1015 - 1020.

[Has93] H. Hashemi, “The indoor radio propagation channel,” *Proc. IEEE,* Vol. 81, pp. 943-968, 1993.

[Has02] M. Hassan-Ali and K. Pahlavan, “A new statistical model for site-specific indoor radio propagation prediction based on geometric optics and geometric probability,” *IEEE Trans. on Wireless Communications*, Vol. 1, Issue 1, Jan. 2002 Page(s):112 – 124.

[How90] S.J. Howard and K. Pahlavan, “Measurement and analysis of the indoor radio channel in the frequency domain,” *Instrumentation and Measurement, IEEE Transactions on*, Vol. 39, No. 5, Oct. 1990, pp. 751 – 755.

[How91] S. J. Howard, Frequency domain characteristics and autoregressive modeling of the indoor radio channel, Ph.D. dissertation, Worcester Polytechnic Institute, Worcester, MA, May 1991.

[IEE03] IEEE Std 802.15.3 standard groups document, 2003.

[IWT04] X. Li and K. Pahlavan, “Short range UWB indoor positioning,” Technical report, CWIN, WPI, April 2004.

[Jai01] R. Jain, A. Puri, and R. Sengupta, "Geographical routing using partial information for wireless ad hoc networks, " *IEEE Pers. Commun.*, Feb. 2001, pp. 48-57.

[Jen01] P. Jensfelt, "Approaches to mobile robot localization in indoor environments", PhD Thesis, Royal Institute of Technology, Stockholm, Sweden, 2001.

[Kan04a] M. Kanaan, K. Pahlavan, "A Comparison of Wireless Geolocation Algorithms in The Indoor Environment", *Proc. of the IEEE WCNC*, 2004.

[Kan04b] M. Kanaan., K. Pahlavan, "CN-TOAG: a new algorithm for indoor geolocation," *IEEE International Symposium on Personal, Indoor and Mobile Radio Communications, IEEE-PIMRC’04*, vol. 3, Sept. 2004.

[Ko98] Y. Ko and N. H. Vaidya, "Location-aided routing (LAR) in mobile ad hoc networks, " *Proc. ACM/IEEE MOBICOM ’98*, Dallas, TX, 1998.

[Kos00] H. Koshima and J. Hoshen, "Personal locator services emerge," *IEEE Spectrum*, Feb. 2000, pp. 41-48.

[Kri99a] P. Krishnamurthy and Kaveh Pahlavan, "Distribution of range error and radio channel modeling for indoor geolocation applications," *Proc. Of PIMRC*, Kyoto, Japan, Sept. 1999.

[Kri99b] P. Krishnamurthy, Analysis and modeling of the wideband radio channel for indoor geolocation applications, Ph.D. dissertation, Worcester Polytechnic Institute, 1999.

[Li04] X. Li and K. Pahlavan, “Super-resolution TOA estimation with diversity for indoor geolocation,” *IEEE Trans. on Wireless Communications*, Vol. 3, No. 1, Jan. 2004, pp. 224-234.

[Mey96] M. J. Meyer *et al*., “Wireless Enhanced 9-1-1 Service – Making It a Reality,” *Bell Labs Tech. J.*, pp. 188-202, autumn 1996.

[Mol03] A.F. Molishch, J.R. Foerster, and Marcus Pendergrass, “Channel models for ultrawideband personal area networks,” *IEEE Wireless Communications*, Vol. 10, No. 6, Dec. 2003, pp. 14 - 21.

[Opp04] I. Oppermann, M. Hamalainen, and J. Iinatti, *UWB Theory and Applications*, Wiley, Hoboken, NJ, 2004.

[Pah98] K. Pahlavan, P. Krishnamurthy, and J. Beneat, “Wideband Radio Channel Modeling for Indoor Geolocation Applications,” *IEEE Communication Mag.*, Vol. 36., No. 4, Apr. 1998, pp. 60-65.

[Pah00] K. Pahlavan, P. Krishnamurthy, A. Hatami, M. Ylianttila, J. Mäkelä, R. Pichna, J. Vallström, "Handoff in Hybrid Mobile Data Networks," *IEEE Personal Communications Magazine*, Vol.7 No.2, April 2000, pp. 34-47.

[Pah02a] K. Pahlavan, X. Li, and J. P. Makela, “Indoor Geolocation Science and Technology,” *IEEE Communication. Magazine*., Vol. 40, No. 2, Feb. 2002, pp. 112-118.

[Pah02b] K. Pahlavan and P. Krishnamurthy, *Principles of Wireless Networks – A Unified Approach*, Prentice Hall, 2002.

[Pah05] K. Pahlavan, A. H. Levesque, *Wireless Information Networks*, Second Edition, Wiley-Interscience, 2005.

[Por03] D. Porcino and W. Hirt, “Ultra-wideband radio technology: potential and challenges ahead,” *IEEE Communications Magazine*, Vol. 41, No. 7, July 2003, pp. 66 - 74.

[Pot00] G. J. Pottie and W. J. Kaiser, "Wireless integrated network sensors, " *Commun.. ACM*, May 2000, pp. 51-58.

[Rap02] T. S. Rappaport, *Wireless Communications:Principles and Practice*, 2nd ed., Prentice Hall, Upper Saddle River, NJ, 2002.

[Roo02a] Teemu Roos, Petri Myllymaki, Henry Tirri, , "A statistical modeling approach to location estimation," *IEEE Trans. Mobile Comput.nternational Journal of Wireless Information Networks*, vol. 1, no. 1, pp. 59-69, March 2002.

[Roo02b] Teemu Roos, Petri Myllymaki, Henry Tirri, Pauli Miskangas, and Juha Sievanen, "A probabilistic approach to WLAN user location estimation," *International Journal of Wireless Information Networks*, vol. 9, no. 3, pp. 155-164, July 2002.

[Ros76] S. Ross, *A First Course in Probability*, Macmillan Publishing Co., 1976.

[Sal87] A. M. Saleh and R. A. Valenzuela, "A statistical model for indoor multipath propagation," *IEEE Journal on Selected Areas in Communication.* JSAC-5, pp 128-137, 1987.

[Sma02] A. Smailagic and D. Kogan, "Location sensing and privacy in a contextaware computing environment," IEEE Wireless Commun. Mag., vol. 9, no. 5, pp. 10–17, Oct. 2002.

[War97] A. Ward, A. Jones, A. Hopper, "A new location technique for the active office", *IEEE Personal Communications Magazine*, October 1997.

[Wer98] J. Werb and C. Lanzl, "Designing a positioning system for finding thingsand people indoors, IEEE Spectrum, pp. 71-78, Sept. 1998.

[Zan03] E.D. Zand and K. Pahlavan, "Measurement of TOA using frequency domain characteristics for indoor geolocation", *IEEE-PIMRC 2003*, Volume: 3, 7-10 Sept. 2003, Pages:2213 – 2217.